DEVELOPMENT OF A MINIATURE ODOUR SENSOR FOR IMPLANTATION IN MICE

A THESIS

submitted to

Indian Institute of Science Education and Research Pune

in partial fulfillment of the requirements for the

BS-MS Dual Degree Programme

by

ANANTHA PADMANABHAN

Department of Biology
Indian Institute of Science and Education and Research, Pune
Dr. Homi Bhabha Road,
Pashan, Pune 411008, INDIA

March 2025

Under the supervision of

Prof. Dr. Tobias Ackels
Sensory Dynamics and Behaviour
University of Bonn Medical Center
Life and Brain Center
53127-Bonn, Germany

CERTIFICATE

This is to certify that this dissertation entitled "**DEVELOPMENT OF A MINIATURE ODOUR SENSOR FOR IMPLANTATION IN MICE**" towards the partial fulfillment of the BS-MS dual degree programme at the Indian Institute of Science Education and Research, Pune represents study/work carried out by **Anantha Padmanabhan** at Institute of Experimental Epileptology and Cognition Research (IEECR), University Of Bonn Medical Center, Germany under the supervision of **Prof. Dr. Tobias Ackels**, University of Bonn Medical Center, Bonn, Germany during the academic year 2024-2025.

Anantha Padmanabhan

Prof. Dr. Tobias Ackels

Dr. Nixon M Abraham

Committee

Prof. Dr. Tobias Ackels

Dr. Nixon M Abraham

This thesis is dedicated to all the songs that rule my playlist

DECLARATION

I hereby declare that the matter embodied in the report entitled ”Development of a Miniature Odour Sensor for Implantation in Mice” are the results of the work carried out by me at the Institute of Experimental Epileptology and Cognition Research (IEECR), University Of Bonn Medical Center, Germany and in affiliation with Indian Institute of Science Education and Research, Pune under the supervision of Prof. Dr. Tobias Ackels and the same has not been submitted elsewhere for any other degree. Wherever others contribute, every effort is made to indicate this clearly, with due reference to the literature and acknowledgment of collaborative research discussions.

Anantha Padmanabhan
20201046

Prof. Dr. Tobias Ackels

ACKNOWLEDGMENT

I am grateful to my supervisor, Prof. Dr. Tobias Ackels, for this great opportunity to learn many new things and his support during the project. I would like to thank Dr. Nixon Abraham for his support as the expert for my project. I would also like to thank my labmates - Anantu, Shambhavi, Dyutika, Amir, Julia, Neelam, Linda and Nele for being a team and making the work fun. This project would not have been possible without the support of Ben and Axel from the CADRE team.

My family supported me throughout this journey. A bunch of people I am indebted to for bearing with all my craziness - Jyothi, Anju, Rifa, Joseph, Vishnupriya, Bhageerath, Krishna, Nikhil, Anuvind, Devapriyan, Ann and Abhilash.

Finally, I thank Akshai and Shijil for guiding my life decisions with their wisdom and reducing the damage I would have done to myself.

ABSTRACT

Olfactory navigation is crucial for survival-related behaviours in animals, including locating food sources, evading predators, and selecting mates. There is increasing evidence that suggests mice can process intermittent and fluctuating odour stimuli to extract spatial and temporal information for effective navigation.

We have devised a custom-designed open-field behavioural arena (150 cm × 108 cm) to study odour-based navigation in mice. The arena features controlled airflow and visual isolation to have the animal focus exclusively on olfactory cues that are introduced via a custom-made odour delivery device. To gain a better understanding of the sensory input during navigation, we aim to develop a miniature, head-mounted odour sensor for real-time olfactory information recording in freely behaving animals.

We evaluate various odour detection technologies, including a photoionisation detector (PID), an ethanol sensor, and a metal oxide (MOx) sensor. While a PID offers high sensitivity and fast response times, their size and cost limit their applicability for head-mounted use. MOx sensors, particularly those incorporating microelectromechanical systems (MEMS), are ideal due to their compact size, high sensitivity, and rapid response times. A metal oxide sensor, the Micro Chemical Sensor (MiCS) 6814 — which has three independent sensing elements — was determined to be the suitable sensor for the project due to its compact size and sensitivity to volatile organic compounds (VOCs).

A significant challenge when using MOx sensors is their slow recovery time, which limits their ability to capture rapid odour concentration fluctuations in turbulent environments. By applying signal deconvolution with a rise-decay-sustain kernel, we were able to overcome the slow recovery of this sensor and produce signals using the MiCS that are comparable to a PID while capturing dynamic olfactory information.

This paves the way to use this sensor as a chronic lightweight implant, allowing its integration into behavioural experiments with freely moving mice.

Contents

1 INTRODUCTION **1**

1.1 The Role of Olfaction in Mammalian Navigation 1

1.2 Experimental setup - Open Field Behavioural Arena 3

1.3 Measuring Odour Concentrations and Fluctuations 4

1.3.1 Photoionisation Detector 4

1.3.2 Ethanol Sensor 4

1.3.3 Metal Oxide Sensor 5

2 MATERIALS and METHODS **6**

2.1 Instruments 6

2.2 Softwares 8

2.3 Odour Delivery 9

2.3.1 220A Aurora Olfactometer 9

2.3.2 Temporal Odour Delivery Device (tODD) 10

2.3.3 Odour Delivery Device (Arena) 11

2.4 Data Acquisition 12

2.5 Data Analysis 13

2.5.1 Deconvolution 13

2.5.2 Quantitative Analysis of Signal Characteristics 14

3 RESULTS **15**

3.1 Simple pulses - tODD 15

3.1.1 Alpha Terpinene 16

3.1.2 Ethyl Butyrate 20

3.1.3 Acetophenone 24

3.2 Coupled pulses - tODD 28

3.2.1 Alpha Terpinene 28

3.2.2 Ethyl Butyrate 32

3.2.3 Acetophenone 36

3.3 Simple pulses - 220A Aurora Olfactometer 40

3.3.1 Alpha Terpinene 40

3.3.2 Ethyl Butyrate 42
3.3.3 Acetophenone 44
3.4 Pulse trains - tODD 46
3.4.1 Alpha Terpinene 46
3.4.2 Ethyl Butyrate 50
3.4.3 Acetophenone 54
3.5 Plumes - tODD 58
3.5.1 Alpha Terpinene 58
3.5.2 Ethyl Butyrate 61
3.6 Plumes - Arena 64
3.6.1 Alpha Terpinene 65
3.6.2 Ethyl Butyrate 67
3.7 Incorporating the Sensor into the Arena 69

4 DISCUSSION **72**

5 CONCLUSIONS **76**

6 REFERENCES **77**

List of Figures

1.1 Schematic of the arena 3
1.2 Arena - (a) Side view, (b) Top view 3

2.1 MiCS 6814 6
2.2 Circuit diagram for the PCB 6
2.3 Printed circuit board 7
2.4 Schematic of a four-channel tODD 10
2.5 An eight-channel tODD 11
2.6 Schematic of Odour delivery device (Arena). 11
2.7 Odour delivery device (Arena) 12

3.1 Alpha Terpinene simple pulses - tODD 16
3.2 Correlation for Alpha Terpinene simple pulses 17
3.3 Normalised AUC and FWHM for Alpha Terpinene simple pulses 18
3.4 Linear Correlation for Normalised AUC and FWHM 19
3.5 Ethyl Butyrate simple pulses - tODD 20
3.6 Correlation for Ethyl Butyrate simple pulses 21
3.7 Normalised AUC and FWHM for Ethyl Butyrate simple pulses 22
3.8 Linear Correlation for Normalised AUC and FWHM 23
3.9 Acetophenone simple pulses - tODD 24
3.10 Correlation for Acetophenone simple pulses 25
3.11 Normalised AUC and FWHM for Acetophenone simple pulses 26
3.12 Linear Correlation for Normalised AUC and FWHM 27
3.13 Alpha Terpinene coupled pulses - tODD 29
3.14 Correlation for Alpha Terpinene coupled pulses 29
3.15 Normalised AUC and FWHM for Alpha Terpinene coupled pulses 30
3.16 Linear Correlation for Normalised AUC and FWHM 31
3.17 Ethyl Butyrate coupled pulses - tODD 32
3.18 Correlation for Ethyl Butyrate coupled pulses 33
3.19 Normalised AUC and FWHM for Ethyl Butyrate coupled pulses 34
3.20 Linear Correlation for Normalised AUC and FWHM 35
3.21 Acetophenone coupled pulses - tODD 36

3.22 Correlation for Acetophenone coupled pulses 37
3.23 Normalised AUC and FWHM for Acetophenone coupled pulses 38
3.24 Linear Correlation for Normalised AUC and FWHM 39
3.25 Alpha Terpinene simple pulses of different concentrations 41
3.26 Normalised AUC plots for Alpha Terpinene simple pulses 41
3.27 Ethyl Butyrate simple pulses of different concentrations 42
3.28 Normalised AUC plots for Ethyl Butyrate simple pulses 43
3.29 Acetophenone simple pulses of different concentrations 44
3.30 Normalised AUC plots for Acetophenone simple pulses 45
3.31 Alpha Terpinene pulse trains of different frequencies - tODD 47
3.32 Latency distribution for Alpha Terpinene pulse trains 48
3.33 Ethyl Butyrate pulse trains of different frequencies - tODD 51
3.34 Latency distribution for Ethyl Butyrate pulse trains 52
3.35 Acetophenone pulse trains of different frequencies - tODD 55
3.36 Latency distribution for Acetophenone pulse trains 56
3.37 Alpha Terpinene plumes - tODD 60
3.38 Difference in the number of peaks detected for Alpha Terpinene plumes 60
3.39 Ethyl Butyrate plumes - tODD 62
3.40 Difference in the number of peaks detected for Ethyl Butyrate plumes . 63
3.41 Behavioural arena - recording locations 64
3.42 Alpha Terpinene plumes - Arena 65
3.43 Alpha Terpinene plumes - Arena 66
3.44 Ethyl Butyrate plumes - Arena 67
3.45 Ethyl Butyrate plumes - Arena 68
3.46 Miniature sensor and the custom-made sensor holder 69
3.47 Design of mouse with sensor, sensor holder and thermistor probe . . . 70
3.48 Commutator and miniature cable with connections established to PCB . 70
3.49 Schematic displaying the plan to integrate the sensor 71

Chapter 1

INTRODUCTION

Olfaction is crucial for animals to gather information and interact with their surroundings. Animals use their sense of smell to identify and differentiate rapidly fluctuating odour stimuli, hence playing an essential role in survival-related behaviours such as navigation, locating food, evading predators and selecting mates (Marin et al., 2021, Sunil et al., 2024). In nature, animals encounter odour stimuli in the form of complex odour plumes. These odour plumes are modulated by turbulent air currents, making them unpredictable and fragmented with complex temporal and spatial patterns (Celani et al., 2014). This results in intermittent and fluctuating odour concentrations in air. This complexity poses significant challenges for organisms like mice, which rely on olfaction to locate odour sources and requires them to effectively detect and process brief odour encounters (Gumaste et al., 2024, Findley et al., 2021, Lewis et al., 2021).

Additionally, the spatiotemporal structure of odour plumes in the environment provides important cues for mice. The mammalian olfactory system can extract spatial information from odour plumes, helping animals to locate odour sources. This ability to interpret spatial information from odours is essential for olfactory navigation (Marin et al., 2021).

1.1 The Role of Olfaction in Mammalian Navigation

Olfactory navigation is pivotal in how mammals interpret and move through their environments. This process involves detecting and processing odour cues to create mental maps, locate resources, and avoid dangers (Baker et al., 2018). Olfactory cues can convey information across vast distances, enabling behaviours such as source detection, trail following, and navigation using distant odour plumes (Jacobs, 2012). This reliance on the sense of smell is particularly pronounced in species like rodents, which often inhabit environments where visual cues are limited. These animals adeptly

combine olfactory information with learned spatial cues to navigate their surroundings effectively (Marin et al., 2021).

Mammals employ various strategies to interpret olfactory information for navigation. Odour plume tracking allows many mammals to detect and follow the concentration gradients of airborne odours to locate the source, a behaviour observed in species ranging from rodents to humans (Sunil et al., 2024). Through spatial mapping, odour cues help animals build mental maps of their surroundings, supporting orientation and route planning. This ability is essential for finding food sources or returning to nesting areas (Poo et al., 2021). Additionally, temporal processing enables mammals to use the timing of odour detection to provide spatial information, with mammals using the temporal dynamics of odour detection to infer the direction and distance of an odour source (Ackels et al., 2021, Gumaste et al., 2024, Lewis et al., 2021).

Mice use active sniffing strategies to extract temporal information from odour plumes. Their active sniffing behaviour, ranging from 4 to 12 Hz, allows them to sample odour fluctuations with high temporal resolution (Wachowiak, 2011). While mice can discriminate the identity of monomolecular odours in less than 200 ms (Abraham et al., 2004), it has been shown that the mouse olfactory system integrates odour information across multiple sniffs to enhance signal detection and discrimination (Resulaj & Rinberg, 2015). This suggests that the temporal patterns within odour plumes affect the detection as well as higher-order olfactory processing. Additionally, the interaction between sniffing-modulated nasal airflow dynamics and olfactory bulb encoding of odour plume intermittency enables mice to reconstruct spatial and temporal characteristics of odour plumes, enhancing their ability to locate odour sources in complex environments (Gumaste et al., 2024).

Mice are equipped with sophisticated olfactory systems capable of processing rapid odour fluctuations. It has been shown that the ability of mice to detect and respond to brief, intermittent odour encounters relies on the encoding of fast odour dynamics by the mouse olfactory bulb. This high temporal resolution is essential for effectively navigating complex odour landscapes (Ackels et al., 2021). The mammalian brain has evolved to process complex olfactory signals efficiently. Dynamic odour information is converted into neural maps within the olfactory cortex, enabling mammals to navigate based on odour cues (Matheson et al., 2022, Grimaud et al., 2024, Poo et al., 2021). This neural representation allows for the integration of olfactory information with other sensory inputs, facilitating comprehensive environmental mapping (Sunil et al., 2024).

1.2 Experimental setup - Open Field Behavioural Arena

To investigate olfactory-driven navigation, we have designed a controlled behavioural arena with dimensions 150 cm × 108 cm. In the arena, animals will be trained to perform an odour-based navigation task to localise the source of an odour. The primary objective of this setup is to create an environment where the animal's movement and decision-making are guided exclusively by olfactory cues in the absence of visual cues.

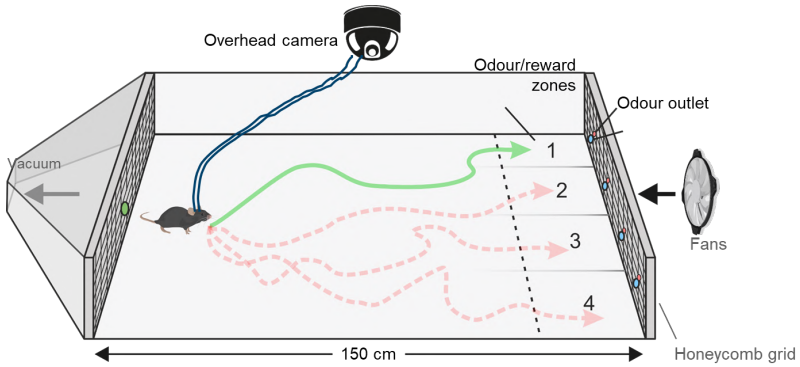

Figure 1.1: Schematic of the arena showing the fans, odour outlet, honeycomb grid, vacuum and odour zones for each port

The arena is enclosed using a surrounding curtain, ensuring the animal is visually isolated from external stimuli that could influence its behaviour. A continuous airflow is maintained through the arena using fans on one side and an exhaust on the other. The honey-comb grids placed in front of the fans break up the laminar structure of the airflow. A pair of infrared (IR) lamps and an IR sensitive camera has been incorporated to provide optimal conditions for video tracking and to avoid visual stimuli or distractions while the mouse performs the behavioural task.

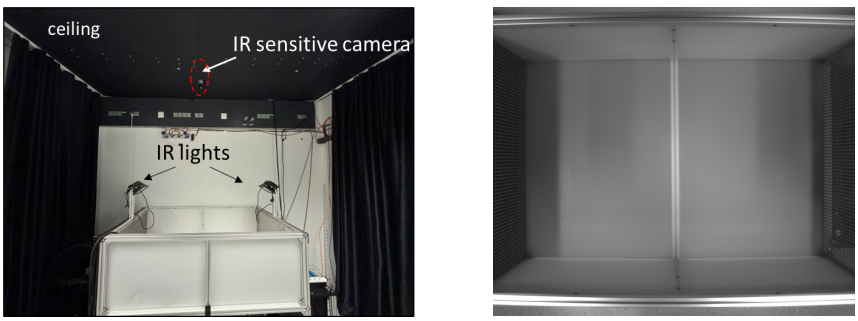

(a) (b)

Figure 1.2: (a) Side view of the arena showing the infrared (IR) lamps and the IR sensitive camera (b) Top view of the arena from the camera

The animal will be trained to navigate towards any of the four odours ports. To motivate navigation specifically towards the rewarded odour port and prevent sampling through odour ports, the odour zone border represented by the region behind the decision line (Figure 1.1) serves as a reference to introduce an intertrial interval.

Understanding how mice navigate using these odour cues requires temporally precise measurement of the sensory input. The aim of this project is to develop a miniature odour sensor that can be head-mounted on a freely behaving animal, performing an odour navigation task to record real-time olfactory information. It will allow us to track odour cues in real time and directly relate them to the behaviour observed.

1.3 Measuring Odour Concentrations and Fluctuations

1.3.1 Photoionisation Detector

Photoionisation detectors (PID) are considered the gold standard for odour detection. PIDs are widely used for measuring volatile organic compounds (VOCs) due to their high sensitivity and fast response times (Baumbach et al., 2003).

PIDs rely on photoionisation, where high-energy ultraviolet (UV) photons ionise gas molecules. The UV lamp in PIDs generates high-energy photons that interact with the VOCs present. When a molecule absorbs a photon with energy higher than its ionisation potential, an electron is liberated. This generates a measurable current proportional to the gas concentration.

The 200B mini photo-ionisation detector (Aurora Scientific) has a bandwidth of 330 Hz, which enables it to faithfully capture rapidly fluctuating stimuli like odour plumes. The limitations posed by its size and cost make it unsuitable for recording real-time olfactory information from a freely behaving animal. The PID will be used to study and compare the characteristics of the miniature sensor developed and used in this project.

1.3.2 Ethanol Sensor

Ethanol sensors provide a more targeted approach for detecting certain volatile compounds. These sensors have been used in behavioural studies involving ethanol as an odour cue. Tariq et al. (2020) demonstrated how head-mounted ethanol sensors can be used to track mouse olfactory-guided behaviour, highlighting their utility in studying odour-based navigation. However, ethanol is an aversive stimulus for mice, which makes it less suitable for this work. These sensors have a limited sensitivity to other

volatile organic compounds and slow response times. In addition to that, the metal case around these sensors needs to be removed to improve its sensitivity, which leaves them susceptible to mechanical damage and malfunctioning due to moisture.

1.3.3 Metal Oxide Sensor

Metal Oxide (MOx) sensors operate on the principle that the conductivity of a metal oxide sensing layer changes in the presence of specific gases, resulting in the detection of different volatile compounds. These sensors can detect a wide range of odorants. Additionally, MOx sensors require fewer electronic components, reducing cost, simplifying design, and making them more compact for various applications (Drix et al., 2021). Their widespread adoption can be attributed to their high sensitivity, robustness, and cost-effectiveness.

The introduction of microelectromechanical systems (MEMS) has further enhanced MOx sensor capabilities, significantly reducing their size, power consumption, and response times (to the order of milliseconds from minutes to hours). There are sensors like Amphenol SGX Sensortech MICS 6814 Sensor with a bandwidth of up to 60 Hz, giving a time resolution of about 16 milliseconds (Dennler et al., 2024). This is sufficient to capture rapid changes in the environment. The enhanced sensitivity, selectivity and rapid response time achieved through the integration of MEMS technology make them suitable for recording temporally complex olfactory information in real-time .

Despite their advantages, one significant challenge is the slow recovery time of MOx sensors. This slow recovery time arises from the fundamental sensing mechanism of MOX sensors, which involves the adsorption and desorption of gas molecules on the metal oxide surface. During exposure to an odour, target molecules interact with the sensor surface, altering its electrical resistance (Monroy et al., 2012). When the odour concentration decreases, the sensor takes a significant amount of time to release the adsorbed molecules and return to its baseline state. In a setting like a behavioural arena with turbulent airflow conditions, where the mouse is constantly moving, and odour gradients shift rapidly, this slow recovery can result in signal lag, affecting the real-time tracking of odour cues essential for navigation. Signal deconvolution using a rise-decay-sustain kernel has been deployed in the signal processing pipeline to overcome this slow recovery.

Chapter 2

MATERIALS and METHODS

2.1 Instruments

Amphenol SGX Sensortech MiCS 6814 Sensor: This is a multi-gas sensor based on MEMS technology. It contains three independent sensing elements RE for reducing gases, OX for oxidising gases and NH_3 for Ammonia and related gases. The RE sensor will be primarily used for the experiments because of its ability to capture rapid fluctuations. The NH_3 and OX sensors were disregarded because of slow decay and inability to differentiate short pulses respectively.

The initial design of the printed circuit board (PCB) was created in collaboration with Nik Dennler, a Postdoctoral Researcher at ETH Zurich (Dennler et al., 2024). Edits were made to the design to significantly reduce its size by establishing connections on both sides of the PCB. The new design also incorporates electronic connections to a thermistor probe which will be implanted on the mouse.

Figure 2.1: MiCS 6814

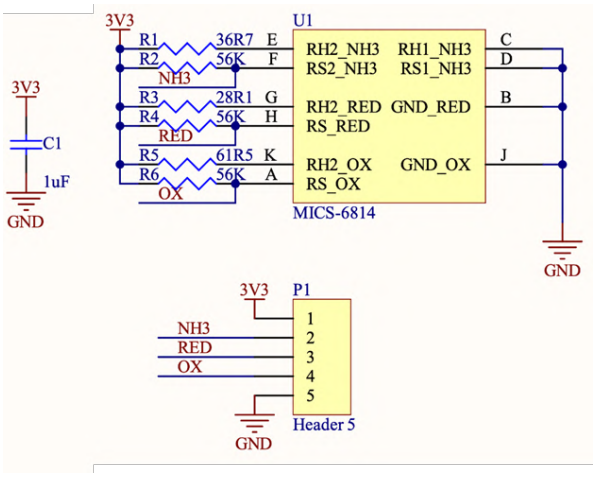

Figure 2.2: Circuit diagram for the PCB

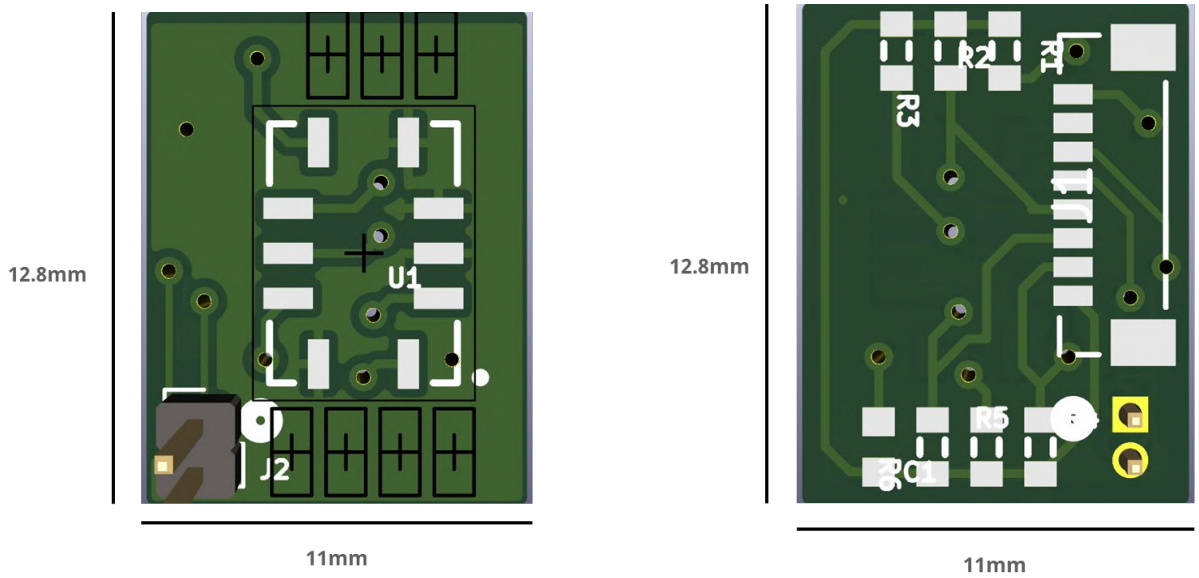

(a) (b)

Figure 2.3: (a) Top view of the PCB, (b) Bottom view of the PCB

Aurora mini–Photoionisation Detector (PID): This device detects volatile organic compounds (VOCs) with a temporal bandwidth of 330 Hz. This bandwidth corresponds to an ability to respond to events with a time resolution as small as about 3 milliseconds (1/330 seconds). It serves as a reference for measuring odour stimuli in our experiments. It provides a reliable control signal to compare the sensitivity and performance of other sensors.

Aurora 220A Olfactometer: The Aurora 220A is designed to present odorants accurately. This device can rapidly switch between different odorants or from an odorant to clean air. The device has a finely controlled airflow system, which allows for precise dilution of odorants with clean air to adjust odorant concentration. Odorants can be delivered for durations ranging from 20 milliseconds and above.

TGS2620: The TGS 2620 is a semiconductor gas sensor designed to detect alcohol vapours and volatile organic compounds (VOCs) like solvents.

Temporal Odour Delivery Device (tODD): tODD is a high-speed device designed to reliably present olfactory stimuli ranging from simple odour pulses in the millisecond range to complex high-frequency plume structures (Ackels et al., 2021).

cDAQ 9215 (Analog Input Module): This module captures analog signals from connected devices, including sensors, enabling real-time data acquisition. It is part of the National Instruments (NI) CompactDAQ series.

cDAQ 9174: A chassis that supports multiple input and output modules, including the cDAQ 9215. It provides power and data connectivity for modular data acquisition, allowing simultaneous acquisition from multiple sources.

CED Micro1401-4: The Micro1401-4 is a data acquisition unit which can sample data up to a rate of 1 MHz. It allows simultaneous recording of waveform data, digital events, and markers.

Multi-Wire Round Cable (STC-36T-8): The STC-36T-8 cable is ideal for integrating miniature sensors into a large behavioural arena while allowing sensor-implanted animals to move freely. It has a compact diameter of just 1.62 mm and is lightweight. This helps to minimise the physical burden and allows the animals to move freely without constraints.The 36 AWG silver-plated copper conductors ensure stable and reliable signal transmission throughout experimental trials.

10-Channel Slip Ring Commutator: The SL10C slip-ring commutator (Campden Instruments Ltd.) maintains a continuous electrical connection between stationary and rotating components, allowing sensor-implanted animals to move without constraint during behavioural experiments. Designed with a 10-channel configuration and a low-noise transmission system, it prevents signal loss while eliminating cable twisting and tangling as the animal explores the arena.

Thermistor Probe: A thermistor probe is a temperature-sensing device that combines a thermistor (a resistor whose resistance changes with temperature) with a protective housing. These probes, which are capable of detecting small temperature variations, will be implanted in the animal to study respiration.

2.2 Softwares

220A Olfactometer Control: The proprietary software controls the Aurora 220A Olfactometer to adjust odour delivery parameters such as duration, concentration, and airflow. It provides precise control over odour stimuli presentation.

Bonsai (Versions 2.8.3 and 2.8.5): Bonsai is an open-source visual programming environment for real-time data acquisition, processing, and visualisation. It is being used with NI-DAQmx devices to capture signals from multiple devices and stream live data during experiments.

NI Max (Version 18.5): National Instruments Measurement & Automation Explorer (NI-MAX) is software configuring, testing, and managing NI hardware devices such as CompactDAQ and data acquisition modules.

PulseBoy (forked from RoboDoig/PulseBoy): Python-based GUI (Graphical User Interface) tool designed to control pulse trains for National Instruments (NI) hardware. This software is used to generate and manage pulse sequences, which are important for controlling devices such as high-speed valves or other equipment that require precise digital inputs.

KICAD: It is used for electronic design automation (EDA). It facilitates the design of schematics and the creation of printed circuit boards (PCBs).

Spike2(Version 10.19): Spike2 is a data acquisition and analysis software developed by Cambridge Electronic Devices. It is capable of stimulus generation, data capture, and control of external equipment. It allows to import data from other systems and export to formats like MATLAB.

Autodesk Fusion 360: Autodesk Fusion 360 is a platform for 3D modelling, simulation, and documentation. It has been used to design holders for the sensor, parts for tODD, etc.

2.3 Odour Delivery

The following devices were used for odour delivery and the odorants used were Alpha Terpinene, Ethyl Butyrate and Acetophenone.

2.3.1 220A Aurora Olfactometer

Mineral oil was used as a control to study the response of PID and MiCS towards airflow. The Total System Flow Rate was set to 200 standard cubic centimetres per minute (sccm). The concentration of odour being delivered can be controlled by altering the Total Flow Percentage through Vial, which is set as a percentage of the Total System Flow Rate. It is limited to a maximum flow rate of 100 sccm and a minimum flow rate of 5 sccm. The recordings were made for the following values of Total Flow Percentage through Vial: 10%, 5% & 1%. The recordings were taken for a series of odour deliveries of the following durations in the given order with a delay of 20 s between 2 consecutive deliveries: 20 ms, 50 ms, 100 ms, 200 ms, 500 ms, 1000 ms and 2000 ms. This sequence was repeated five times for each concentration for all three odours.

2.3.2 Temporal Odour Delivery Device (tODD)

An eight-channel tODD was assembled to present short pulses and plumes with high temporal accuracy as olfactory stimuli. PulseBoy, a Python-based GUI (Graphical User Interface) tool, is used to control the valves and generate and manage pulse sequences. The concentration of all the odours used is 6%. The trial banks designed consisted of the following stimuli:

- Single pulses of different durations with 10 seconds Inter Stimulus Interval: 10 ms, 20 ms, 50 ms, 100 ms, 200 ms, 500 ms, 1000 ms and 2000 ms.
- Coupled pulses of equal duration (10 ms and 20 ms) were delivered, separated by varying inter-stimulus intervals of 10 ms, 20 ms, 50 ms, and 100 ms.
- Pulse trains of different frequencies (5 Hz, 10 Hz, 15Hz, 20 Hz, and 40 Hz) were presented, each lasting for 1 second.
- Four sparse and four busy plumes. The classification of the plume stimuli as sparse or busy was based on signal intermittency, FFT maximum, and coefficient of variability.

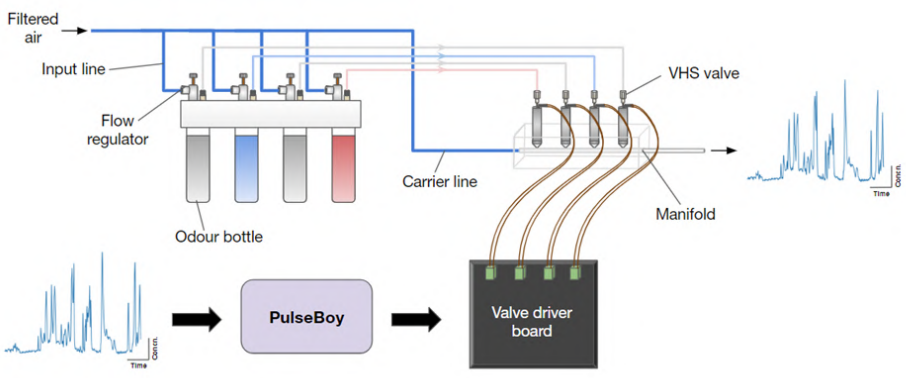

Figure 2.4: Schematic of a four-channel tODD (Ackels et al., 2021)

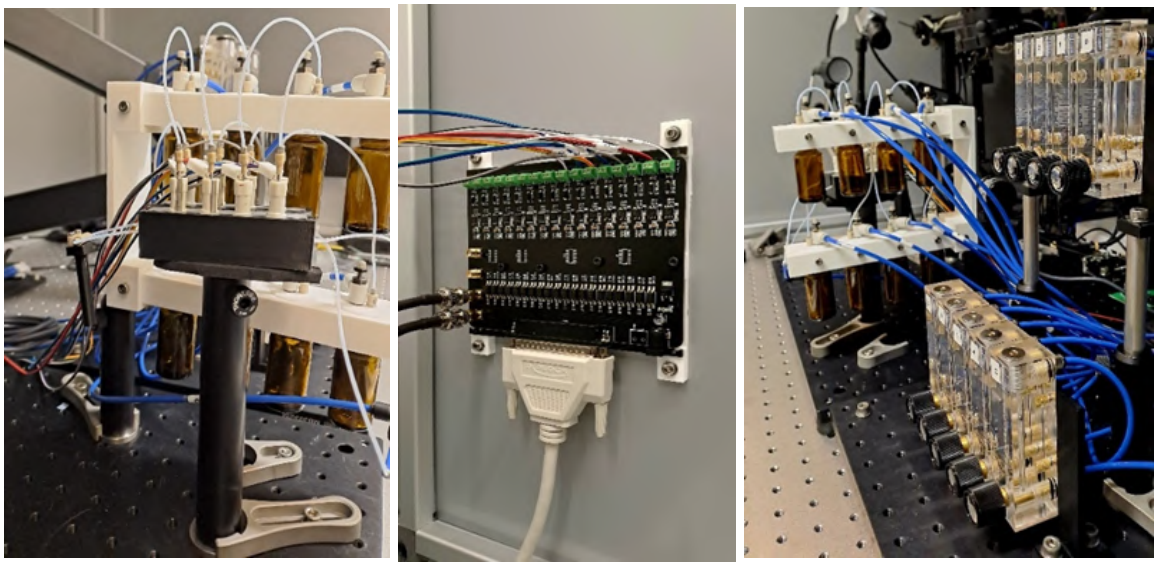

(a) (b) (c)

Figure 2.5: An eight-channel tODD (a) Valves and odour outlet (b) Custom-made valve driver board (c) Flow regulators

2.3.3 Odour Delivery Device (Arena)

In the arena, we have devised a custom multi-channel, multi-valve odour delivery system with four final odour ports. The odour delivery is controlled by two sets of valves: LHD Series 3-Way Control Solenoid Valve (The Lee Company) and SMC VK3000 M5. The combination of these valves allows the dilution and mixing of different odorants used. The non-laminar flow generated in the arena through the honeycomb grid (shown in Figure 2.7) results in rapid fluctuations.

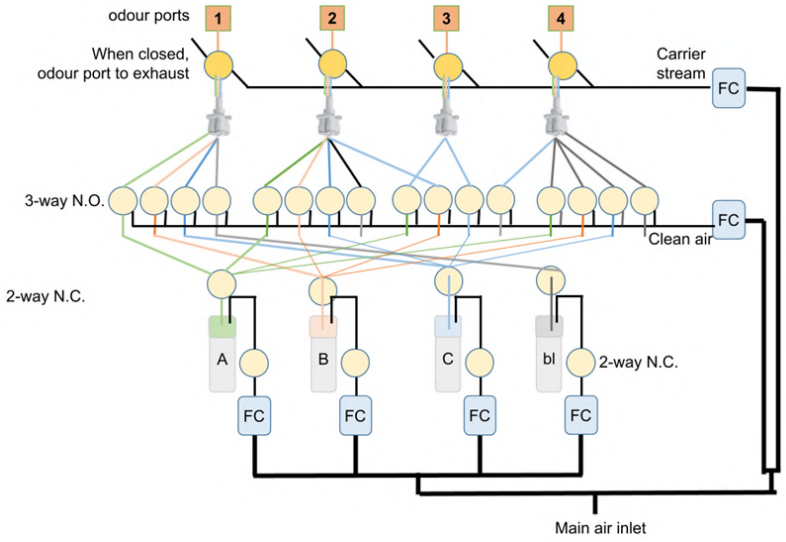

Figure 2.6: Schematic of Odour delivery device (Arena).

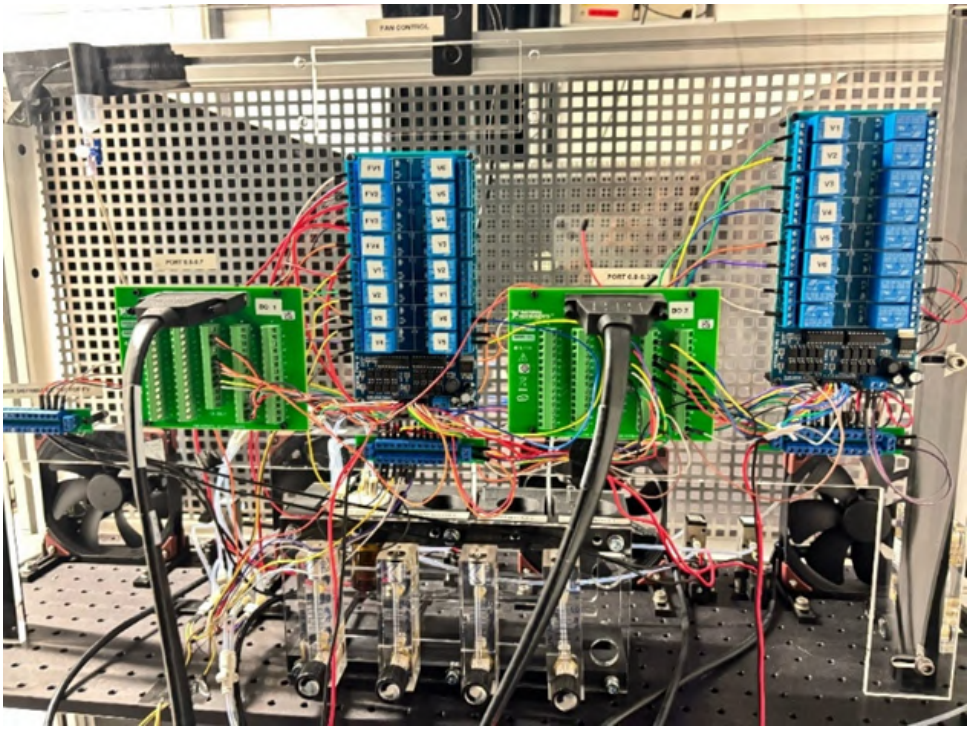

Figure 2.7: Odour delivery device (Arena)

2.4 Data Acquisition

Analog data from all devices was captured using NI-DAQ devices or a CED Micro1401-4, enabling synchronised and precise data logging.

The Spike2 software was used for real-time data acquisition, signal processing, and analysis from Micro1401-1. Spike2's sampling configuration allows simultaneous recording from multiple channels connected to the Micro1401-1's analog and digital inputs, ensuring accurate time-aligned data collection. Spike2 provides various built-in tools for real-time visualisation and event detection.

The Bonsai software (versions 2.8.3 and 2.8.5) was employed for real-time data acquisition from the NI-DAQmx devices and live streaming during the experiments. The Bonsai-DAQmx Library enables the software to identify and acquire data from the connected NI-DAQmx devices. Multiple channels connected to the cDAQ AI module can be included in the Analog Input source. Matrix Writer and CSV Writer act as two different sinks saving data in different forms.

- Matrix Writer: Writes each array-like object in the sequence to a raw binary output stream. The data is saved in the column-major layout.
- CSV Writer: Writes a delimited text representation of each element of the sequence to a text file.

2.5 Data Analysis

The spike recordings saved as .smrx files were exported as .mat files for further analysis in Python using custom written scripts. Python packages such as numpy, scipy, and h5py (for HDF5 file handling) were used for analysis.

2.5.1 Deconvolution

Deconvolution is a mathematical technique used in signal processing to recover the original signal from a distorted signal. In this case, deconvolution helps to recover the true temporal profile of olfactory signals from the raw signal of the sensor recordings by removing distortions caused by sensor response dynamics.

- Convolution Model: The observed signal h is modelled as the convolution of the original signal f with a distortion function g (the rise-sustain-decay kernel)

$$h = f \cdot g$$

- Deconvolution Objective: The goal is to find the solution f to the convolution equation:

$$f \cdot g^{-1} = h$$

- Fourier Transform: The problem is in solved in the frequency domain using the Fourier transform. By the Convolution theorem:

$$F = H/G$$

  Where F, H, and G are the Fourier transforms of f, h, and g, respectively.

- Inverse Fourier Transform: The estimated deconvolved signal f is obtained by taking the inverse Fourier transform of F.

$$rise = e^{(-t/tau\_rise)}$$
$$decay = e^{(-t/tau\_decay)} \qquad kernel = rise * decay * sustain$$
$$sustain = e^{(-t/tau\_sustain)}$$

The kernel consists of three terms; one for rise, one for decay and one for sustain. The sustain term was added to overcome the diminishing of the signals after the sudden rise. The combination of values used for this kernel are:

- tau_rise = 0.002, tau_decay = 0.5, tau_sustain = 1.5, for simple pulses longer than 100 ms

- tau_rise = 0.01, tau_decay = 1, tau_sustain = 1.5, for all signals except simple pulses longer than 100 ms

2.5.2 Quantitative Analysis of Signal Characteristics

- Full Width at Half Maximum (FWHM) measures the duration of a signal peak at half of its maximum amplitude. It is used in quantifying response duration differences between PID and MiCS.
- Area Under the curve (AUC) represents the total integrated response magnitude. It is used in quantifying cumulative exposure effects and comparing overall sensitivity of the devices to different odour concentrations
- Pearson's Correlation Coefficient measures linear correlation between PID and MiCS signals. It quantifies similarity between different devices' odour recognition patterns
- Peak detection was used in the case of pulse trains and odour plumes with varying number of peaks. This helps us to compare the ability of the two devices to capture the temporal structure of the signal.
- Latency has been calculated as the time difference between the peaks detected and start of the trigger for pulse trains.
- Unpaired t-test is a statistical method used to determine whether there is a significant difference between the means of two independent groups. In addition to comparing the means, the test takes into account the variability within each group and evaluates whether the observed difference in means is likely due to random chance or represents a true difference.

Chapter 3

RESULTS

In this section, we compare the MiCS response with the PID response to stimulus types and protocols of varying complexities. The signals presented for MiCS were obtained following signal processing involving deconvolution with a rise-decay-sustain kernel. This analysis allows us to explore the characteristics of the sensors across multiple metrics. As odour stimuli, we used Alpha Terpinene (a terpene), Ethyl Butyrate (an ester), and Acetophenone (a ketone) to assess variations in the sensor's performances for odorants belonging to different chemical classes.

3.1 Simple pulses - tODD

Simple square pulses of different durations ranging from 10 ms to 2000 ms were used to compare the temporal resolution capabilities and the signal stability during sustained exposure of the two sensors. The odorants used are Alpha Terpinene, Ethyl Butyrate and Acetophenone.

3.1.1 Alpha Terpinene

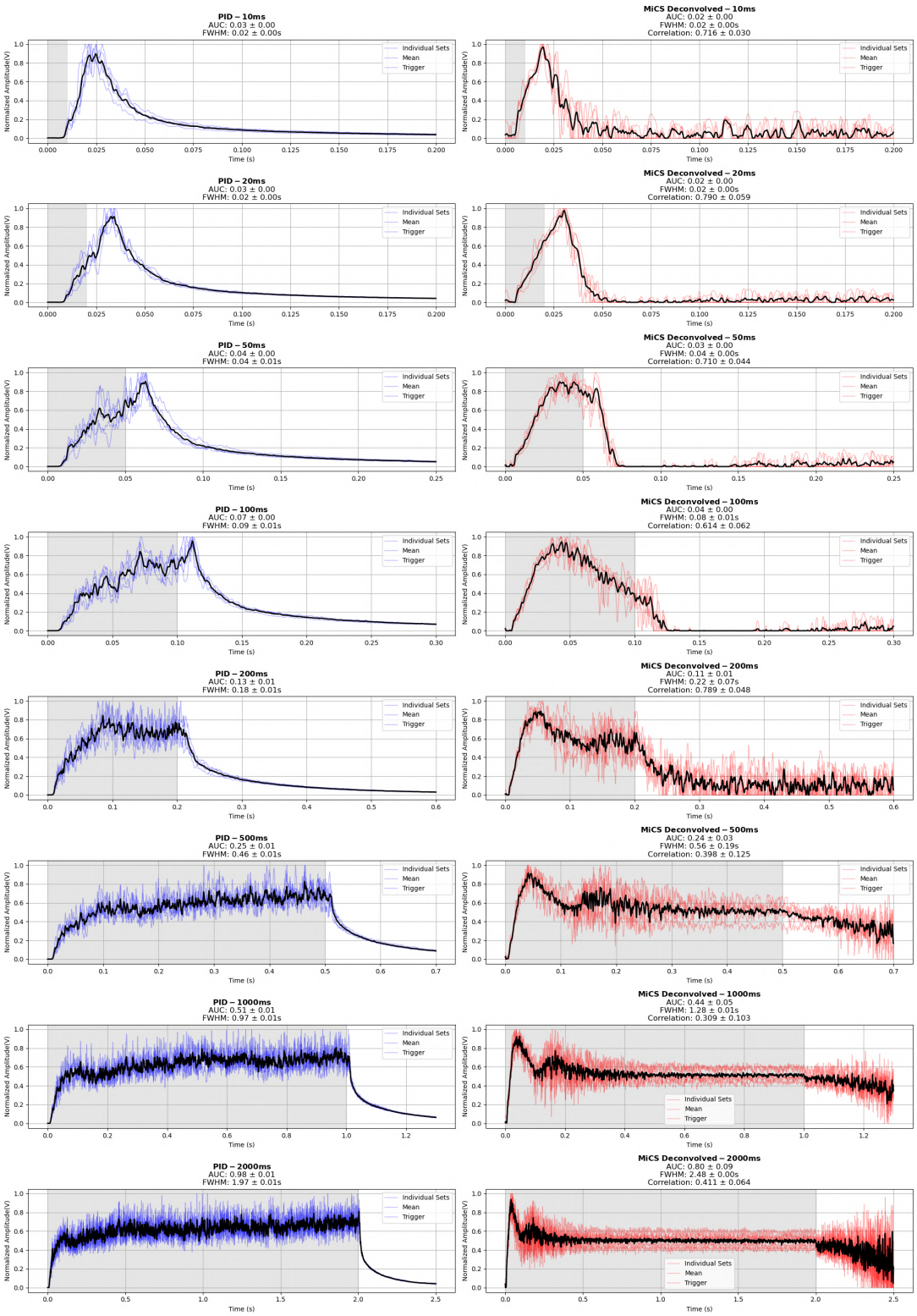

Figure 3.1: PID and MiCS deconvolved signals in response to simple pulses of different durations in the following order: 10 ms, 20 ms, 50 ms, 100 ms, 200 ms, 500 ms, 1000 ms, 2000 ms. PID repeats (blue, n=5), MiCS deconvolved repeats (red , n=5), Mean of PID and MiCS deconvolved repeats (black) and Odour presentation (grey)

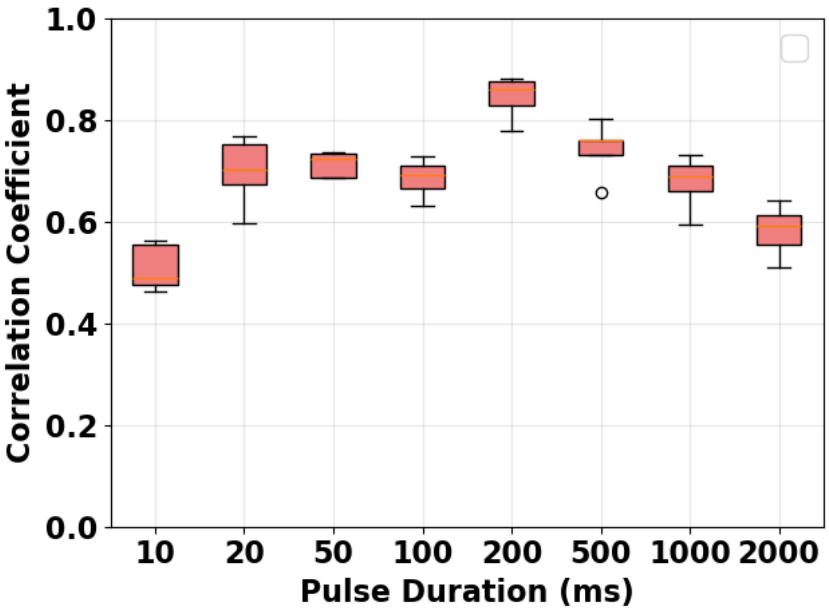

Figure 3.2: Correlation between MiCS deconvolved and PID signals across different pulse durations

The correlation coefficient between MiCS deconvolved and PID signals generally remains high across all pulse durations (Figure 3.2), ranging between 0.5-0.85, with the highest values observed at 200 ms. This indicates a strong similarity between the two signal types across most pulse durations.

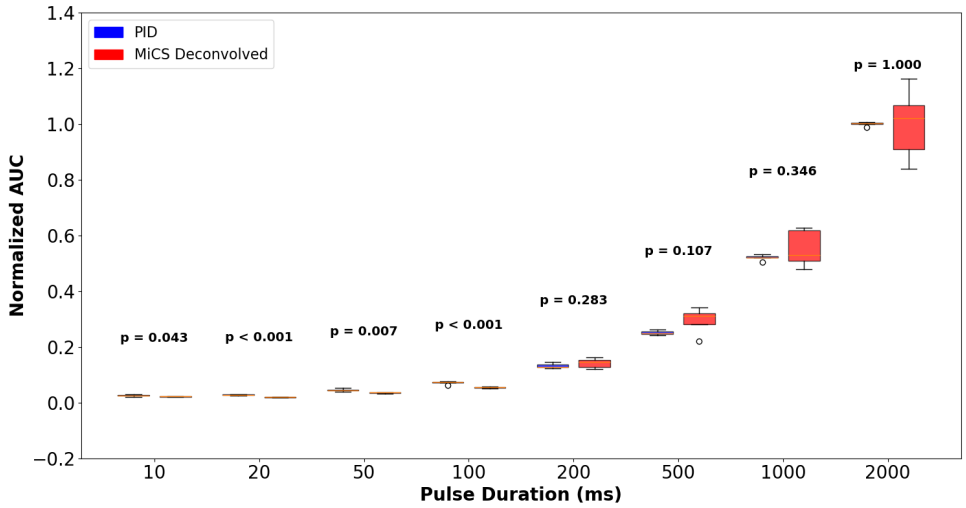

(a)

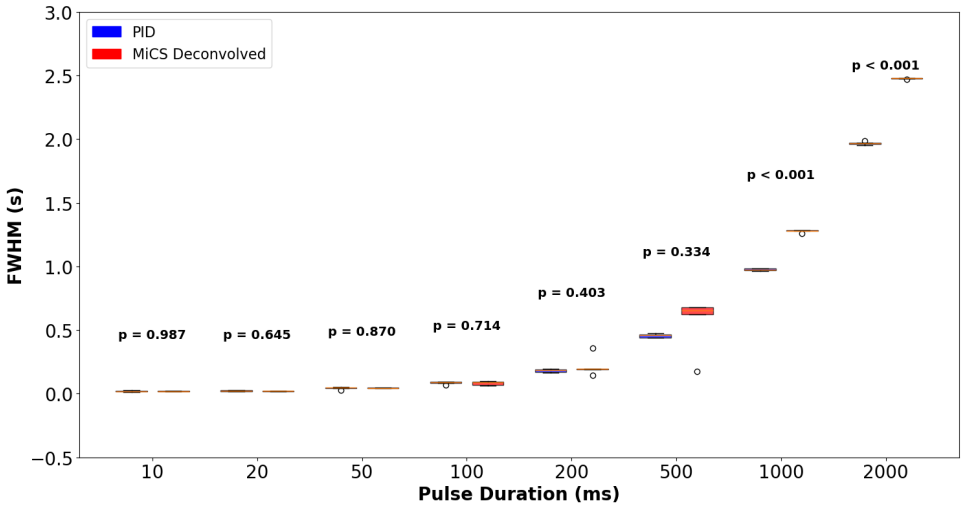

(b)

Figure 3.3: (a) Normalised Area under the Curve and (b) Full Width Half Maxima comparing PID and MiCS deconvolved signals for simple pulses of different durations, PID (blue) and MiCS deconvolved (red), p-values from unpaired t-tests for individual pulse durations

When comparing the normalised AUC of PID and MiCS deconvolved signals across various pulse durations (Figure 3.3 (a)), we found that both PID and MiCS deconvolved signals normalised AUC values increase with pulse duration, reflecting good signal integration over time. Variability is slightly higher for MiCS at longer durations, as indicated by wider boxplots. For shorter pulse durations (10-100 ms), the MiCS deconvolved signal shows notable differences in normalised AUC compared to the PID signal ($p < 0.05$). However, as the pulse duration increases, particularly beyond 200 ms, the two signals converge ($p > 0.05$).

When comparing the FWHM of PID and MiCS deconvolved signals across different pulse durations (Figure 3.3 (b)), we found that both PID and MiCS deconvolved FWHM values increase with pulse duration, as expected due to longer signal widths at longer pulses. The MiCS deconvolved signal FWHM closely follows the PID trend but exhibits slight deviations, particularly at longer durations where the FWHM values are higher for MiCS ($p < 0.001$). At shorter durations (100 ms), the match between PID and MiCS deconvolved signal FWHM is nearly perfect ($p > 0.05$).

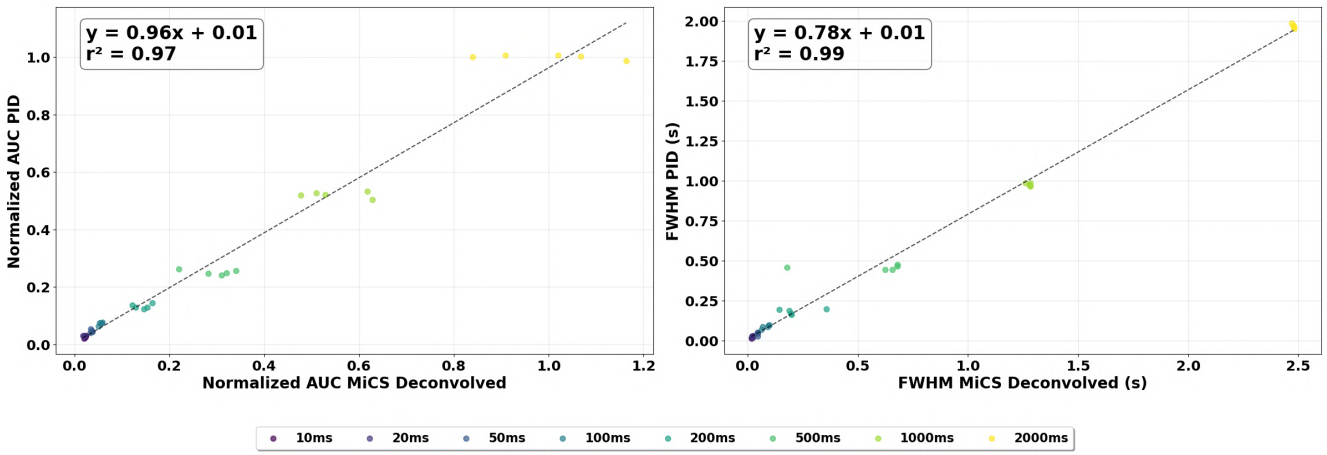

Figure 3.4: Linear Correlation between PID and MiCS deconvolved signal for Normalised AUC and FWHM

Linear regression analysis was done to study the linear relationships between MiCS deconvolved and PID signals for the two metrics (Figure 3.4). The high r^2 values (0.97 for AUC and 0.99 for FWHM) indicate excellent similarity between MiCS deconvolved and PID signals for both metrics. The slopes (0.96 for AUC and 0.78 for FWHM) suggest that MiCS slightly underestimates these parameters compared to PID.

3.1.2 Ethyl Butyrate

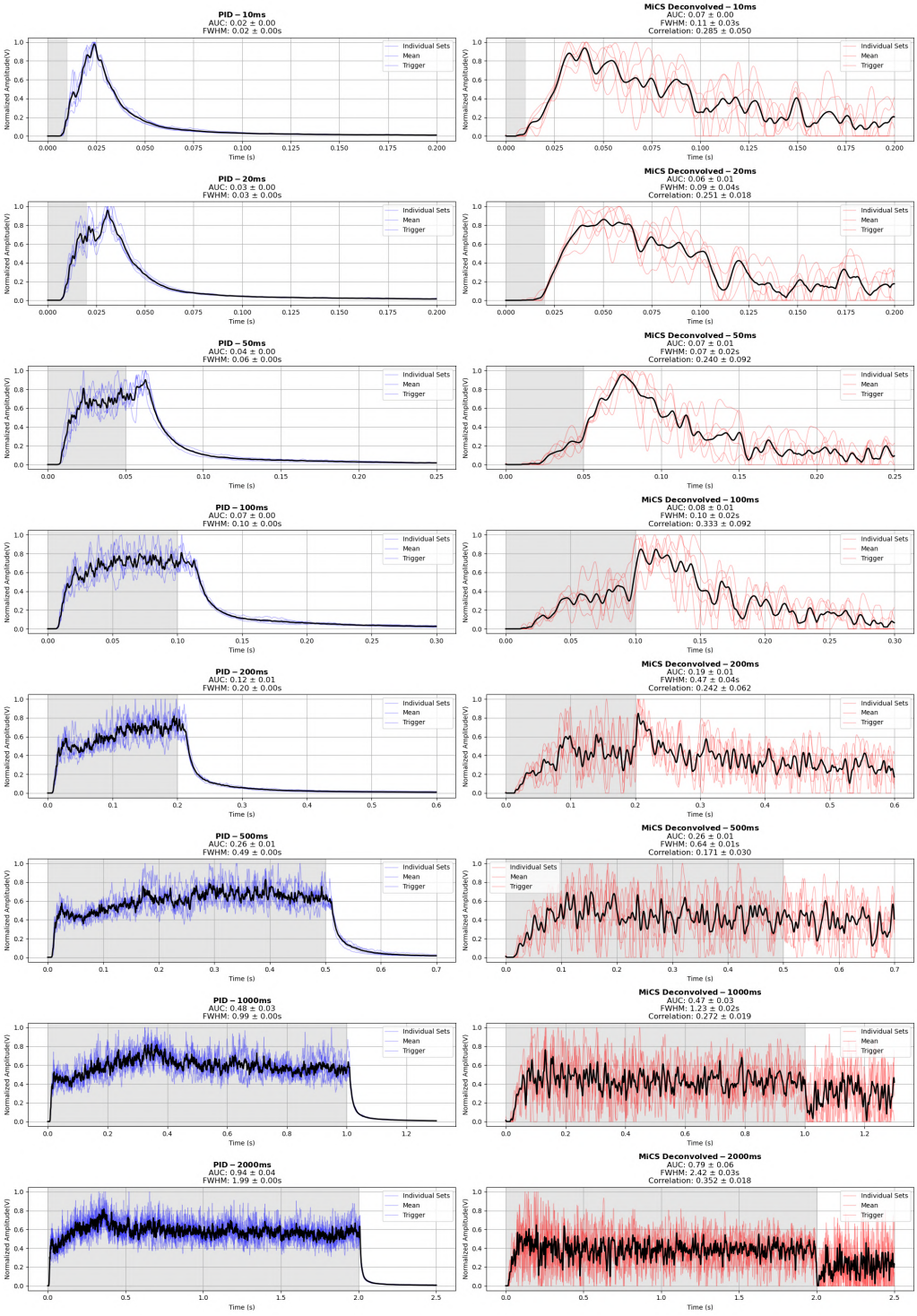

Figure 3.5: PID and MiCS deconvolved signals in response to simple pulses of different durations in the following order: 10 ms, 20 ms, 50 ms, 100 ms, 200 ms, 500 ms, 1000 ms, 2000 ms. PID repeats (blue, n=5), MiCS deconvolved repeats (red , n=5), Mean of PID and MiCS deconvolved repeats (black) and Odour presentation (grey)

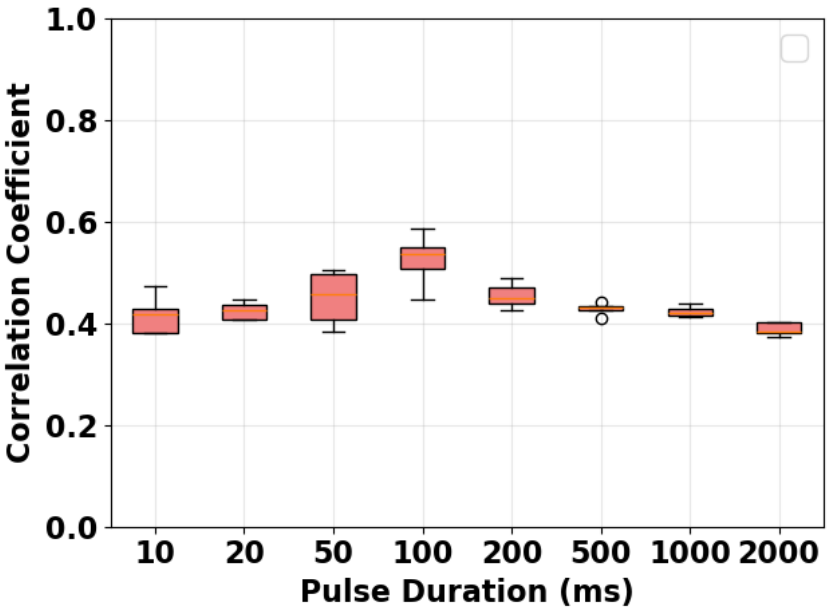

Figure 3.6: Correlation between MiCS deconvolved and PID signals across different pulse durations

The correlation coefficient between MiCS deconvolved and PID signals remains relatively consistent across all pulse durations (Figure 3.6), ranging between 0.4-0.55, with a peak at 100 ms, indicating moderate similarity between the MiCS deconvolved and PID signals.

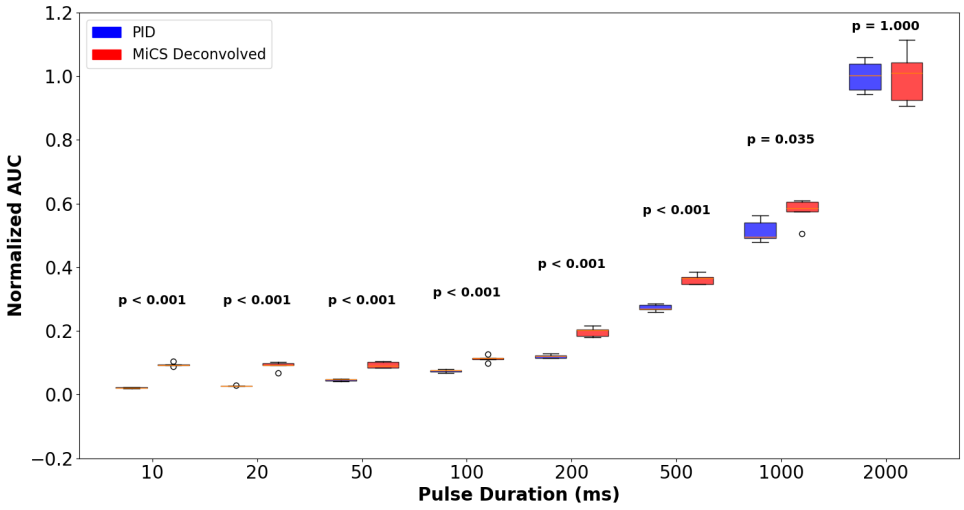

(a)

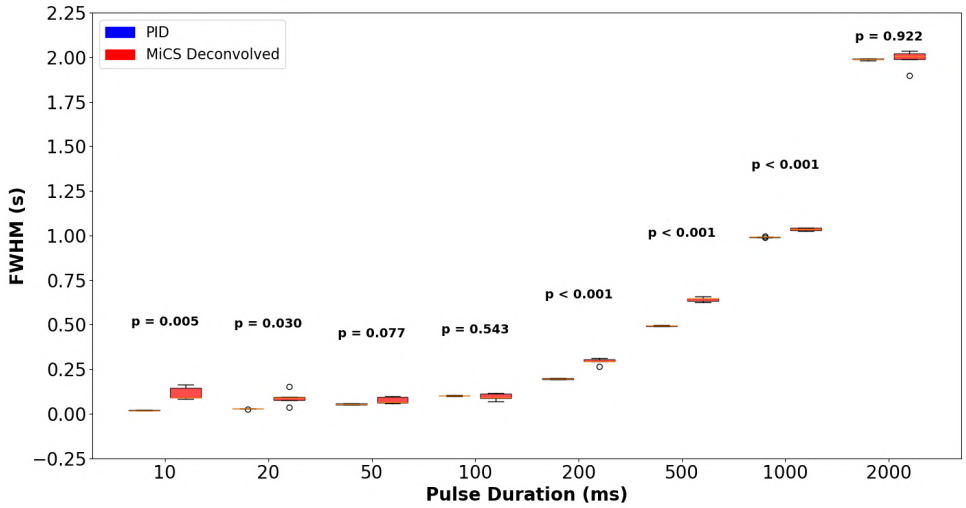

(b)

Figure 3.7: (a) Normalised Area under the Curve and (b) Full Width Half Maxima comparing PID and MiCS deconvolved signals for simple pulses of different durations, PID (blue) and MiCS deconvolved (red), p-values from unpaired t-tests for individual pulse durations

When comparing the normalised AUC of PID and MiCS deconvolved signals across various pulse durations (Figure 3.7 (a)), we found that both signals follow a similar pattern from 10 ms to 2000 ms, with progressive increases becoming more pronounced at durations above 200 ms. The MiCS deconvolved signal consistently shows slightly higher normalised AUC values compared to PID at all durations ($p < 0.05$) except 2000 ms where both signals approach their maximum normalised values ($p = 1$). Variability is slightly higher for MiCS at longer durations, as indicated by wider boxplots.

When comparing the FWHM of PID and MiCS deconvolved signals across different pulse durations (Figure 3.7 (b)), we found that the MiCS deconvolved signal FWHM trend is uneven among itself and in comparison with PID for shorter pulses ($p < 0.05$ for 10 ms and 20 ms pulse durations and $p > 0.05$ for 50 ms and 100 ms pulse durations). For pulse durations from 200 ms to 1000 ms MiCS FWHM is higher than PID FWHM ($p < 0.001$) and both signals approach their maximum normalised values for 2000 ms pulse duration ($p = 0.922$).

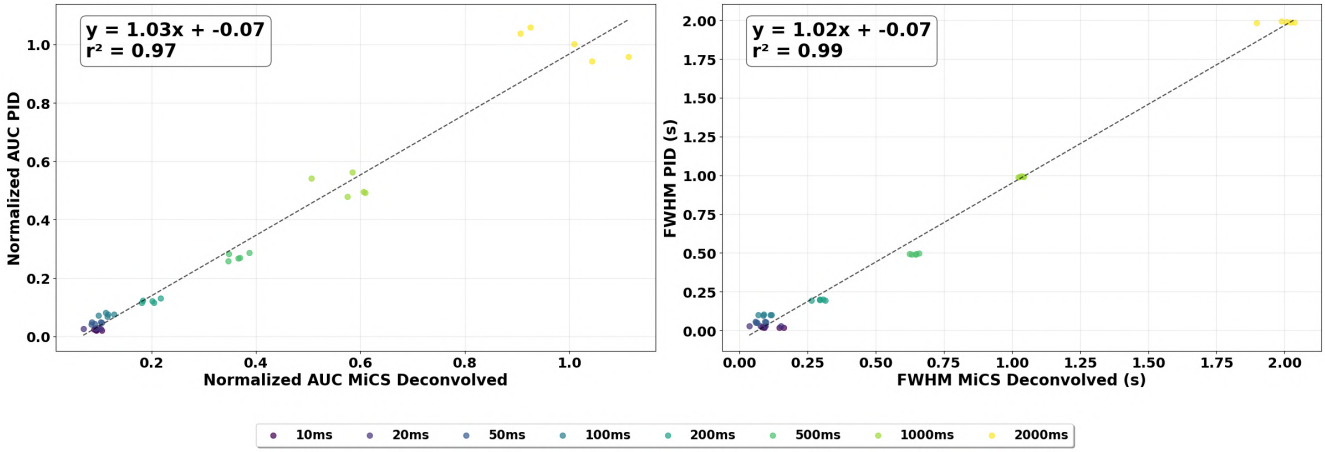

Figure 3.8: Linear Correlation between PID and MiCS deconvolved for normalised AUC and FWHM

Linear regression analysis (Figure 3.8) shows high r^2 values (0.97 for AUC and 0.99 for FWHM) indicating excellent similarity between MiCS deconvolved and PID signals for both metrics. The slopes (1.03 for AUC and 1.02 for FWHM) suggest that MiCS slightly overestimates these parameters compared to PID.

3.1.3 Acetophenone

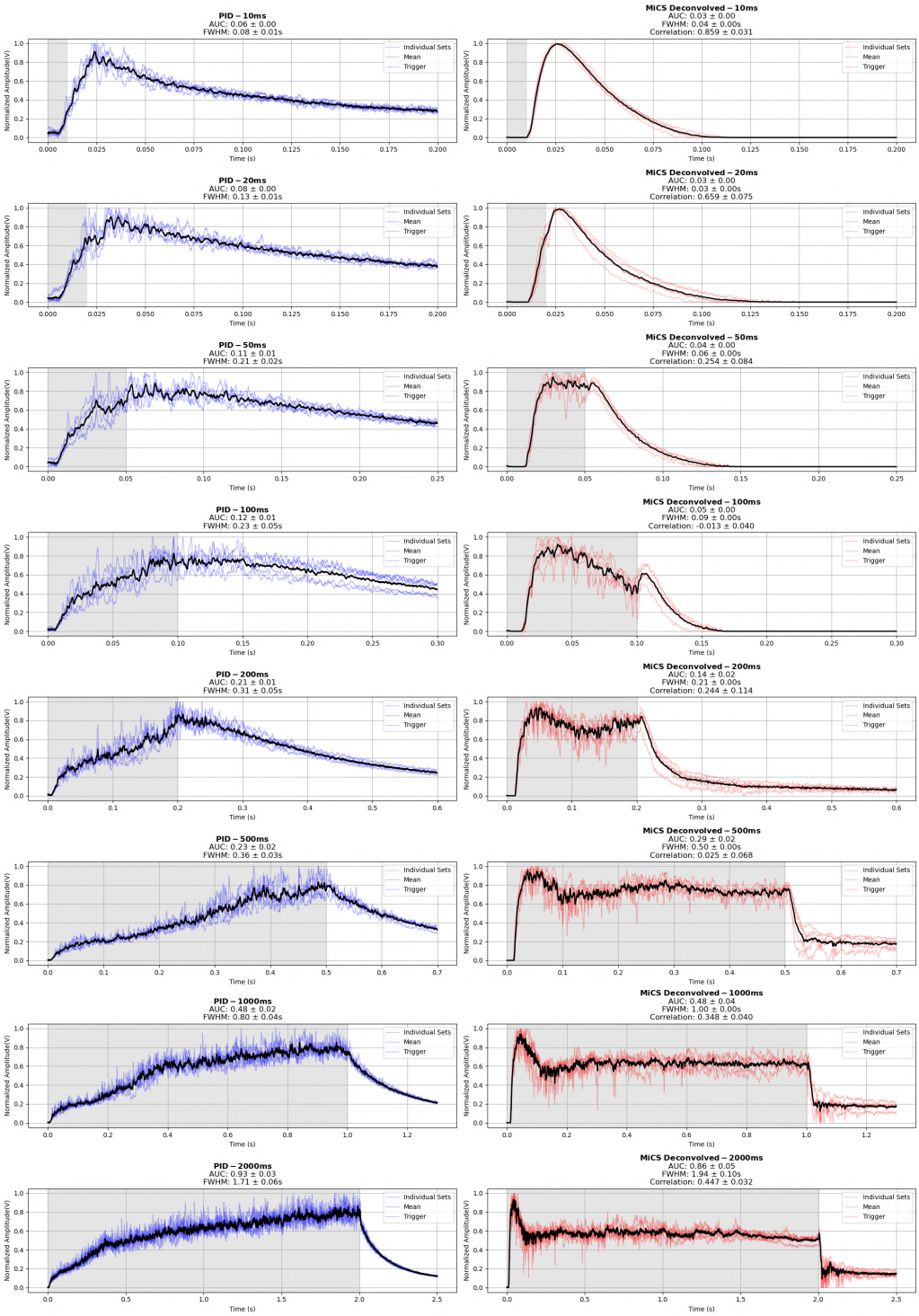

Figure 3.9: PID and MiCS deconvolved signal in response to simple pulses of different durations in the following order: 10 ms, 20 ms, 50 ms, 100 ms, 200 ms, 500 ms, 1000 ms, 2000 ms. PID repeats (blue, n=5), MiCS deconvolved repeats (red , n=5), Mean of PID and MiCS deconvolved repeats (black) and Odour presentation (grey)

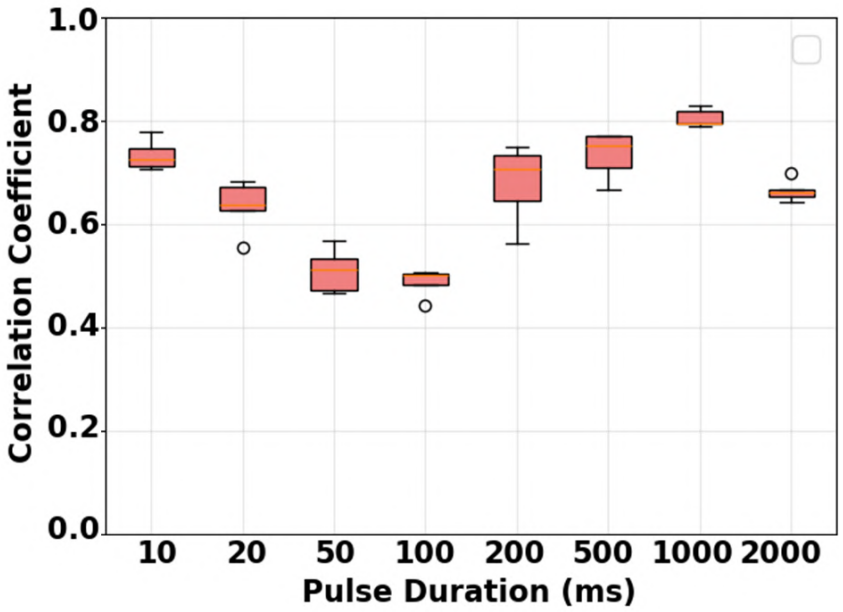

Figure 3.10: Correlation between MiCS deconvolved and PID signals across different pulse durations

The correlation coefficient between MiCS deconvolved and PID signals remains high across most pulse durations (Figure 3.10), ranging between 0.5-0.85, with the highest values observed at 1000 ms. This indicates a strong similarity between the two signal types across most durations.

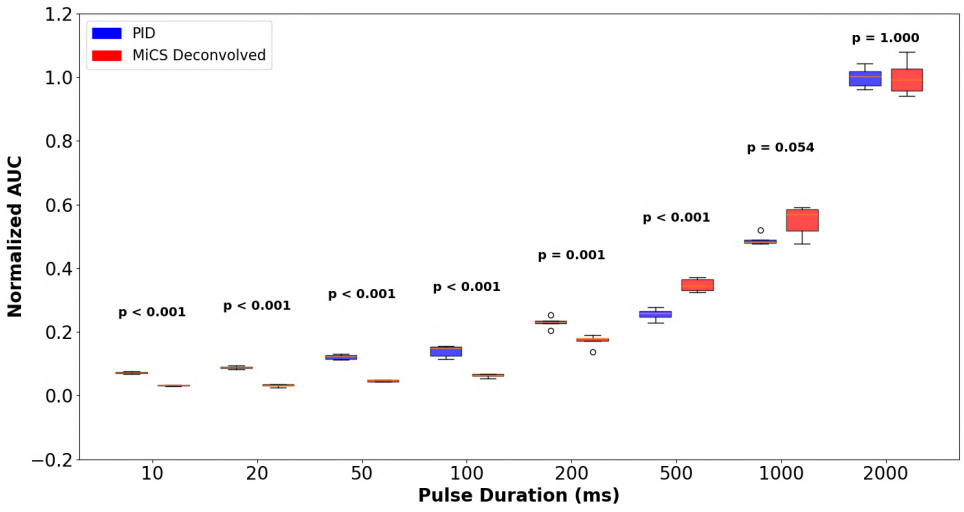

(a)

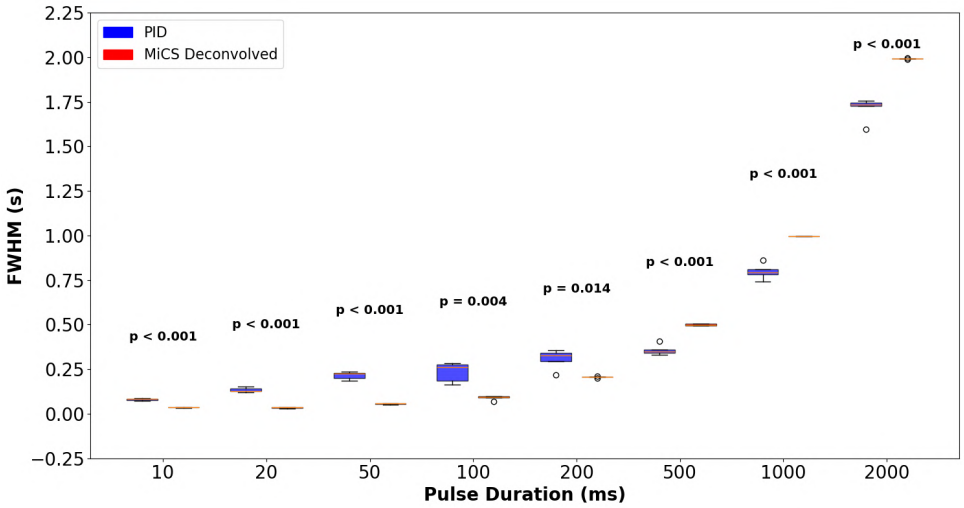

(b)

Figure 3.11: (a) Normalised Area under the Curve and (b) Full Width Half Maxima comparing PID and MiCS deconvolved signals for simple pulses of different durations, PID (blue) and MiCS deconvolved (red), p-values from unpaired t-tests for individual pulse durations

When comparing the normalised AUC of PID and MiCS deconvolved signals across various pulse durations (Figure 3.11 (a)), we found that both PID and MiCS deconvolved signals normalised AUC values increase with pulse duration, reflecting good signal integration over time. The similarity between PID and MiCS AUC shows some deviations, with PID showing higher values till 200 ms ($p < 0.001$) but MiCS showing higher values at 500 ms ($p < 0.001$) & 1000 ms ($p = 0.054$). At 2000 ms, both signals approach similar normalised values ($p = 1$).

When comparing the FWHM of PID and MiCS deconvolved signals across different pulse durations (Figure 3.11 (b)), we found that both signals show increasing FWHM values with pulse duration. The PID signal shows higher FWHM values compared to MiCS deconvolved signals across all pulse durations till 200 ms while MiCS deconvolved signal displays higher FWHM from 500 ms to 2000 ms ($p < 0.05$ for all pulse durations).

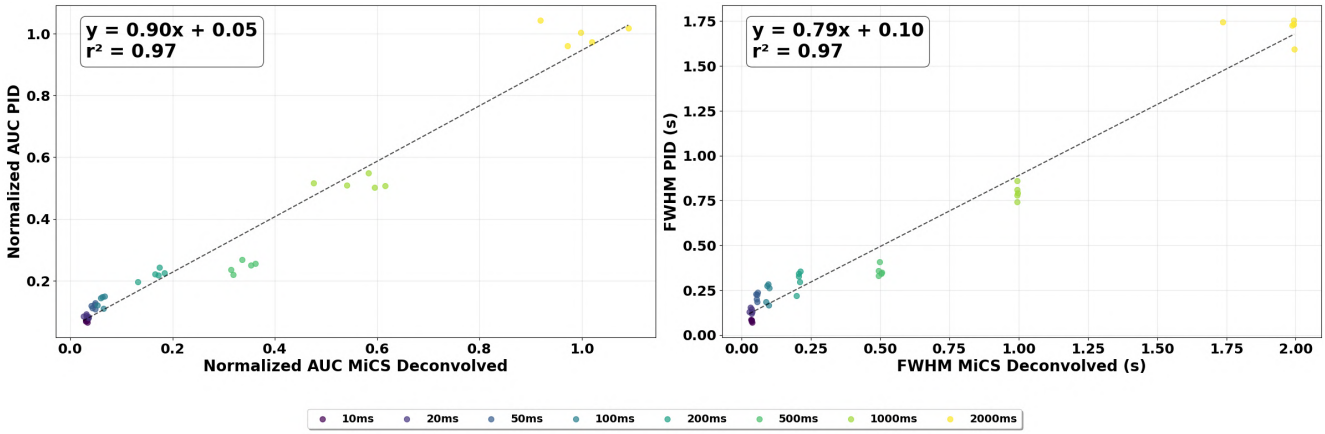

Figure 3.12: Linear Correlation between PID and MiCS for normalised AUC and FWHM

Linear regression analysis (Figure 3.12) shows high r^2 values (0.97 for both AUC and FWHM) indicating excellent similarity between MiCS deconvolved and PID signals for both metrics. The slopes (0.90 for AUC and 0.79 for FWHM) suggest that MiCS deconvolved slightly underestimates these parameters compared to PID.

3.2 Coupled pulses - tODD

Next, we wanted to investigate if the sensor can resolve temporally close stimuli or if it integrates this as a single event. Coupled pulses were recorded to study the ability of the sensor to resolve two pulses separated by varying inter-stimulus intervals. The odorants used are Alpha Terpinene, Ethyl Butyrate and Acetophenone.

3.2.1 Alpha Terpinene

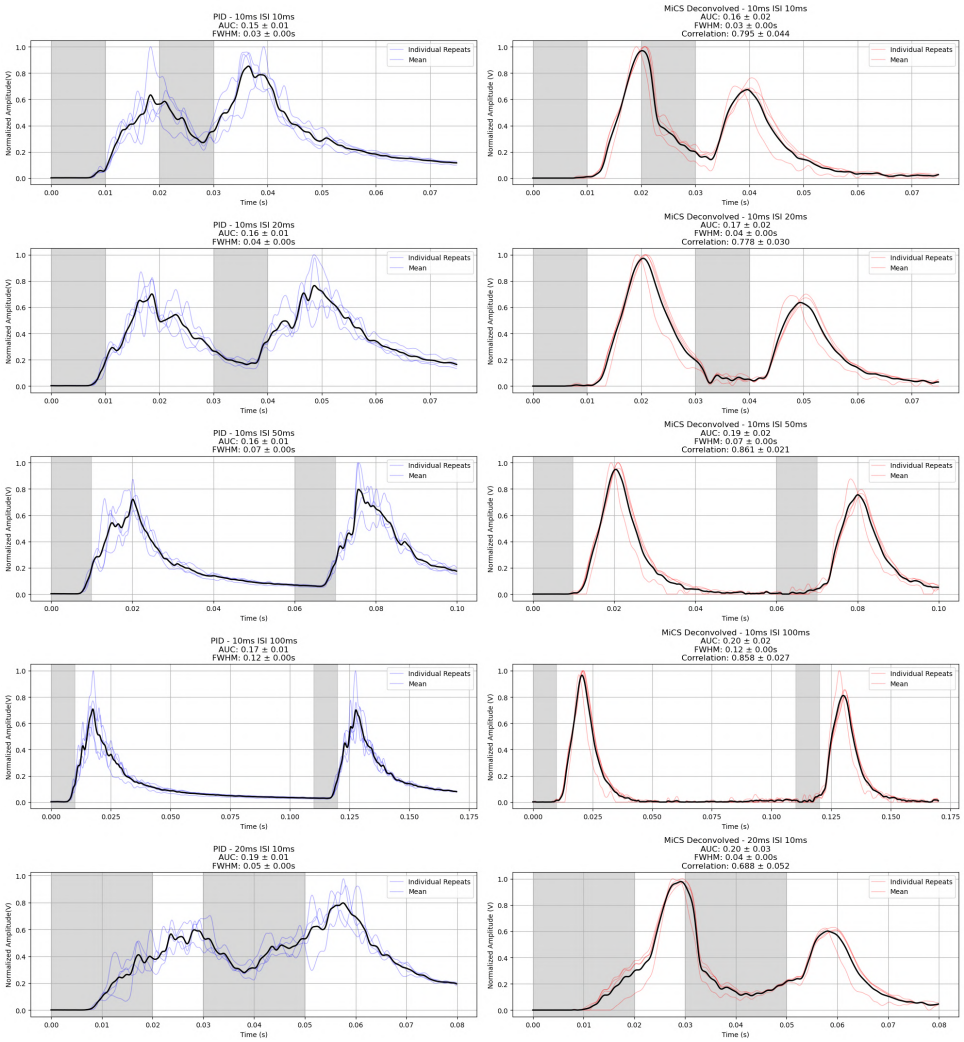

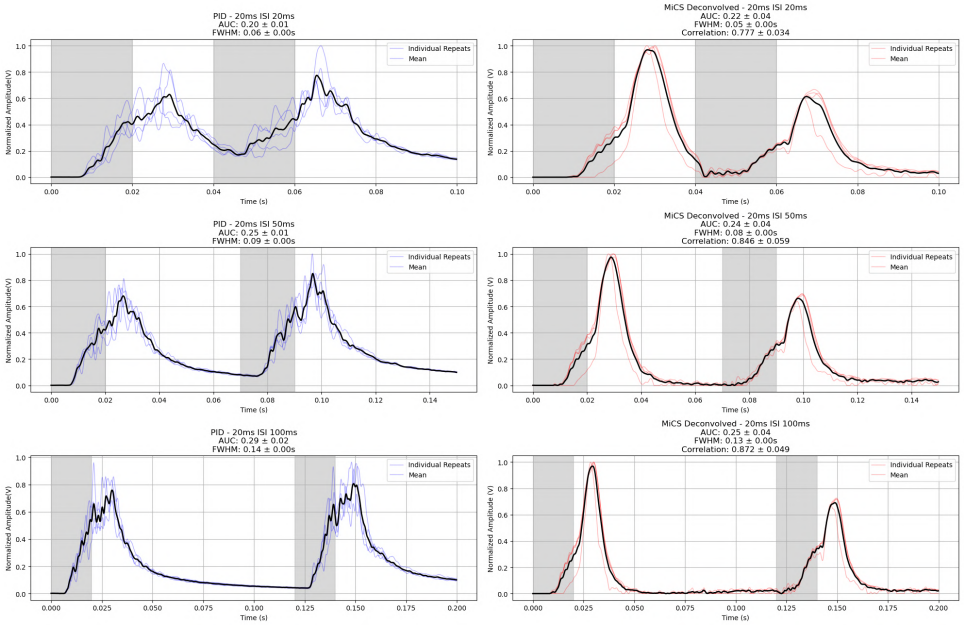

Figure 3.13: PID and MiCS response to coupled pulses of following pulse width and inter-stimulus interval in the order: 10 ms / 10 ms, 10 ms / 20 ms , 10 ms / 50 ms, 10 ms / 100 ms, 20 ms / 10 ms, 20 ms / 20 ms, 20 ms / 50 ms, 20 ms / 100 ms. PID repeats (blue, n=5), MiCS deconvolved repeats (red , n=5), Mean of PID and MiCS deconvolved repeats (black) and Odour presentation (grey)

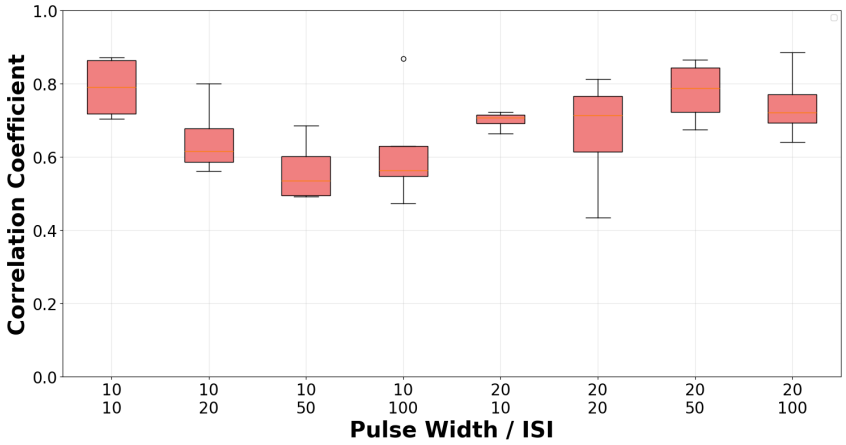

Figure 3.14: Correlation between MiCS Deconvolved and PID signals across different pulse width-ISI combinations. The x-axis contains the pulse widths (10 ms and 20 ms) with different ISI combinations (10 ms, 20 ms, 50 ms and 100 ms)

The correlation coefficient between MiCS deconvolved signals and PID signals across different pulse width-ISI combinations ranges between 0.5 and 0.83 (Figure 3.14).

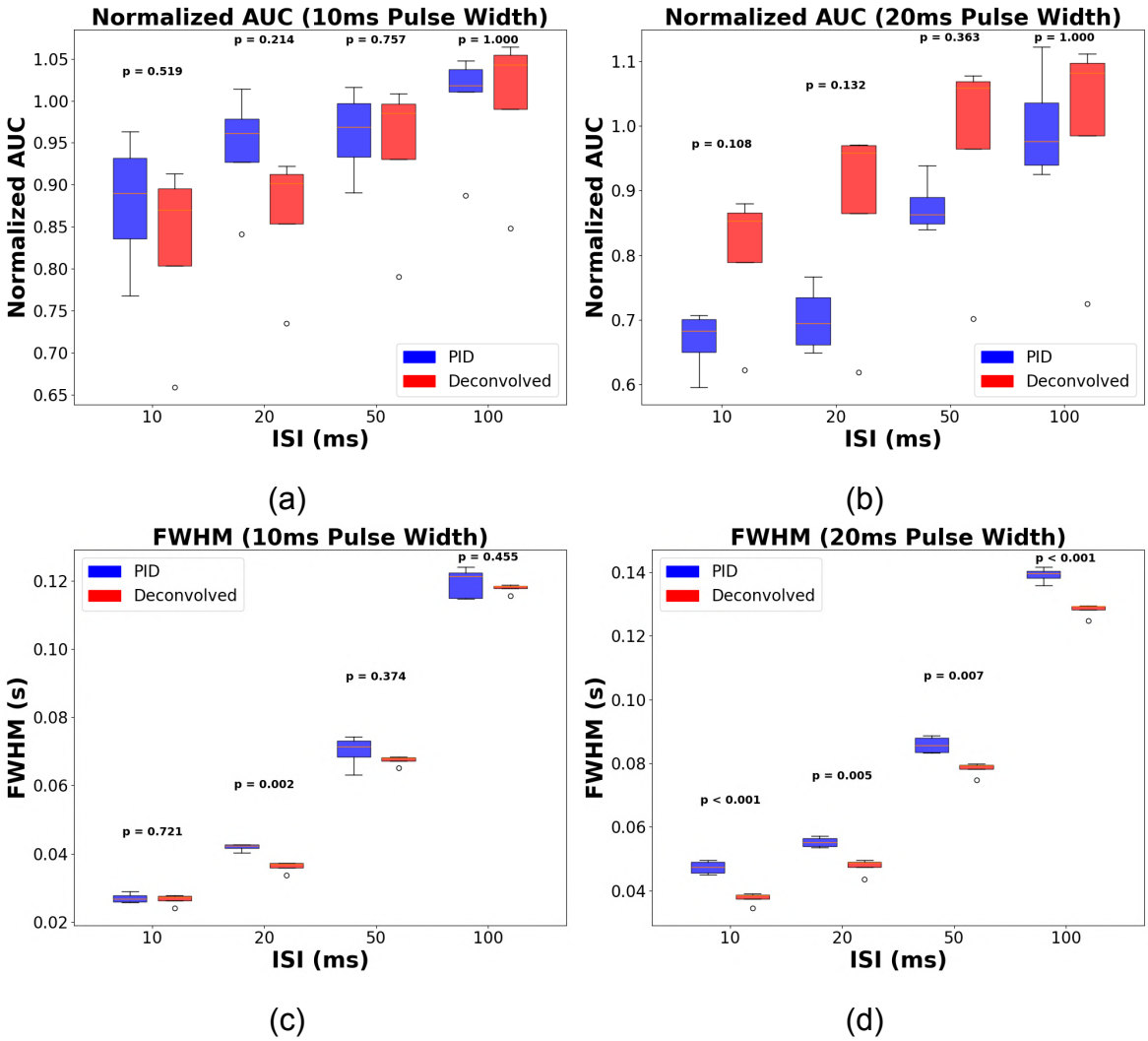

Figure 3.15: Normalised Area under the Curve of (a) 10 ms pulses, (b) 20 ms pulses and Full Width Half Maxima of (c) 10 ms pulses, (d) 20 ms pulses comparing PID and MiCS deconvolved signals for coupled pulses of different durations, PID (blue) and MiCS deconvolved (red), p-values from unpaired t-tests for individual pulse width-ISI combinations

For coupled pulses of 10 ms pulse width (Figure 3.15 (a)), both signal types show an increasing trend in normalised AUC as the ISI increases. PID signal have higher normalised AUC values than MiCS deconvolved signal at lower ISI values ($p > 0.05$). At higher ISI values (50 ms, 100 ms), the values becomes more comparable ($p > 0.05$).

For coupled pulses of 20 ms pulse width (Figure 3.15 (b)), the trend is similar but more pronounced, with normalised AUC increasing with ISI values. MiCS deconvolved signals consistently show higher normalised AUC values compared to PID signals across all ISI values ($p > 0.05$). The difference between PID and MiCS deconvolved signals is significant at lower ISI values (10 ms, 20 ms).

For coupled pulses of 10 ms pulse width(Figure 3.15 (c)), FWHM increases with ISI for both signal types. MiCS deconvolved signal consistently show lower FWHM values than PID signal across all ISI values ($p > 0.05$ for all ISI values except 20 ms). Box heights are generally smaller for MiCS deconvolved signals, indicating less variability.

For coupled pulses of 20 ms pulse width(Figure 3.15 (d)), FWHM increases with ISI for both signal types. MiCS deconvolved signals consistently show lower FWHM values than PID signals across all ISI values ($p < 0.05$). The difference between PID and MiCS deconvolved signals appears more consistent across ISI values. Both signal types show a steep increase in FWHM as ISI increases.

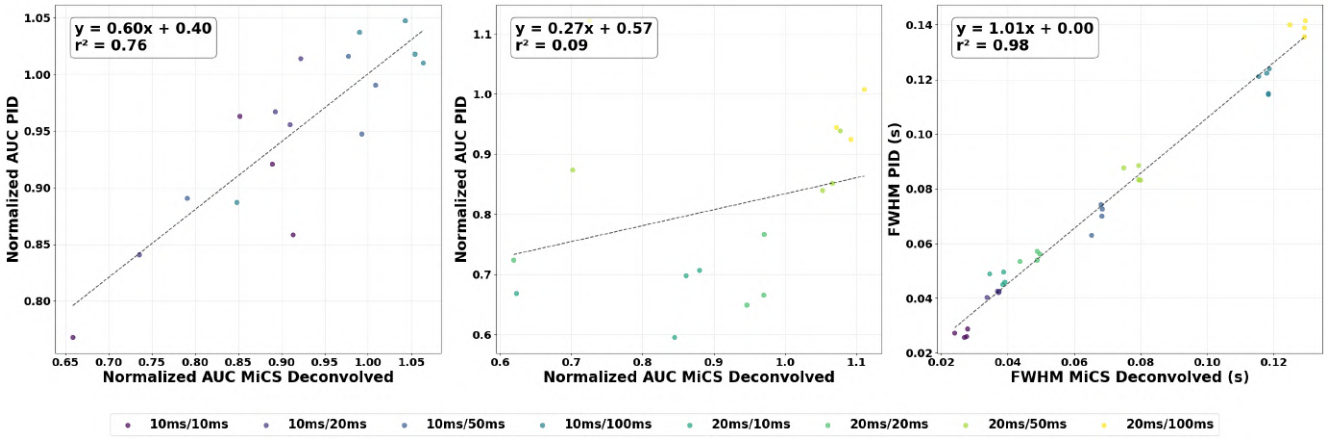

Figure 3.16: Linear Correlation between PID and MiCS for normalised AUC and FWHM

Linear regression analysis (Figure 3.16) shows a positive correlation ($r^2 = 0.76$) between normalised AUC values of both signal types for the 10 ms pulse data, while the 20 ms pulse correlation is weaker ($r^2 = 0.09$). The FWHM values of PID and MiCS deconvolved signals demonstrate an almost perfect correlation ($r^2 = 0.98$) with a slope of 1.01.

3.2.2 Ethyl Butyrate

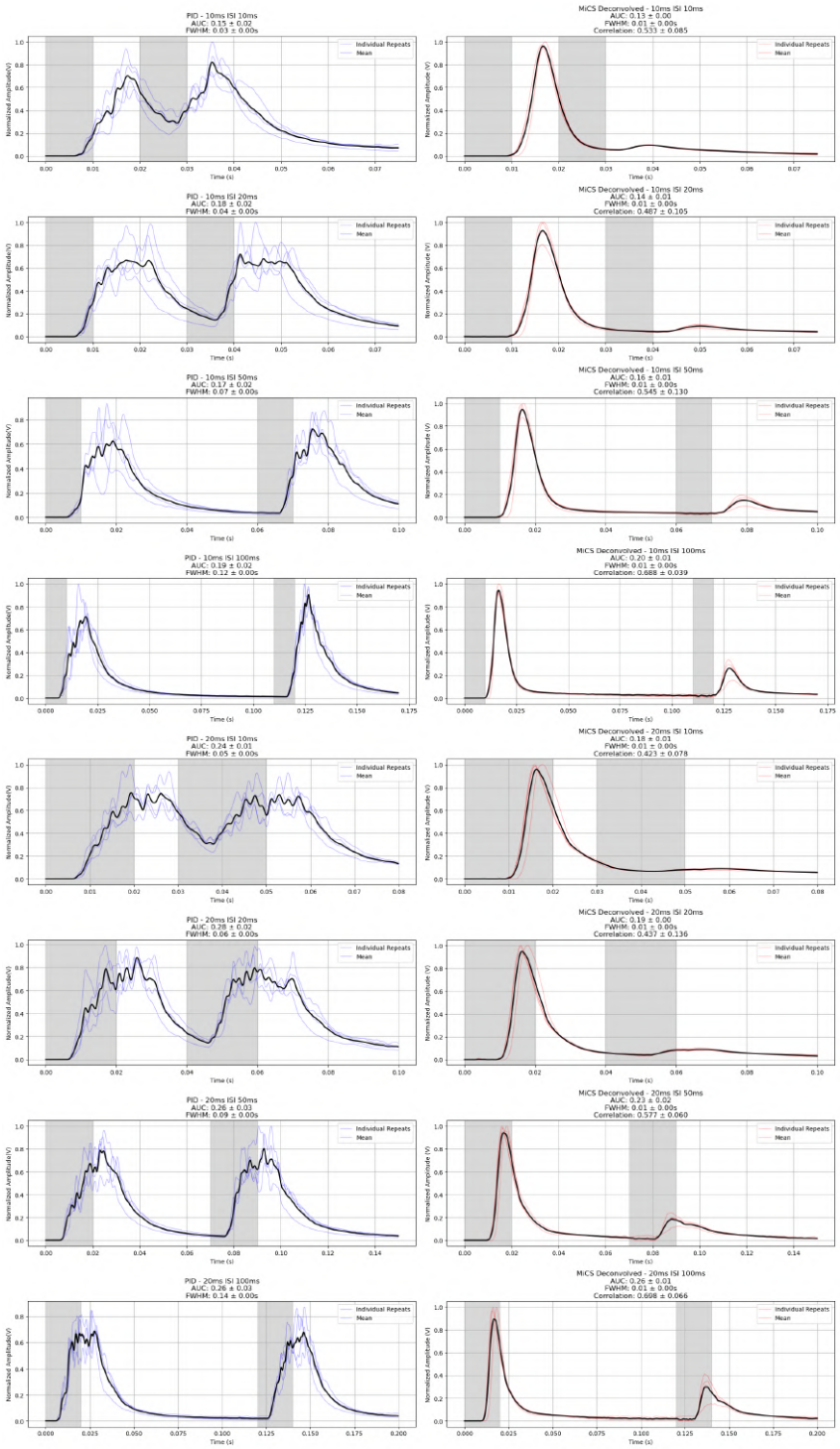

Figure 3.17: PID and MiCS response to coupled pulses of following pulse width and inter-stimulus interval in the order: 10 ms / 10 ms, 10 ms / 20 ms , 10 ms / 50 ms, 10 ms / 100 ms, 20 ms / 10 ms, 20 ms / 20 ms, 20 ms / 50 ms, 20 ms / 100 ms. PID repeats (blue, n=5), MiCS deconvolved repeats (red , n=5), Mean of PID and MiCS deconvolved repeats (black) and Odour presentation (grey)

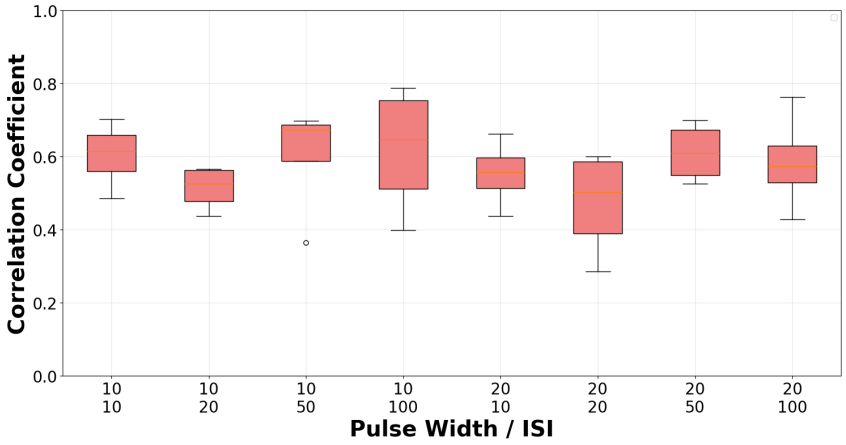

Figure 3.18: Correlation between MiCS Deconvolved and PID signals across different pulse width-ISI combinations. The x-axis contains the pulse widths (10 ms and 20 ms) with different ISI combinations (10 ms, 20 ms, 50 ms and 100 ms)

The correlation coefficient between MiCS deconvolved signals and PID signals across different pulse width-ISI combinations ranges between 0.4 and 0.75 (Figure 3.18).

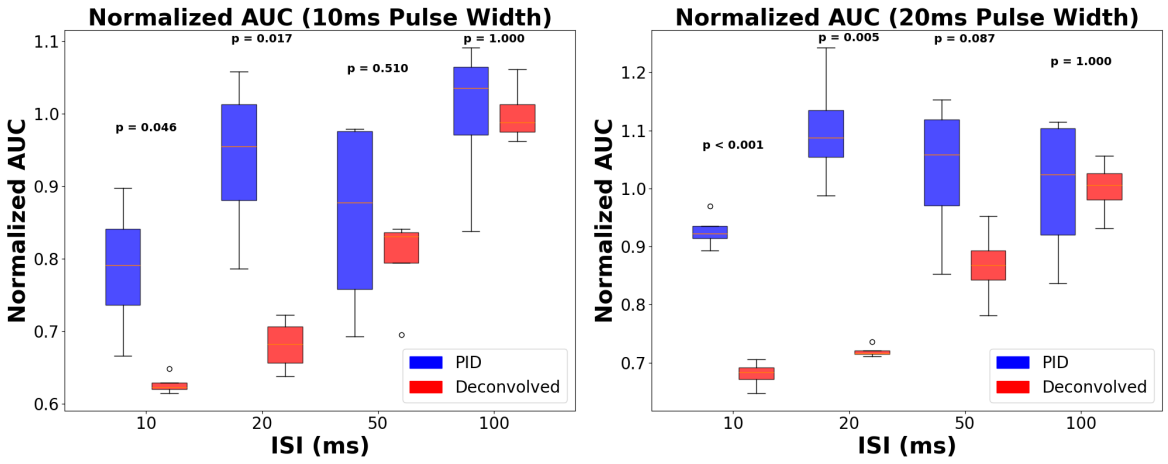

(a) (b)

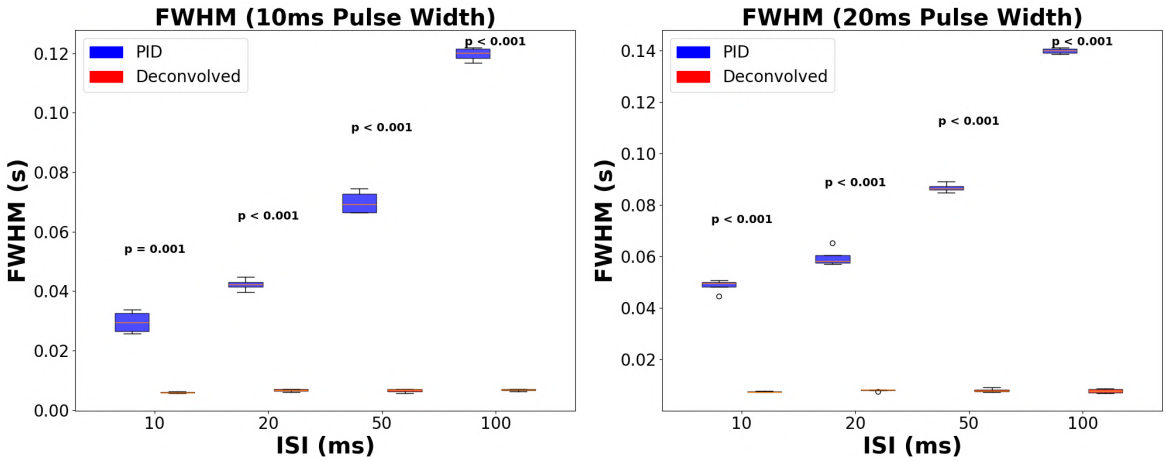

(c) (d)

Figure 3.19: Normalised Area under the Curve of (a) 10 ms pulses, (b) 20 ms pulses and Full Width Half Maxima of (c) 10 ms pulses, (d) 20 ms pulses comparing PID and MiCS deconvolved signals for coupled pulses of different durations, PID (blue) and MiCS deconvolved (red), p-values from unpaired t-tests for individual pulse width-ISI combinations

For coupled pulses of 10 ms pulse width (Figure 3.19 (a)), PID signal shows higher normalised AUC values than MiCS deconvolved signals at lower ISI values (10 ms, 20 ms - $p < 0.05$) and the gap between PID and MiCS deconvolved signals reduces at higher ISI values (50 ms, 100 ms - $p > 0.05$). The variability for PID signals appears greater than for MiCS deconvolved signals for all ISI values.

For coupled pulses of 20 ms pulse width (Figure 3.19 (b)), the trend is similar but more pronounced, with normalised AUC increasing with ISI values. MiCS deconvolved signal consistently shows higher normalised AUC values compared to PID signals across all ISI values. The difference between PID and MiCS deconvolved signals is significant at lower ISI values (10 ms, 20 ms) with $p < 0.05$.

For coupled pulses of 10 ms pulse width, PID signal shows significantly higher FWHM values than MiCS deconvolved signal across all ISI values($p < 0.001$)(Figure 3.19 (c)). PID signal display a strong increasing trend in FWHM as ISI increases. MiCS deconvolved signal maintain consistently low FWHM values regardless of ISI.

There is a similar pattern to 10 ms pulse width observed for 20 ms pulse width ($p < 0.001$) (Figure 3.19 (d)). PID signal show a increasing trend with increasing ISI. MiCS deconvolved signals remain consistently low across all ISI values.

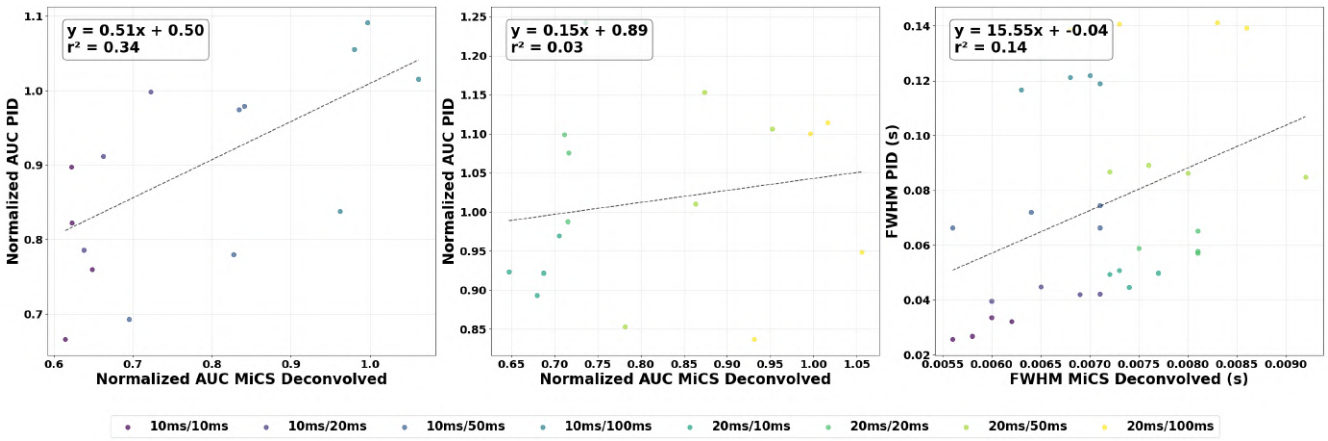

Figure 3.20: Linear Correlation between PID and MiCS for Normalised AUC and FWHM

Linear regression analysis (Figure 3.20) shows a weak correlation ($r^2 = 0.34$) between normalised AUC values of both signal types for the 10 ms pulse data, while the 20 ms pulse correlation is minimal ($r^2 = 0.03$). The FWHM values of PID and MiCS deconvolved signals demonstrate a weak correlation ($r^2 = 0.14$).

3.2.3 Acetophenone

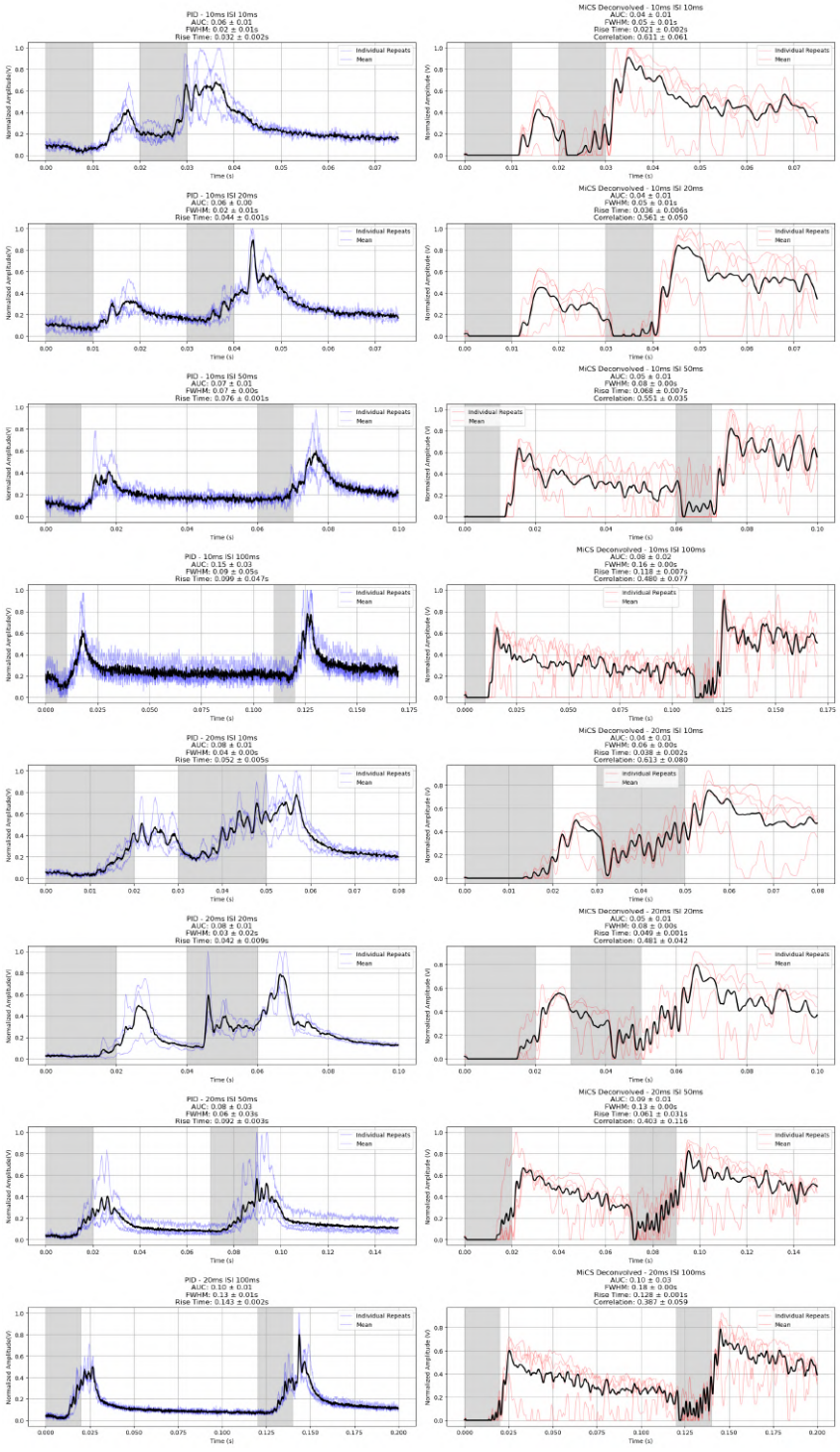

Figure 3.21: PID and MiCS response to coupled pulses of following pulse width and inter-stimulus interval in the order: 10 ms / 10 ms, 10 ms / 20 ms , 10 ms / 50 ms, 10 ms / 100 ms, 20 ms / 10 ms, 20 ms / 20 ms, 20 ms / 50 ms, 20 ms / 100 ms. PID repeats (blue, n=5), MiCS deconvolved repeats (red , n=5), Mean of PID and MiCS deconvolved repeats (black) and Odour presentation (grey)

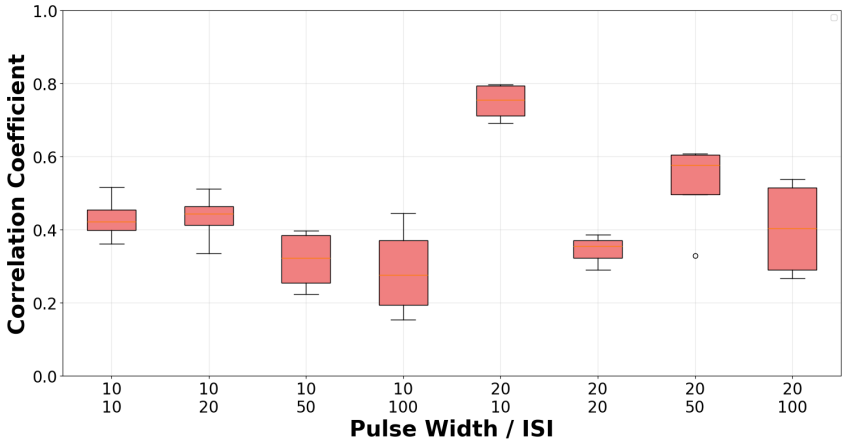

Figure 3.22: Correlation between MiCS Deconvolved and PID signals across different pulse width-ISI combinations. The x-axis contains the pulse widths (10 ms and 20 ms) with different ISI combinations (10 ms, 20 ms, 50 ms and 100 ms)

The correlation coefficient between MiCS deconvolved signals and PID signals across different pulse width-ISI combinations ranges between 0.2 and 0.8 (Figure 3.22).

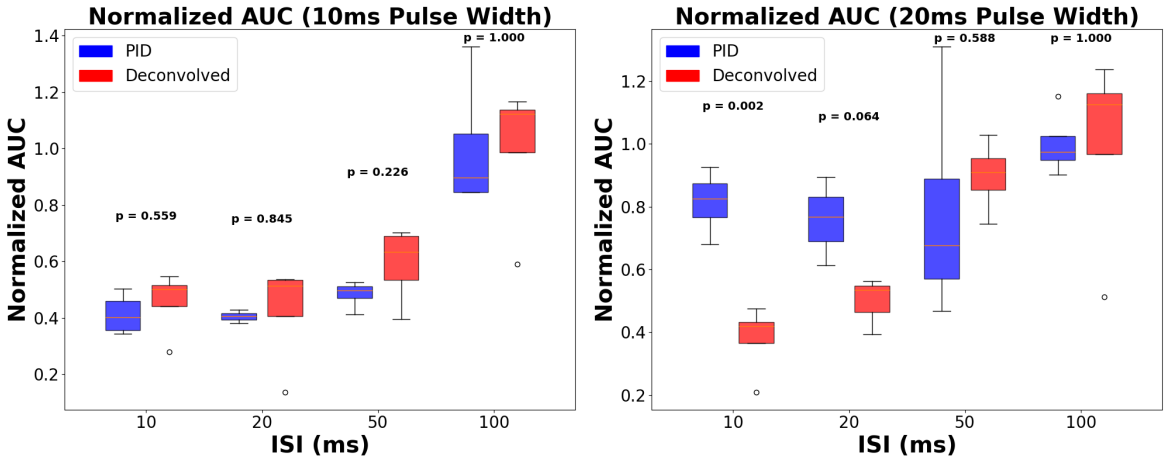

(a) (b)

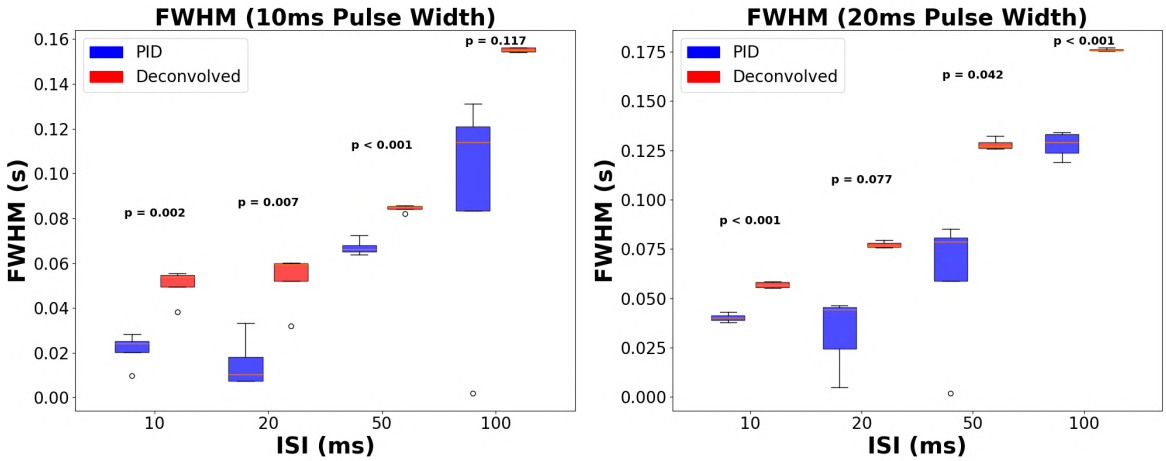

(c) (d)

Figure 3.23: Normalised Area under the Curve of (a) 10 ms pulses, (b) 20 ms pulses and Full Width Half Maxima of (c) 10 ms pulses, (d) 20 ms pulses comparing PID and MiCS deconvolved signals for coupled pulses of different durations, PID (blue) and MiCS deconvolved (red), p-values from unpaired t-tests for individual pulse width-ISI combinations

For coupled pulses of 10 ms pulse width (Figure 3.23 (a)) both PID and MiCS deconvolved signals show an increasing trend in the normalised AUC as ISI increases from 10 ms to 100 ms. MiCS deconvolved signal exhibits slightly higher values than PID signal at all ISI values ($p > 0.05$).

For coupled pulses of 20 ms pulse width (Figure 3.23 (b)), the PID signal show higher normalised AUC values than MiCS deconvolved signals at lower ISI values (10 ms - $p < 0.05$, 20 ms - $p > 0.05$) . The difference between PID and MiCS deconvolved signals decreases at higher ISI values (50 ms, 100 ms - $p > 0.05$) . The MiCS deconvolved signals display an increasing trend with ISI, with values rising steadily from 10 ms to 100 ms.

For coupled pulses of 10 ms pulse width (Figure 3.23 (c)), FWHM values for MiCS deconvolved are consistently higher than PID signals across all ISI values ($p < 0.05$ for all ISI values except 100 ms). The MiCS deconvolved signal display a steadily increasing FWHM trend as ISI increases. PID signal at ISI 100 ms shows high variability.

For coupled pulses of 20 ms pulse width (Figure 3.23 (d)), both PID and MiCS deconvolved signals show an increasing trend in FWHM as ISI increases. FWHM values for MiCS deconvolved are consistently higher than PID signals across all ISI values ($p < 0.05$ for all ISI values except 20 ms).

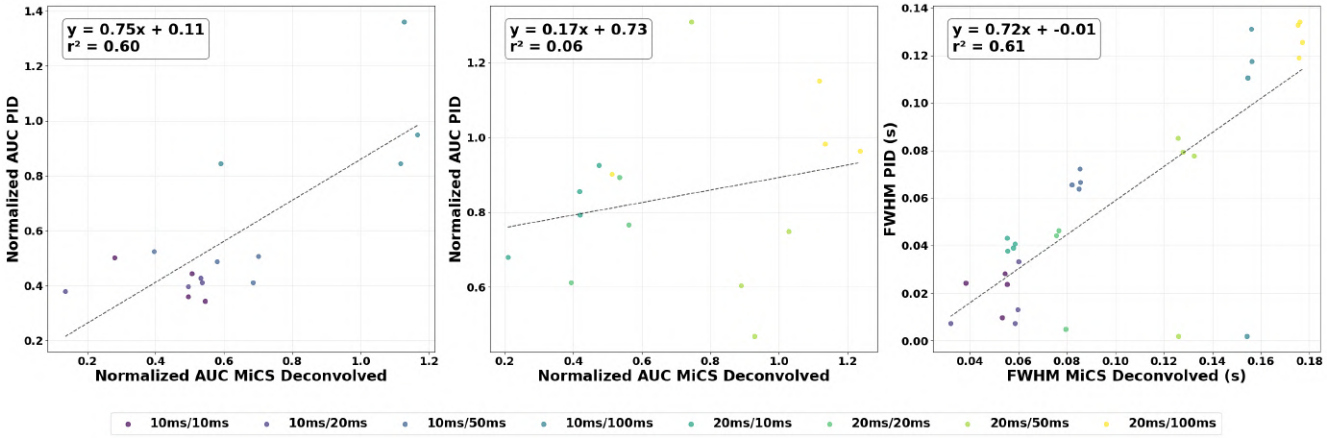

Figure 3.24: Linear Correlation between PID and MiCS deconvolved signals for Normalised AUC and FWHM

Linear regression analysis (Figure 3.24) shows a moderate positive correlation ($r^2 = 0.60$) between normalised AUC values of both signal types for the 10 ms pulse data, while the 20 ms pulse correlation is minimal ($r^2 = 0.06$). The FWHM values of PID and MiCS deconvolved signals demonstrate a moderate positive correlation ($r^2 = 0.61$).

3.3 Simple pulses - 220A Aurora Olfactometer

Simple square pulses of different durations and different concentrations were recorded using PID and MiCS to compare the sensor's ability to differentiate between different concentrations.The odorants used are Alpha Terpinene, Ethyl Butyrate and Acetophenone.

3.3.1 Alpha Terpinene

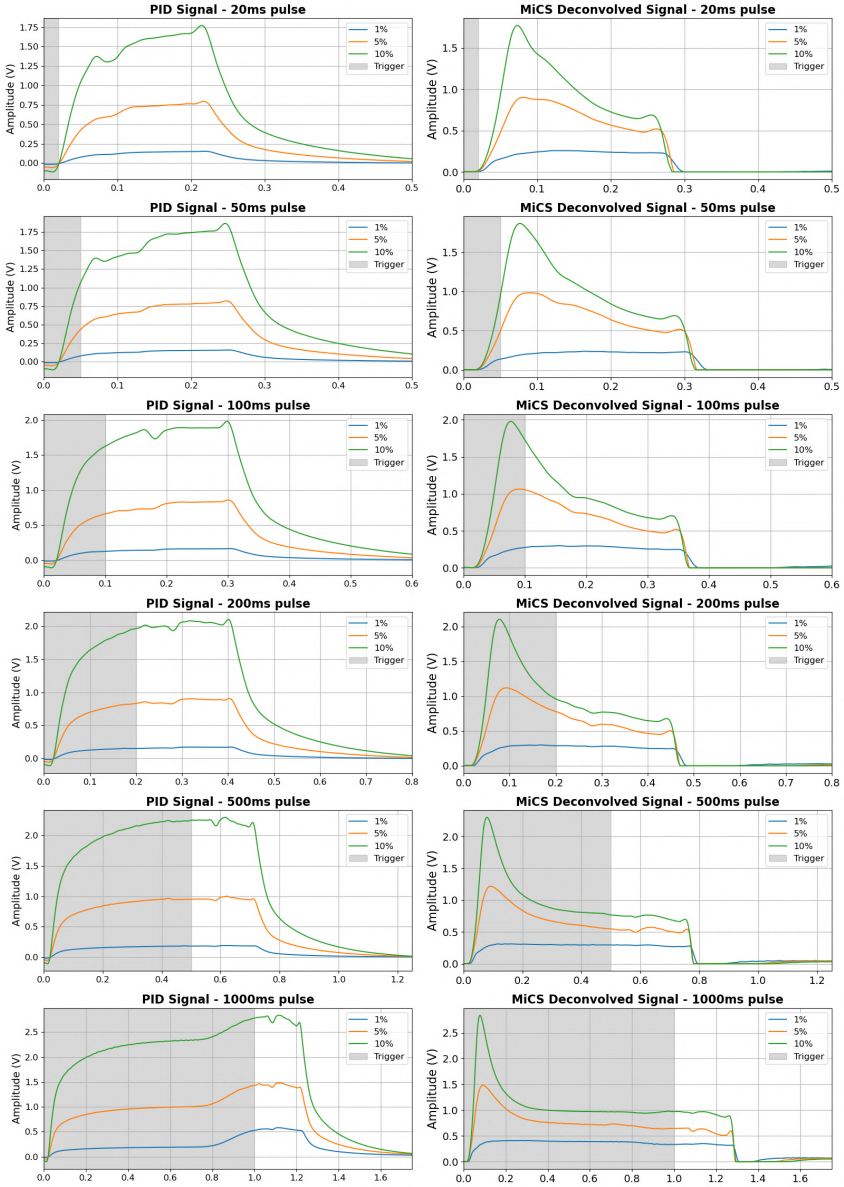

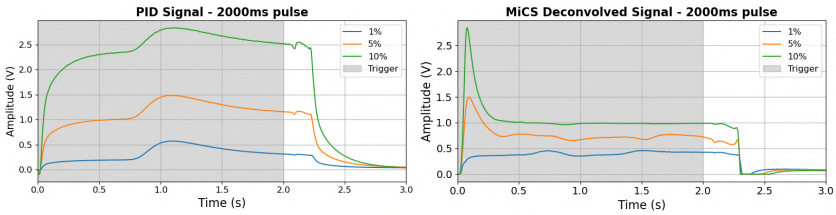

Figure 3.25: Alpha Terpinene simple pulses of different durations and different concentrations. 10%, 5% & 1% concentrations are represented by green, orange and blue colours respectively for both sensors. The signals shown for different concentrations for both sensors are the mean of 5 repeats. Odour presentation (grey)

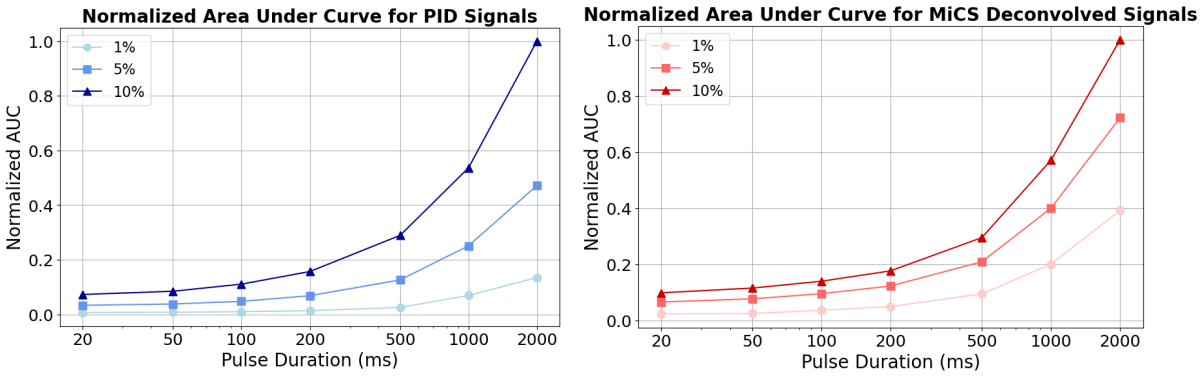

(a) (b)

Figure 3.26: Normalised AUC plots of different concentrations of Alpha Terpinene simple pulses for (a) PID Signal and (b) MiCS deconvolved Signal. PID (blue) and MiCS deconvolved (red). Colour gradient changes from lighter to darker shades with the increase in concentration for both sensors.

Normalised AUC plots for both MiCS deconvolved and PID signals demonstrate similar response patterns. For both devices, the normalised AUC increases exponentially with increasing pulse duration from 20 to 2000 ms, showing a particularly sharp rise between 500 ms and 2000 ms.

The concentration dependence is visible for both sensors, with higher concentrations (10%) consistently producing higher normalised AUC values compared to lower (5% and low (1%) concentrations across all pulse durations. This concentration-dependent response is maintained throughout the pulse duration range, confirming the sensors' ability to differentiate between concentration levels.

3.3.2 Ethyl Butyrate

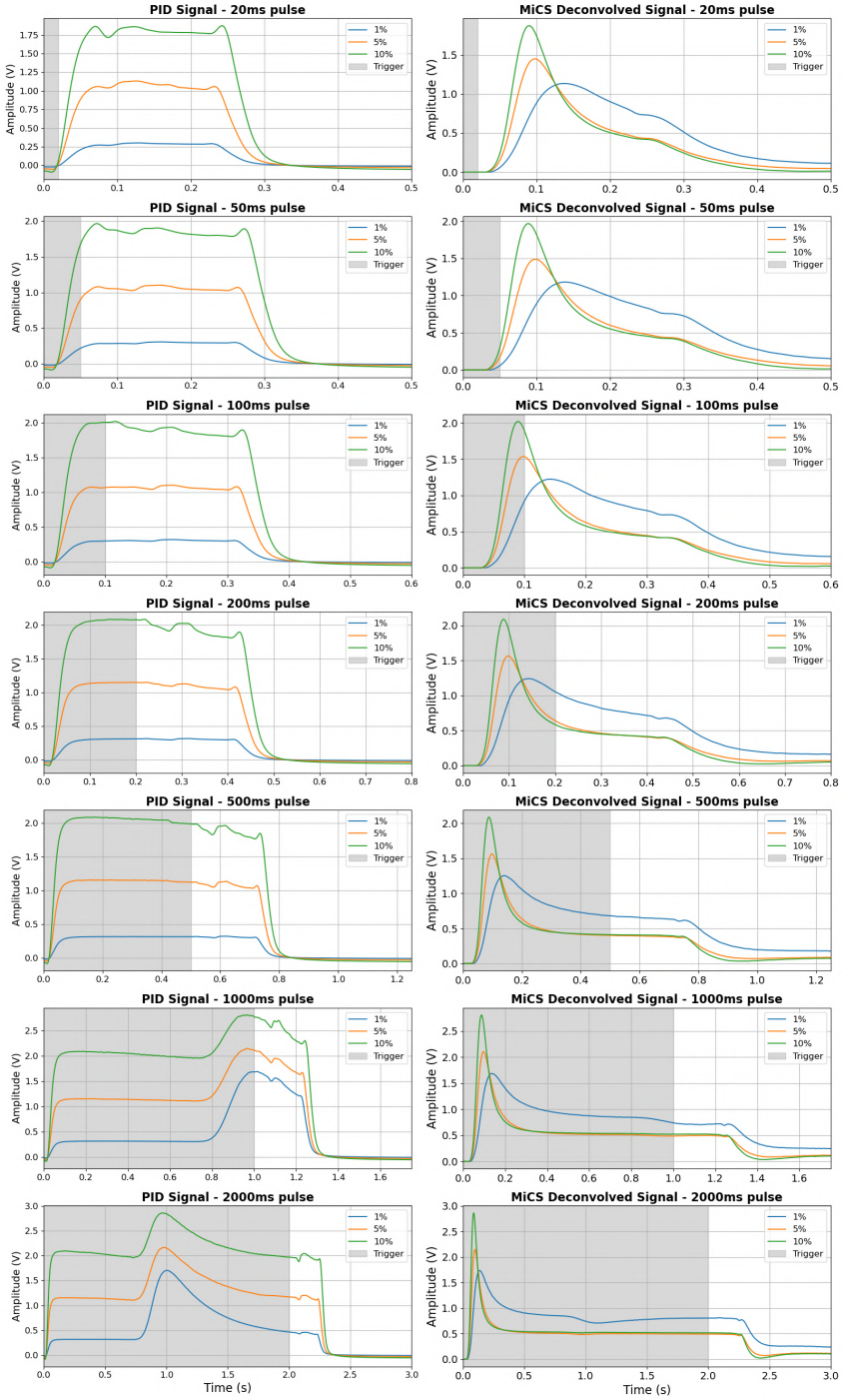

Figure 3.27: Ethyl Butyrate simple pulses of different durations and different concentrations. 10%, 5% & 1% concentrations are represented by green, orange and blue colours respectively for both sensors. The signals shown for different concentrations for both sensors are the mean of 5 repeats. Odour presentation (grey)

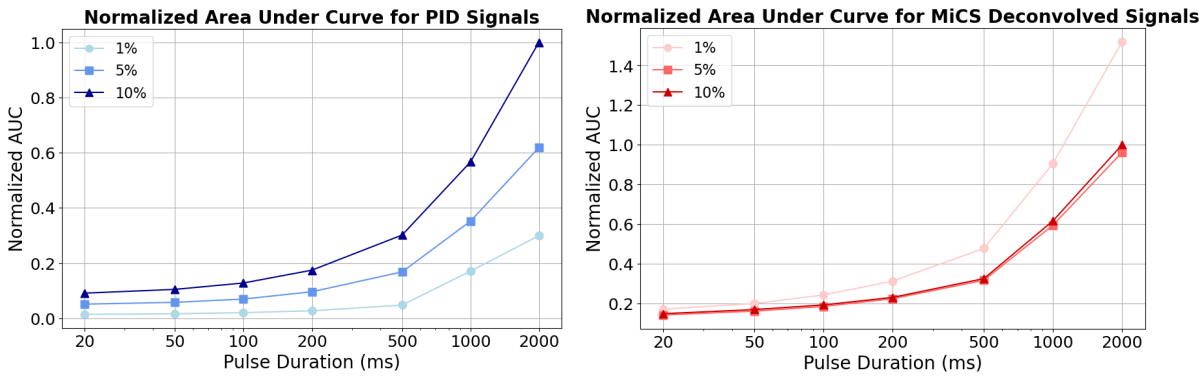

(a) (b)

Figure 3.28: Normalised AUC plots of different concentrations of Ethyl Butyrate simple pulses for (a) PID Signal and (b) MiCS deconvolved Signal. PID (blue) and MiCS deconvolved (red). Colour gradient changes from lighter to darker shades with the increase in concentration for both sensors.

Normalised AUC plots for MiCS deconvolved and PID signals don't demonstrate similar response patterns. For PID, the normalised AUC increases exponentially with increasing pulse duration from 20 to 2000 ms, showing a particularly sharp rise between 500 ms and 2000 ms. The concentration dependence is visible in the case of PID, with higher concentrations (10%) consistently producing higher normalised AUC values compared to lower (5% and low (1%) concentrations across all pulse durations.

For MiCS, the 10% and 5% plots have similar values for the corresponding pulse durations but with a slight difference for the 2000 ms pulse. The normalised AUC values are higher for 1% plot than 10% and 5% ones which could be attributed to the sensor getting saturated or shortcomings in deconvolution.

3.3.3 Acetophenone

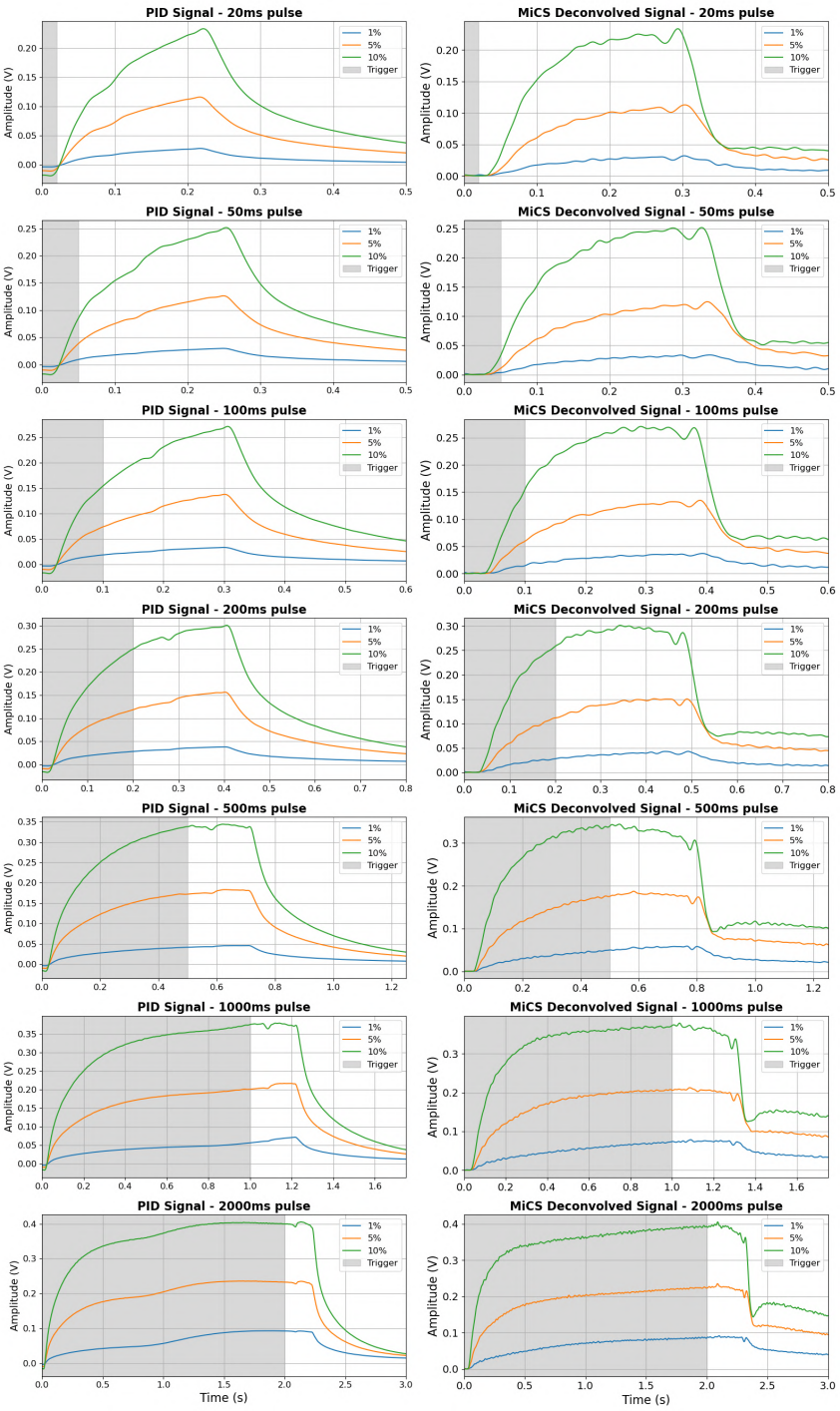

Figure 3.29: Acetophenone simple pulses of different durations and different concentrations. 10%, 5% & 1% concentrations are represented by green, orange and blue colours respectively for both sensors. The signals shown for different concentrations for both sensors are the mean of 5 repeats. Odour presentation (grey)

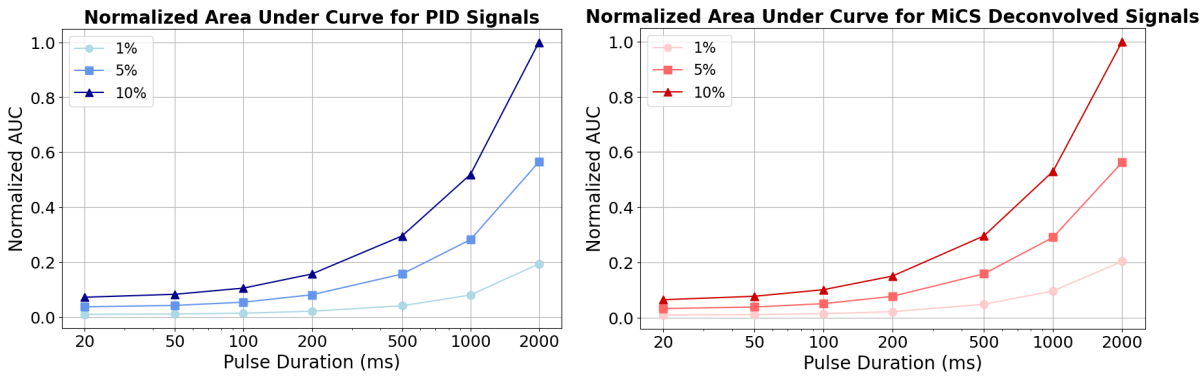

(a) (b)

Figure 3.30: Normalised AUC plots of different concentrations of Acetophenone simple pulses for (a) PID Signal and (b) MiCS deconvolved Signal. PID (blue) and MiCS deconvolved (red). Colour gradient changes from lighter to darker shades with the increase in concentration for both sensors

Normalised AUC plots for both MiCS deconvolved and PID signals demonstrate similar response patterns. For both devices, the normalised AUC increases exponentially with increasing pulse duration from 20 to 2000 ms, showing a particularly sharp rise between 500 ms and 2000 ms.

The concentration dependence is visible for both sensors, with higher concentrations (10%) consistently producing higher normalised AUC values compared to lower (5% and low (1%) concentrations across all pulse durations.This concentration-dependent response is maintained throughout the pulse duration range, confirming the sensors' ability to differentiate between concentration levels. PID signals follow a trend similar to Alpha Terpinene and Ethyl Butyrate but MiCS shows a more pronounced difference between different concentrations compared to Alpha Terpinene.

3.4 Pulse trains - tODD

In this section, we increased the complexity with fast, repetitive short odour pulses. We recorded pulse trains of the frequencies 5 Hz, 10 Hz, 15 Hz, 20 Hz and 40 Hz to study the frequency-dependent performance of the sensors for a standardised pulse duration of 1 second. The odorants used are Alpha Terpinene, Ethyl Butyrate and Acetophenone.

3.4.1 Alpha Terpinene

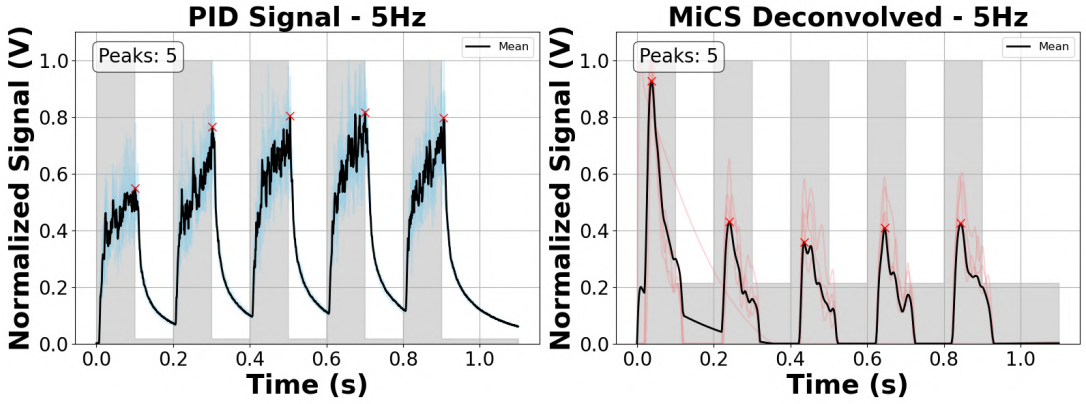

(a)

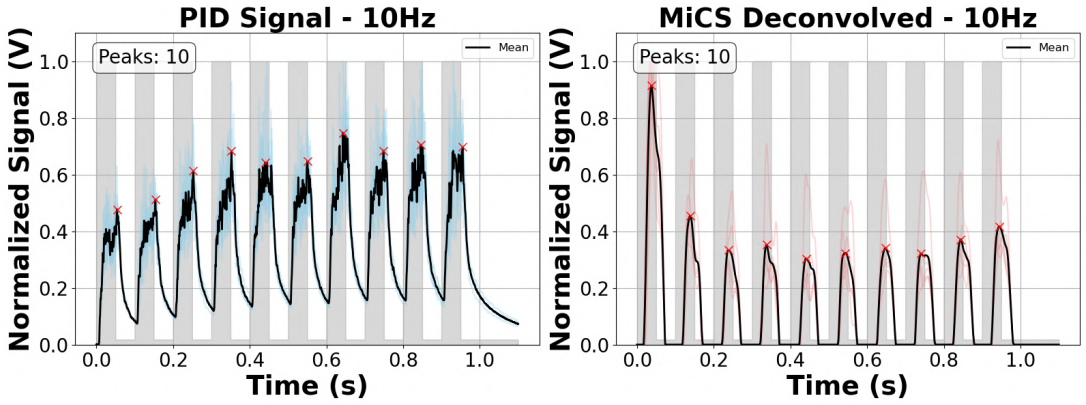

(b)

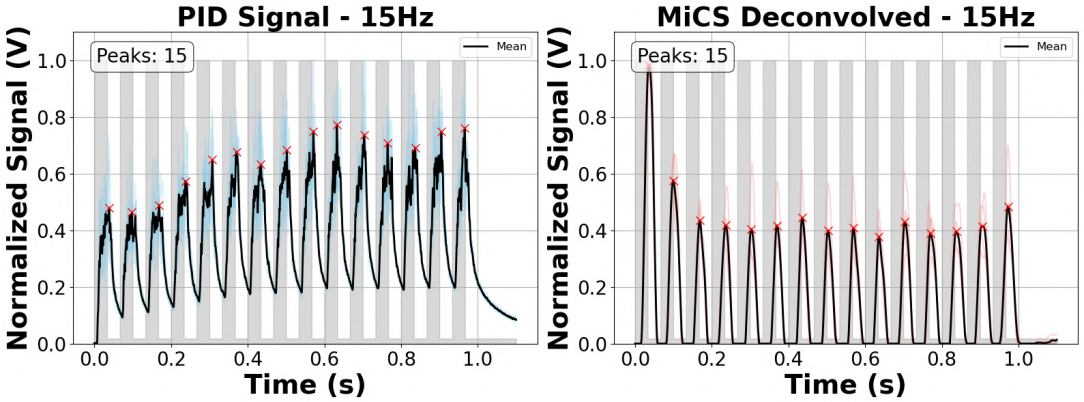

(c)

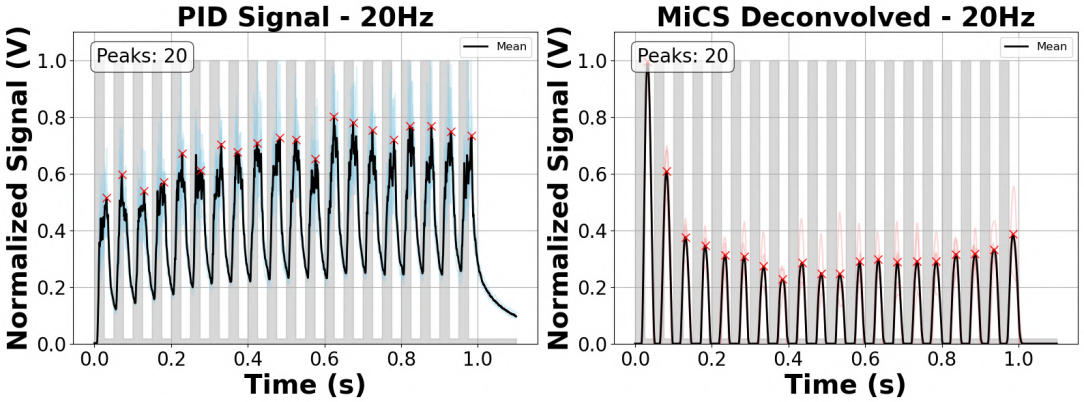

(d)

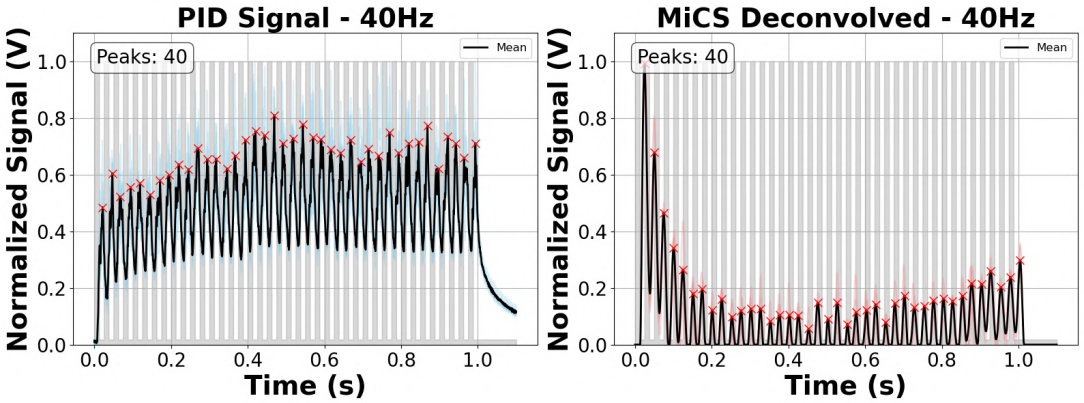

(e)

Figure 3.31: PID and MiCS response to Alpha Terpinene pulse trains of different frequencies (a) 5 Hz, (b) 10 Hz, (c) 15 Hz, (d) 20 Hz, (e) 40 Hz. PID repeats (blue, n=5), MiCS deconvolved repeats (red, n=5), Mean of repeats (black), Peaks detected (red 'x' mark)' and Odour Presentation (grey)

Both PID and MiCS are able to capture the same number of peaks as the odour command pulse provided for all frequencies. The shape of the signal varies for the MiCS deconvolved signal with a decrease in the amplitude after the first peak. The subsequent peaks in the pulse train maintain a low amplitude compared to the first

peak.

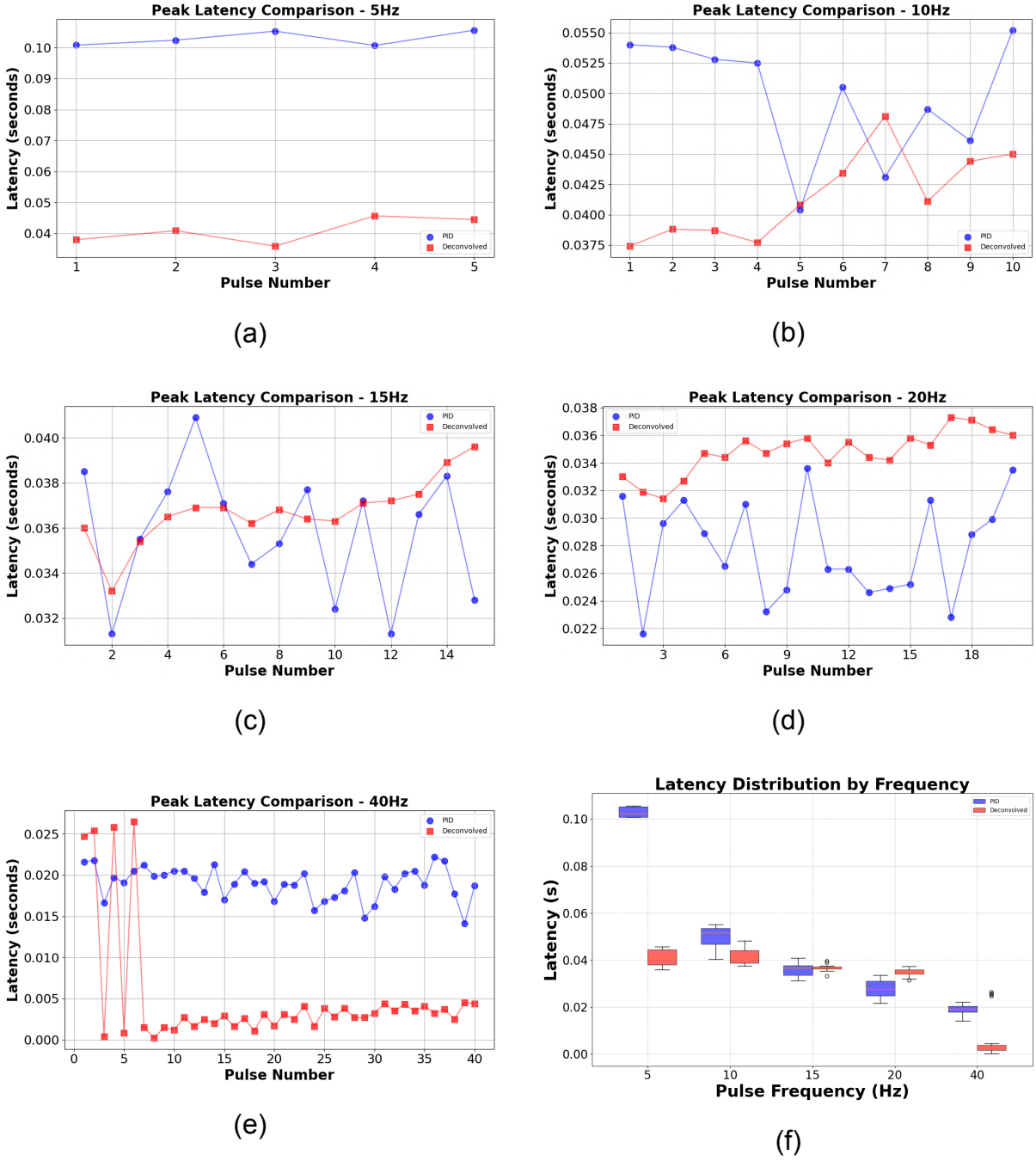

Figure 3.32: Latency for Alpha Terpinene pulse trains of different frequencies. Latency for PID signal (blue), Latency for MiCS deconvolved signal (red)

Latency is calculated as the time difference between the start of each pulse in the pulse train and the corresponding peak detected. This was calculated to study how the signal varies with an increase in pulse numbers for both sensors.

At 5 Hz odour pulse command frequency (Figure 3.32 (a)) the PID signal consistently shows higher latency values with slight variations between pulses. The MiCS deconvolved signal demonstrates lower latency values with minor fluctuations across the five pulses.

The 10 Hz odour pulse command frequency latency plot (Figure 3.32 (b)) shows distinct patterns between the two sensors across pulse numbers. The PID signal exhibits relatively consistent latency for pulses 1-4, then experiences a sharp drop at pulse 5, followed by fluctuations for the remaining pulses. In contrast, the MiCS deconvolved signal maintains lower latency values for pulses 1-4, then shows a gradual increasing trend for pulses 5-10. The two signals intersect at pulse 5, with MiCS deconvolved signal maintaining generally lower latency compared to PID signal for most of the pulse train, except at pulses 5, 8, and 9.

The 15 Hz odour pulse command frequency latency plot (Figure 3.32 (c)) displays significantly more variability in the PID signal. The PID shows several sharp drops in latency at pulses 2, 10, and 12. The MiCS deconvolved signal shows a more stable response, with a gradual upward trend toward the end of the pulse train.

At 20 Hz odour pulse command frequency (Figure 3.32 (d)), the PID shows consistently lower latency than the MiCS. The PID response continues to show substantial variability with multiple peaks, while the MiCS maintains a relatively stable response.

In the 40 Hz odour pulse command frequency latency plot (Figure 3.32 (e)) the PID signal maintains relatively consistent latency with moderate fluctuations. In contrast, the MiCS deconvolved signal shows extreme variability in the early pulses (1-7), then stabilises at very low latency values for the remainder of the pulse train.

The box plot (Figure 3.32 (f)) summarises the latency distributions across all tested frequencies. The PID signal exhibits an uneven pattern, demonstrating higher latency than MiCS deconvolved signal across all frequencies, except at 20 Hz. The PID signal reveals a pronounced trend, with significant variations in latency depending on the frequency. In contrast, the MiCS deconvolved signal displays a more consistent latency, with only minimal differences observed across the various frequencies.

3.4.2 Ethyl Butyrate

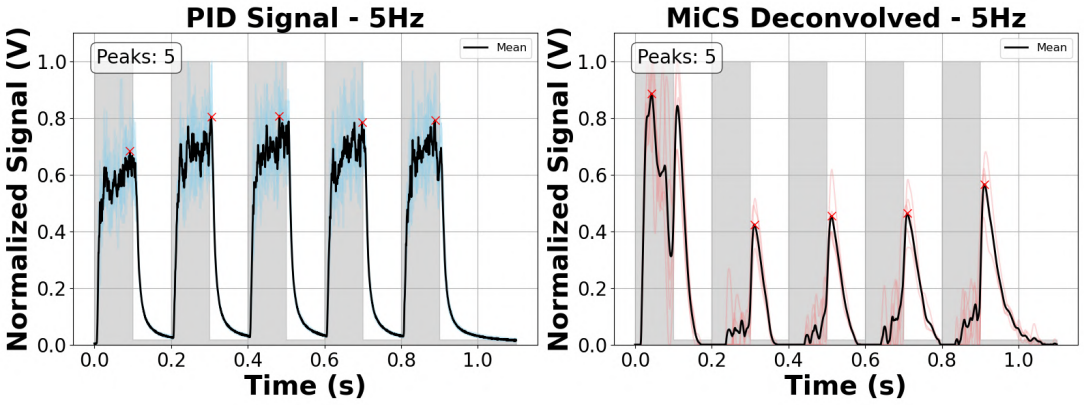

(a)

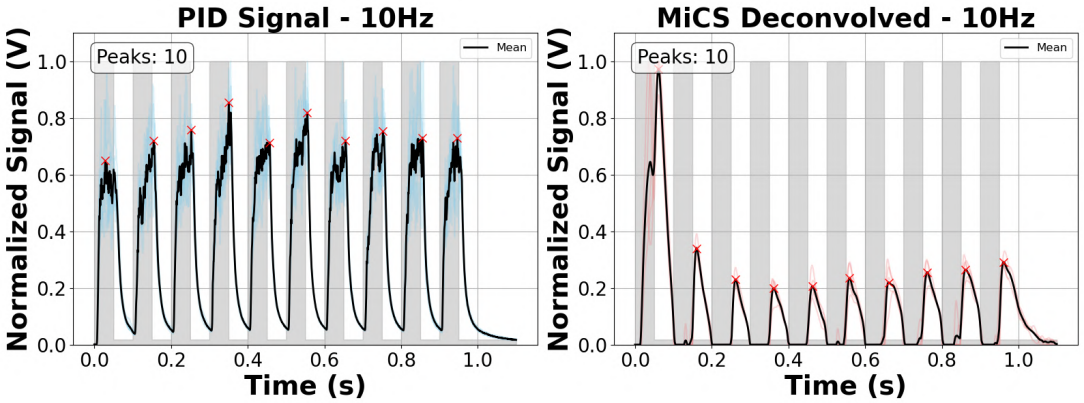

(b)

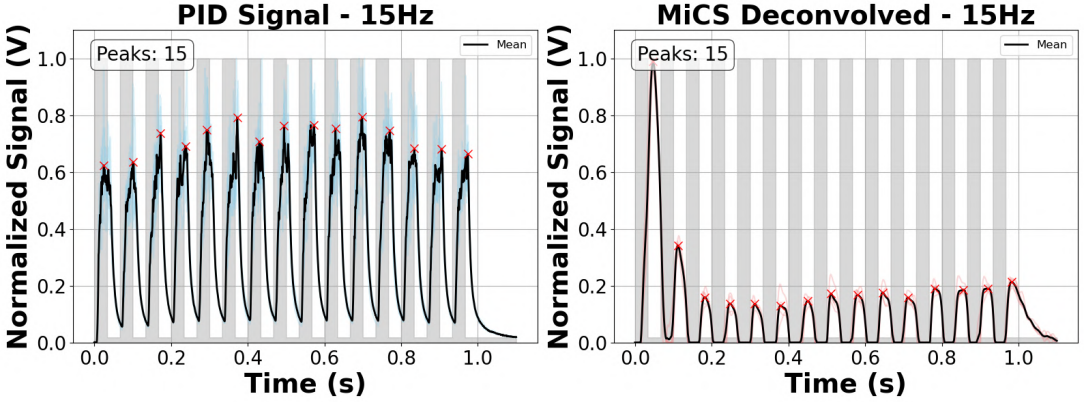

(c)

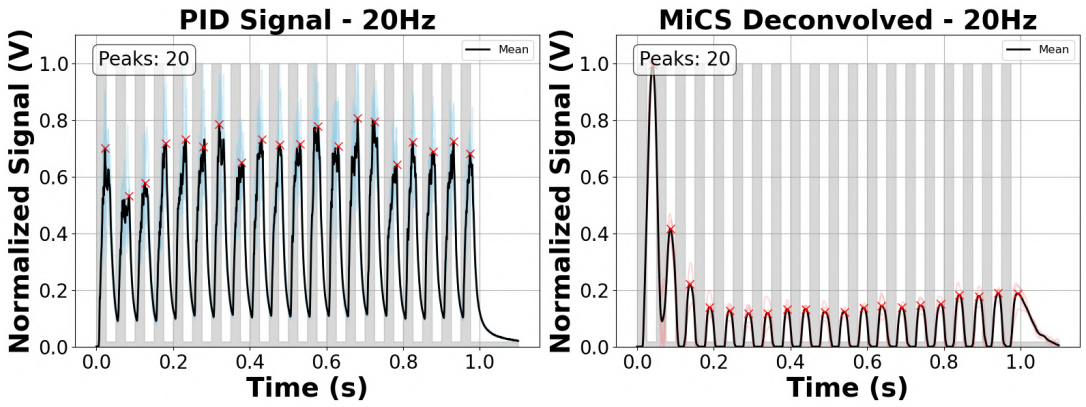

(d)

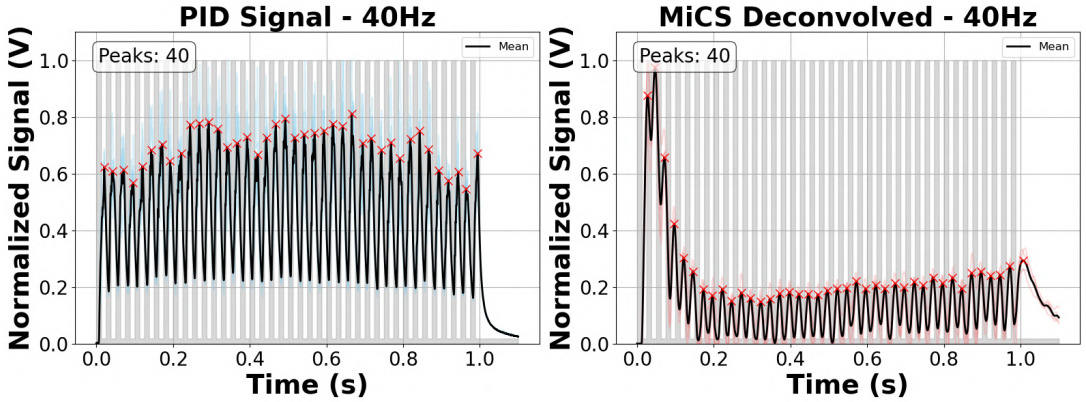

(e)

Figure 3.33: PID and MiCS response to Ethyl Butyrate pulse trains of different frequencies (a) 5 Hz, (b) 10 Hz, (c) 15 Hz, (d) 20 Hz, (e) 40 Hz. PID repeats (blue, n=5), MiCS deconvolved repeats (red, n=5), Mean of repeats (black), Peaks detected (red 'x' mark)' and Odour Presentation (grey)

Both PID and MiCS are able to capture the same number of peaks as the odour command pulse provided for all frequencies. The shape of the signal varies for the MiCS deconvolved signal with a decrease in the amplitude after the first peak. The subsequent peaks in the pulse train maintain a low amplitude compared to the first peak.

At 5 Hz odour pulse command frequency (Figure 3.34 (a)), the MiCS deconvolved signal shows a pattern where it starts at a very low latency for the first pulse, then rises to a higher value by the second pulse and maintains this higher level consistently across pulses 2-5. The MiCS deconvolved signal's latency stabilises at a higher value than the PID signal after the initial pulse.

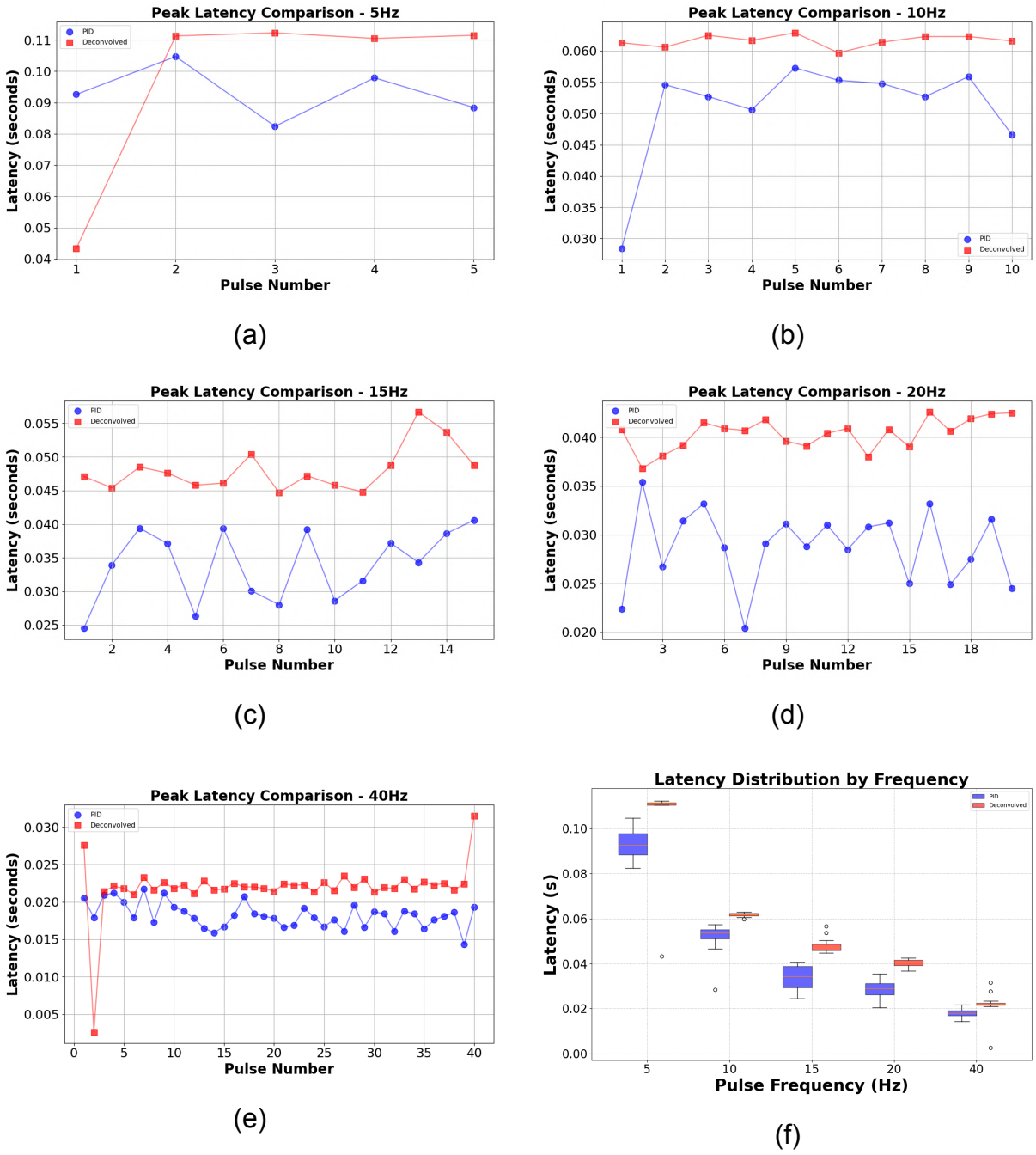

Figure 3.34: Latency for Ethyl Butyrate pulse trains of different frequencies. Latency for PID signal (blue), Latency for MiCS deconvolved signal (red)

At 10 Hz odour pulse command frequency (Figure 3.34 (b)), both sensors display more consistent latency patterns. The MiCS deconvolved shows relatively stable latency across all pulses. The PID signal exhibits lower latency values but with more variability especially for the first and last pulse.

At 15 Hz odour pulse command frequency (Figure 3.34 (c)), both sensors show greater pulse-to-pulse variability.The MiCS deconvolved signal shows higher latency values than PID signal. The PID signal displays a higher variability.

At 20 Hz odour pulse command frequency (Figure 3.34 (d)), the separation between the two sensors remains clear. The MiCS deconvolved signal maintains higher latency values. The PID signal shows lower latency values with significant fluctuations between adjacent pulses, creating a zigzag pattern throughout the pulse train.

The 40 Hz odour pulse command frequency latency comparison (Figure 3.34 (e)) both sensors display their lowest overall latency values in this frequency. The PID signal consistently maintains lower latency than the MiCS deconvolved signal. The MiCS deconvolved sensor exhibits an anomaly with a sudden drop at pulse 2. The PID sensor shows less pronounced variation throughout the pulse train.

The box plot (Figure 3.34 (f)) summarises the latency distributions by frequency for PID and MiCS deconvolved signals. The PID and MiCS deconvolved signals show a consistent decreasing trend as frequency increases. The MiCS deconvolved signal consistently exhibits higher latency than PID across all frequencies.

3.4.3 Acetophenone

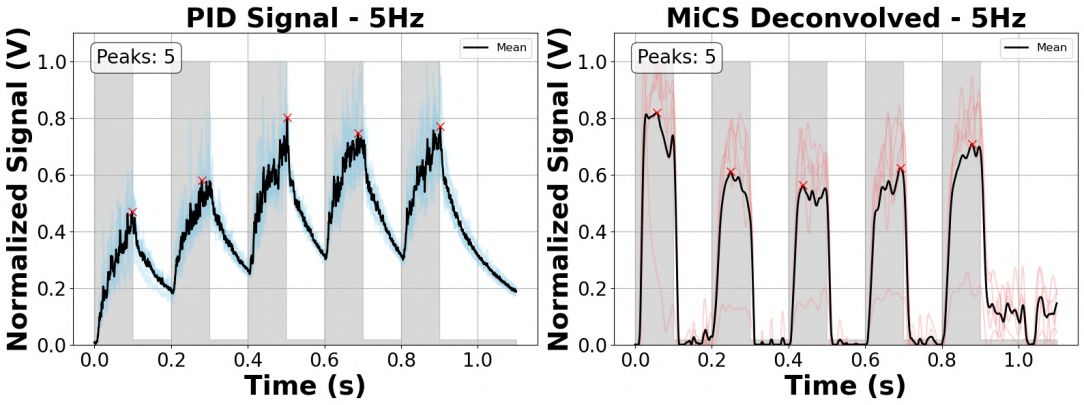

(a)

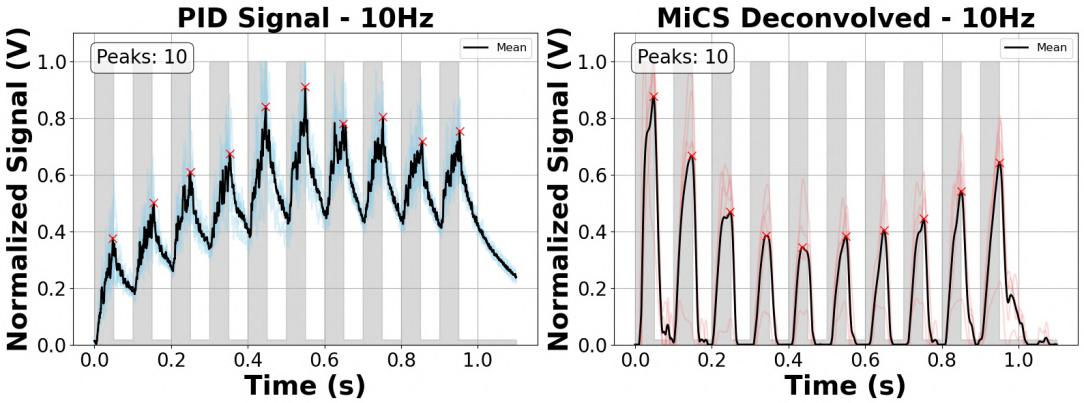

(b)

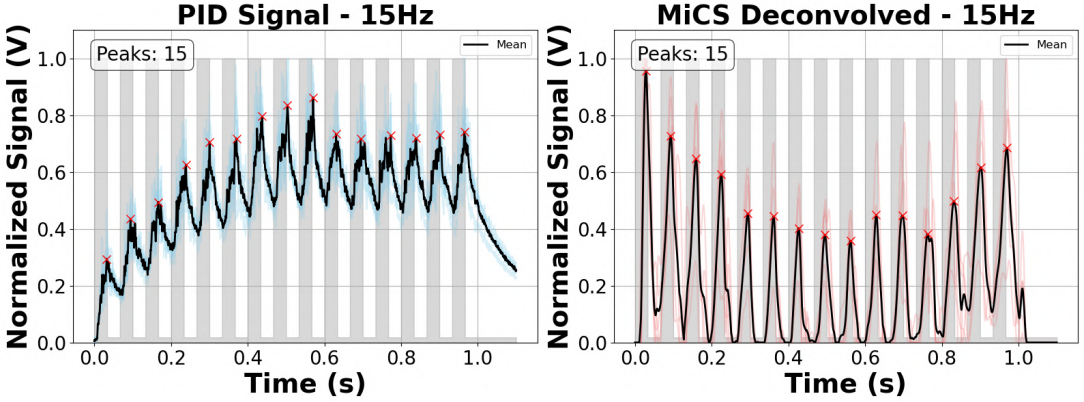

(c)

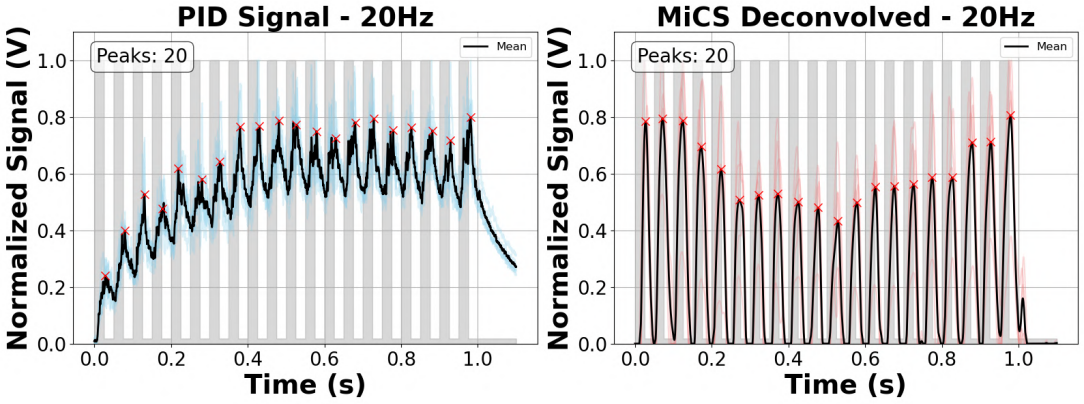

(d)

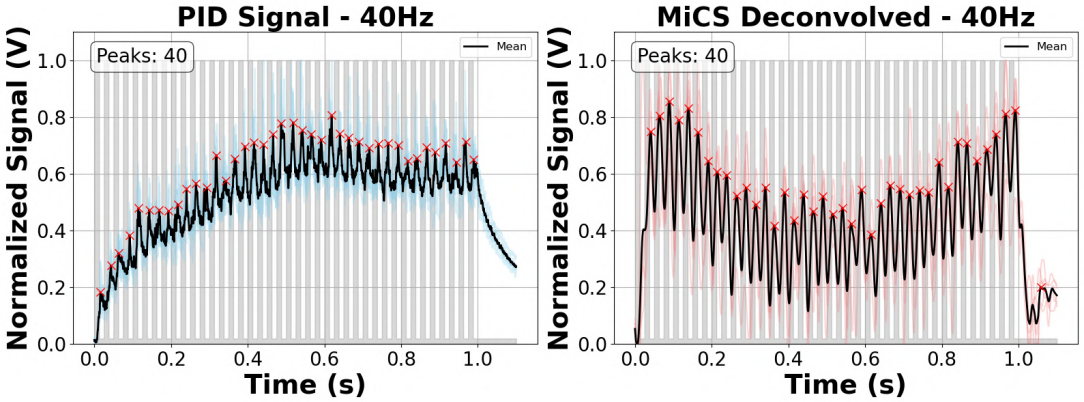

(e)

Figure 3.35: PID and MiCS response to Acetophenone pulse trains of different frequencies (a) 5 Hz, (b) 10 Hz, (c) 15 Hz, (d) 20 Hz, (e) 40 Hz. PID repeats (blue, n=5), MiCS deconvolved repeats (red, n=5), Mean of repeats (black), Peaks detected (red 'x' mark)' and Odour Presentation (grey)

Both PID and MiCS are able to capture the same number of peaks as the odour command pulse provided for all frequencies. Contrary to the trend observed in the case of Alpha Terpinene and Ethyl Butyrate pulse trains,the MiCS deconvolved signal doesn't display a significant decrease in the amplitude after the first pulse. The decrease in amplitude is less pronounced across all pulses for all tested frequencies.

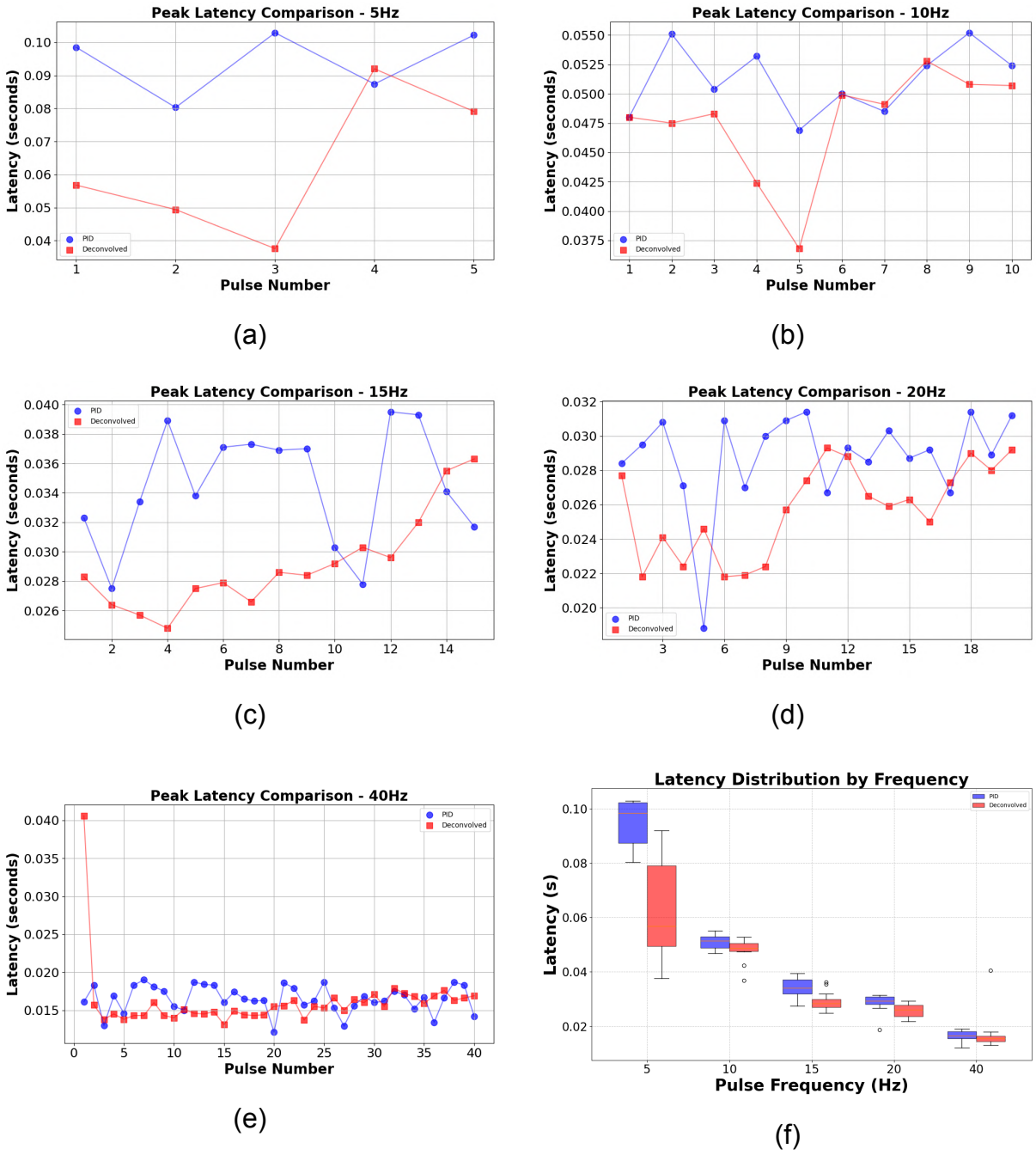

Figure 3.36: Latency for Acetophenone pulse trains of different frequencies. Latency for PID signal (blue), Latency for MiCS deconvolved signal (red)

At 5 Hz odour pulse command frequency (Figure 3.36 (a)) the PID signal shows higher latency values overall, with fluctuations creating a zigzag pattern. The MiCS deconvolved signal shows an interesting trend where it starts with moderate latency, decreases steadily through pulses 2 and 3, then rises at pulse 4, before decreasing again at pulse 5.

At 10 Hz odour pulse command frequency (Figure 3.36 (b)), both sensors show latency values primarily between 0.045-0.055 seconds. The PID signal exhibits greater

variability with peaks at pulses 2 and 9 and a dip at pulse 5. The MiCS deconvolved signal shows relatively stable values for pulses 1-3, then drops sharply at pulses 4-5, before rising to match the PID signal at pulse 6 and remaining comparable through pulse 10.

At 15 Hz odour pulse command frequency (Figure 3.36 (c)), the PID signal exhibits high fluctuations. The MiCS deconvolved signal displays lower latency than the PID throughout pulses 1-13, then crosses over and exceeds PID latency for pulses 14 and 15.

At 20 Hz odour pulse command frequency (Figure 3.36 (d)), the PID signal exhibits significant pulse-to-pulse variation with a distinct zigzag pattern. The MiCS deconvolved signal shows a different pattern, starting at a high latency, dropping to lower values for pulses 2-9, then gradually increasing toward the end.

At 40 Hz odour pulse command frequency (Figure 3.36 (e)) both sensors display similar values throughout most of the pulses , with considerable pulse-to-pulse fluctuations. The MiCS deconvolved signal shows a notably high value at pulse 1 before quickly stabilising. The PID and MiCS deconvolved signals frequently cross each other's lines, indicating similar performance at this frequency, though PID tends to show slightly higher variability between adjacent pulses.

The box plot (Figure 3.36 (f)) summarises the latency distributions across all tested frequencies. The MiCS deconvolved signal shows more variability at 5 Hz but generally lower latency than PID signal across most frequencies. The latency gap between the two sensors changes at around 15 Hz, with MiCS deconvolved signals showing lower latency at higher frequencies.

3.5 Plumes - tODD

Odour plumes prerecorded under turbulent airflow conditions are ideal for studying the sensor's ability to respond to controlled and reproducible rapidly fluctuating odour stimuli. Plume stimuli were classified as sparse or busy based on signal intermittency, FFT maximum, and coefficient of variability. Plume 1, 4, 6 and 7 are responses to sparse plume stimuli, while Plume 2, 3, 5 and 8 are responses to busy plume stimuli. The odorants used are Alpha Terpinene and Ethyl Butyrate.

3.5.1 Alpha Terpinene

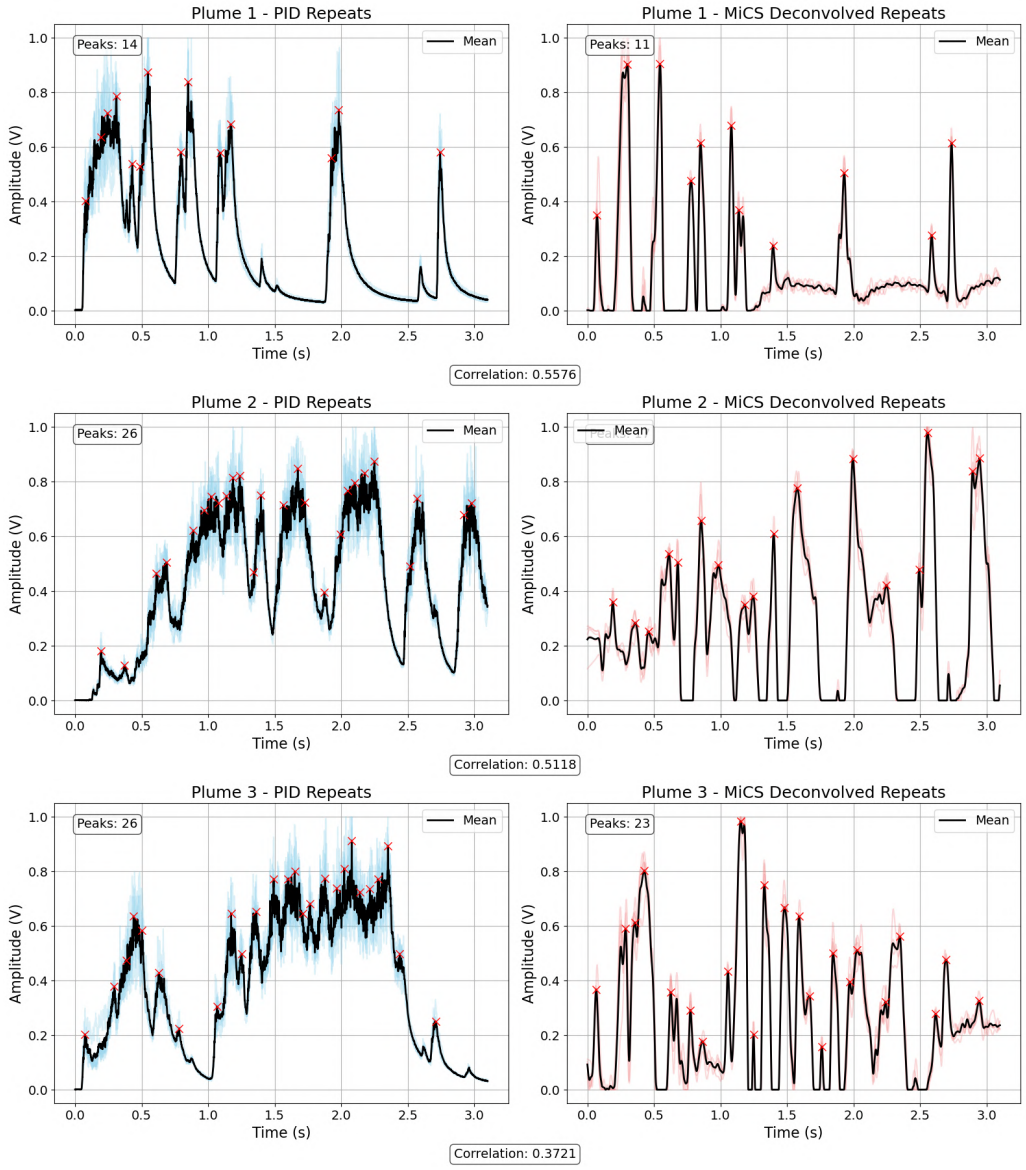

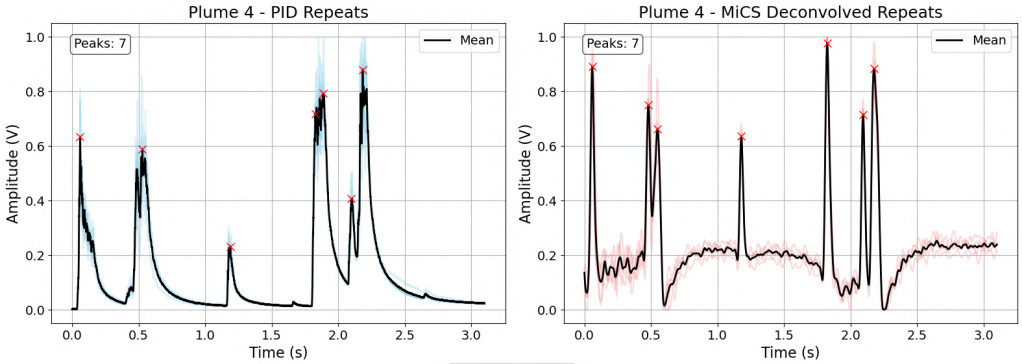

Correlation: 0.4873

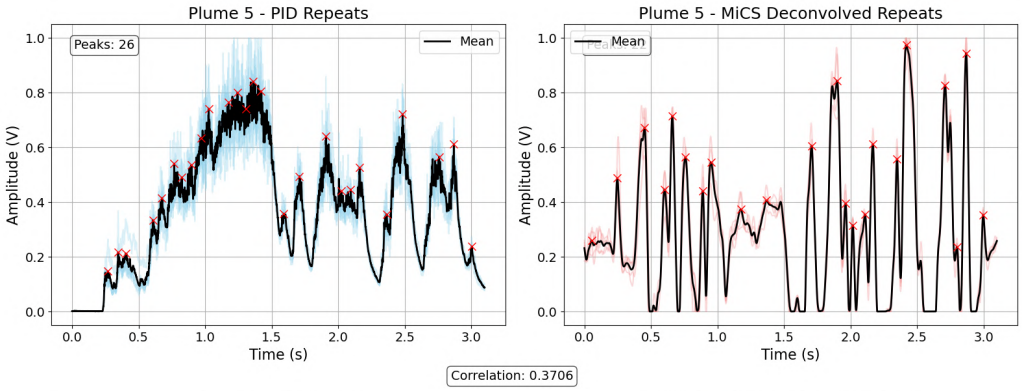

Correlation: 0.3706

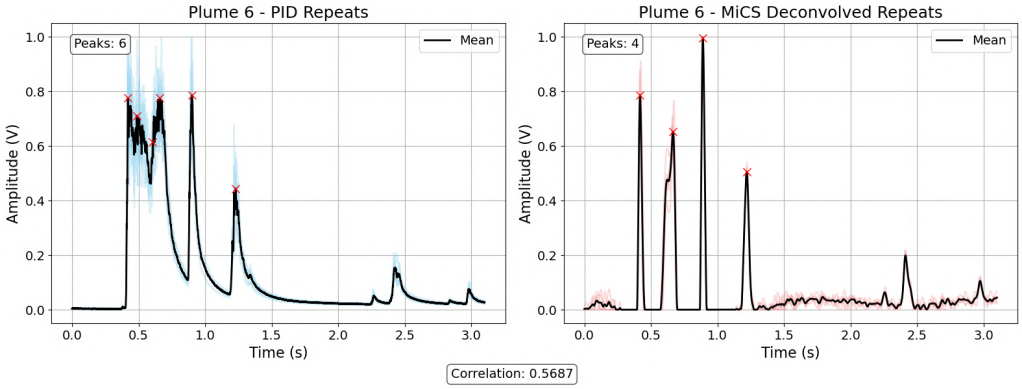

Correlation: 0.5687

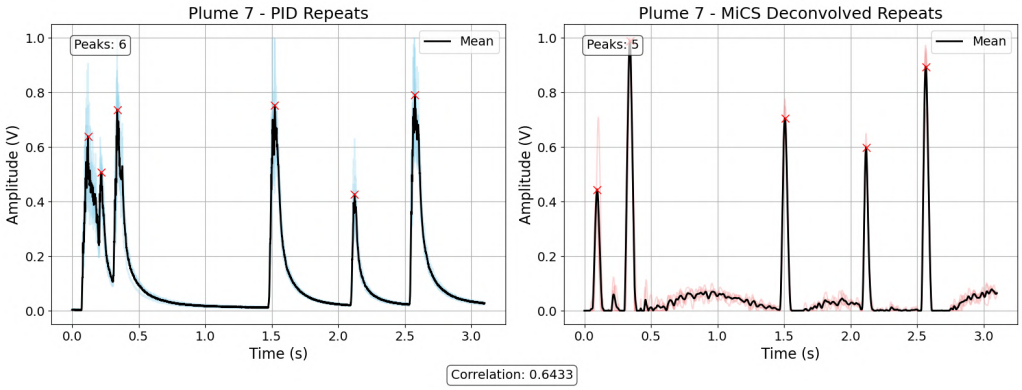

Correlation: 0.6433

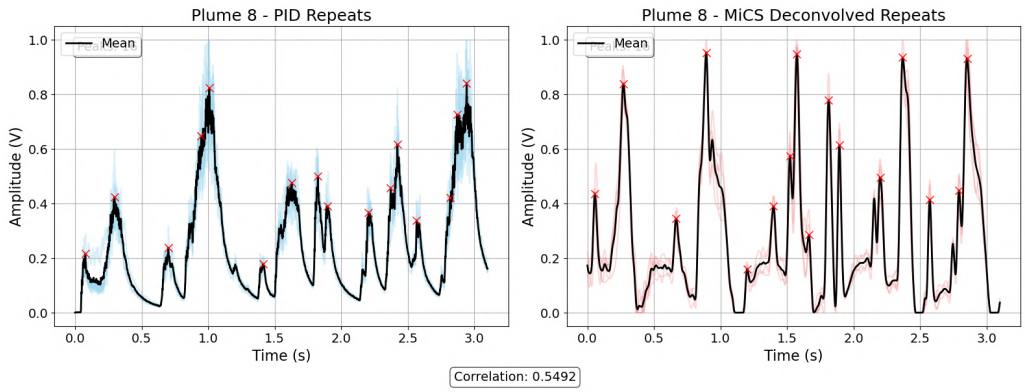

Figure 3.37: Alpha Terpinene: Plume 1 to Plume 8. PID repeats (blue, n=5), MiCS deconvolved repeats (red, n=5), Mean of repeats (black), Peaks detected (red 'x' mark)

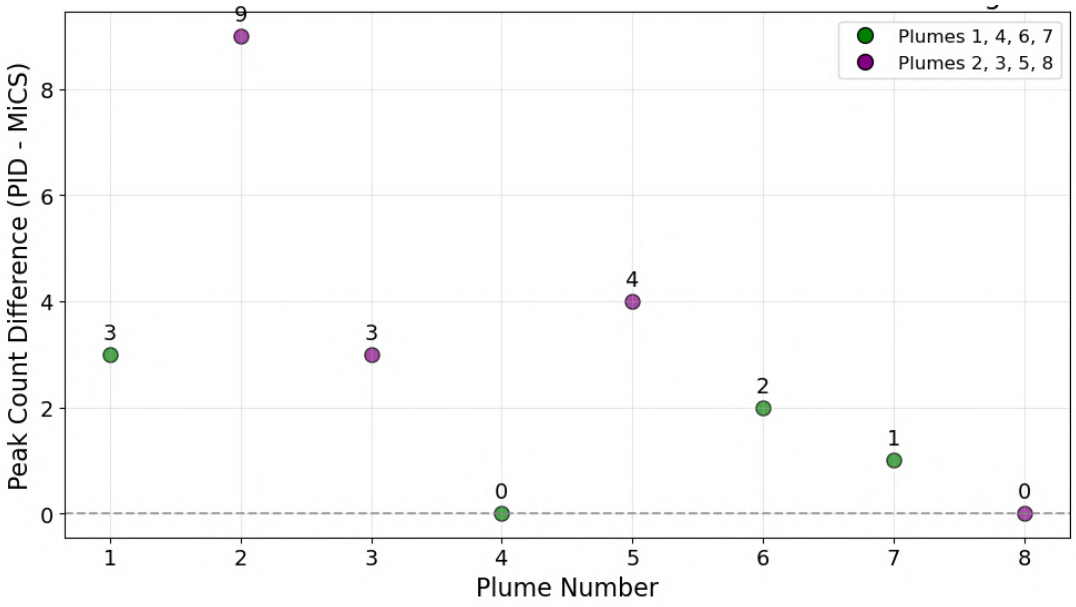

Figure 3.38: Difference in the number of peaks detected between PID and MiCS deconvolved signal for Alpha Terpinene plumes

The difference in the number of peaks detected for PID and MiCS deconvolved signal (Figure 3.38) varies from 0 to 3 for sparse plumes and from 0 to 4 (with an outlier at 9) for busy plumes. The similarity in the number of peaks detected suggests that the MiCS deconvolved signal captures the major peaks or events observed in the PID signal for the corresponding plume.

3.5.2 Ethyl Butyrate

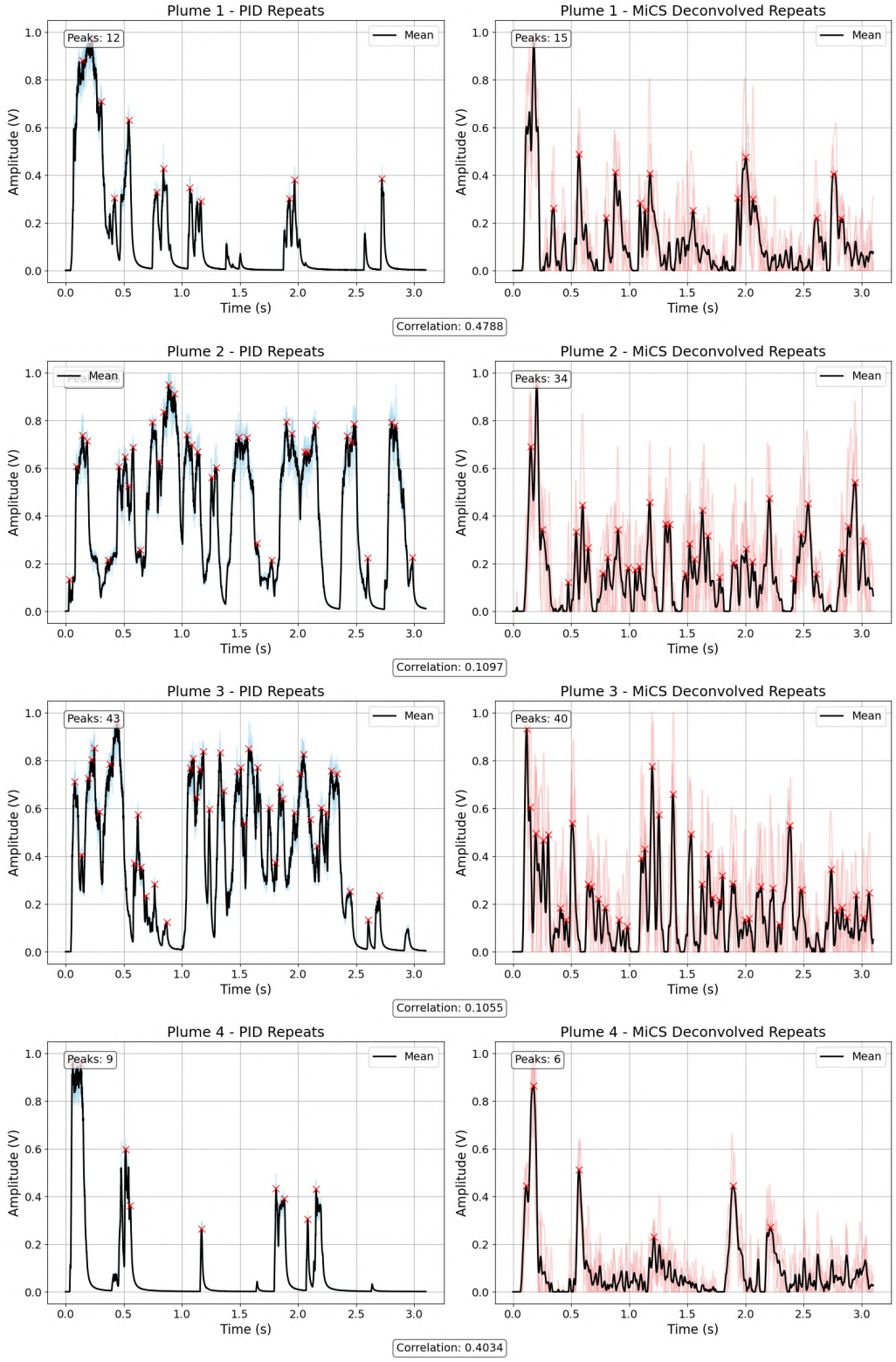

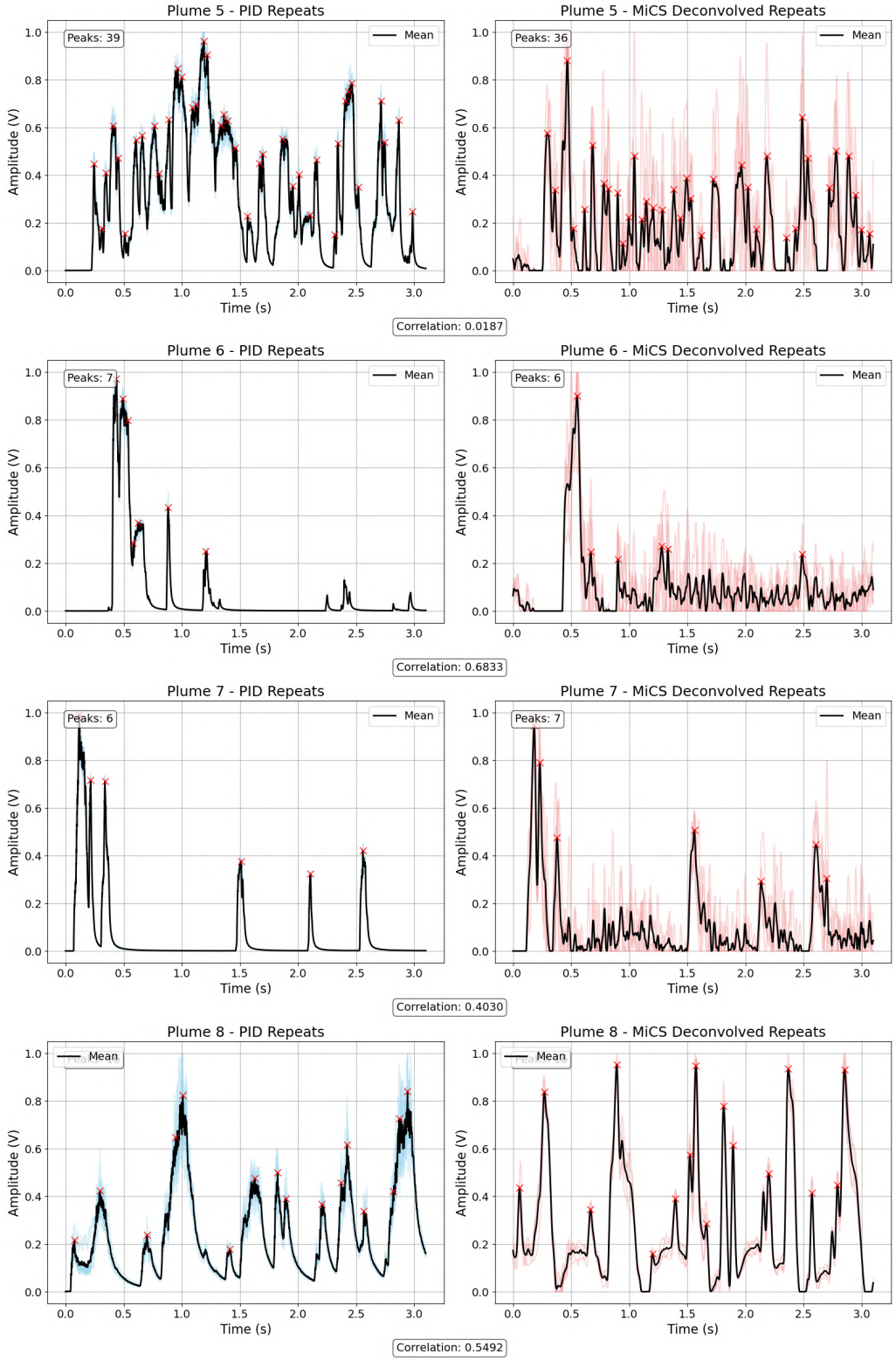

Figure 3.39: Ethyl Butyrate: Plume 1 to Plume 8. PID repeats (blue, n=5), MiCS deconvolved repeats (red, n=5), Mean of repeats (black), Peaks detected (red 'x' mark)

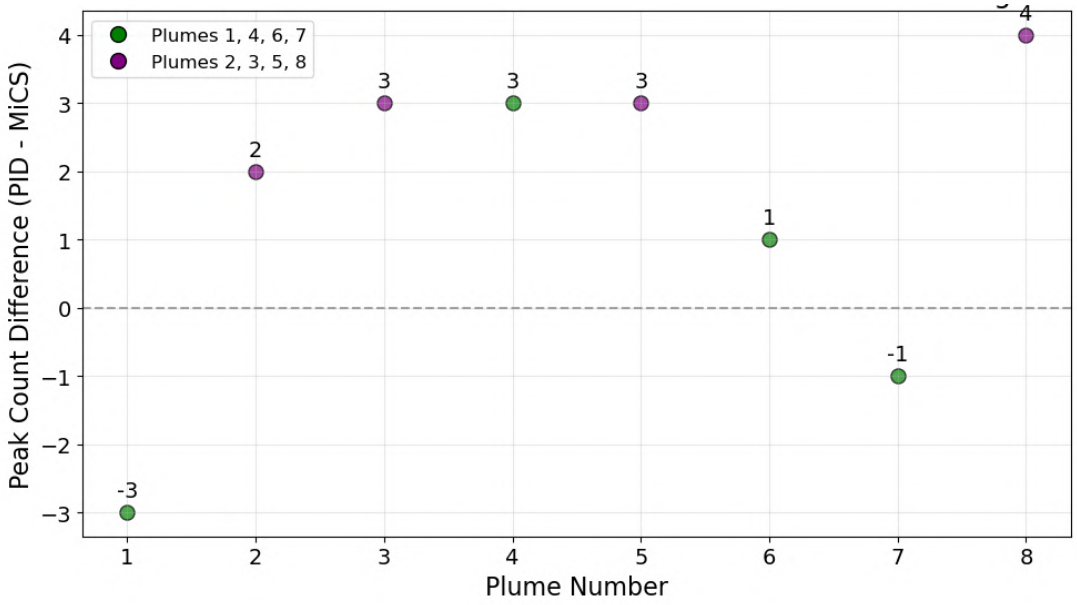

Figure 3.40: Difference in the number of peaks detected between PID and MiCS deconvolved signal for Ethyl Butyrate plumes

The difference in the number of peaks detected for the PID and MiCS deconvolved signal (Figure 3.40) varies from (-3) to 3 for sparse plumes and from 2 to 4 for busy plumes. The similarity in the number of peaks detected suggests that the MiCS deconvolved signal captures the major peaks or events observed in the PID signal for the corresponding plume.

3.6 Plumes - Arena

To test the viability of incorporating the sensor into the behavioural arena we recorded rapidly fluctuating odour stimuli introduced into the behavioural arena with controlled odour delivery under turbulent conditions. We recorded signals simultaneously using PID and MiCS in close proximity (at points marked in Figure 3.41) for different durations of odour presentation under constant airflow conditions maintained by fans and an exhaust. The odorants used are Alpha Terpinene and Ethyl Butyrate.

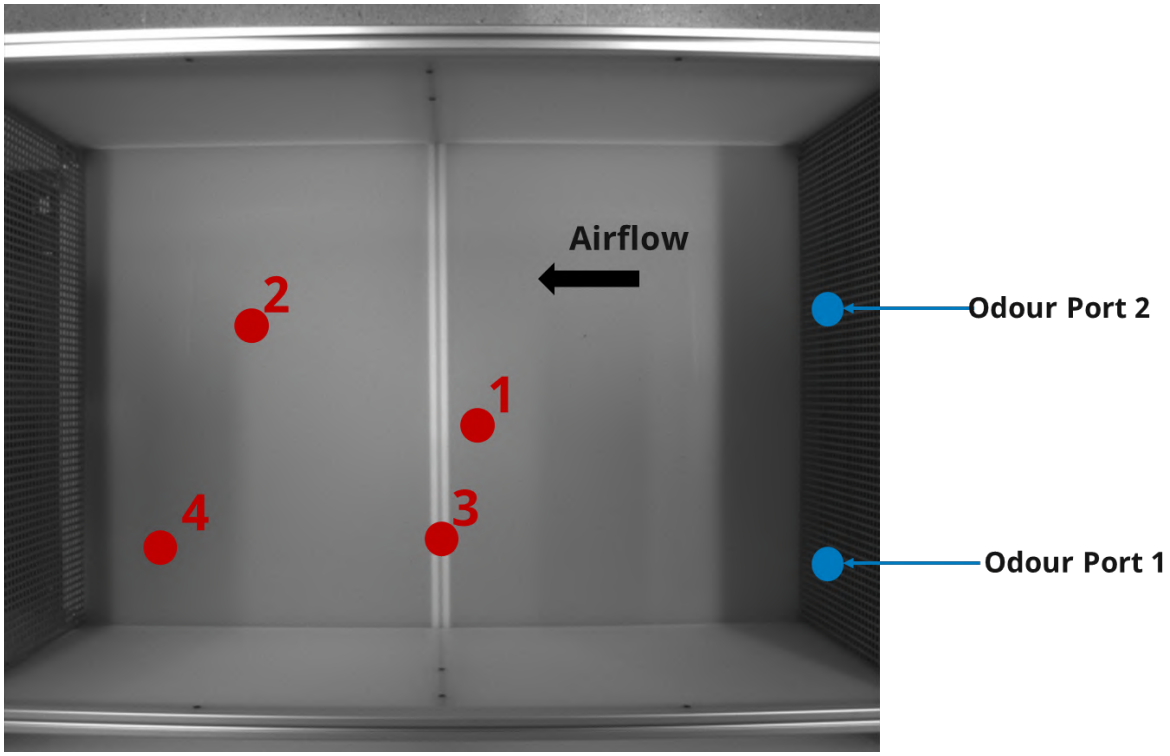

Figure 3.41: Behavioural arena - recording locations

3.6.1 Alpha Terpinene

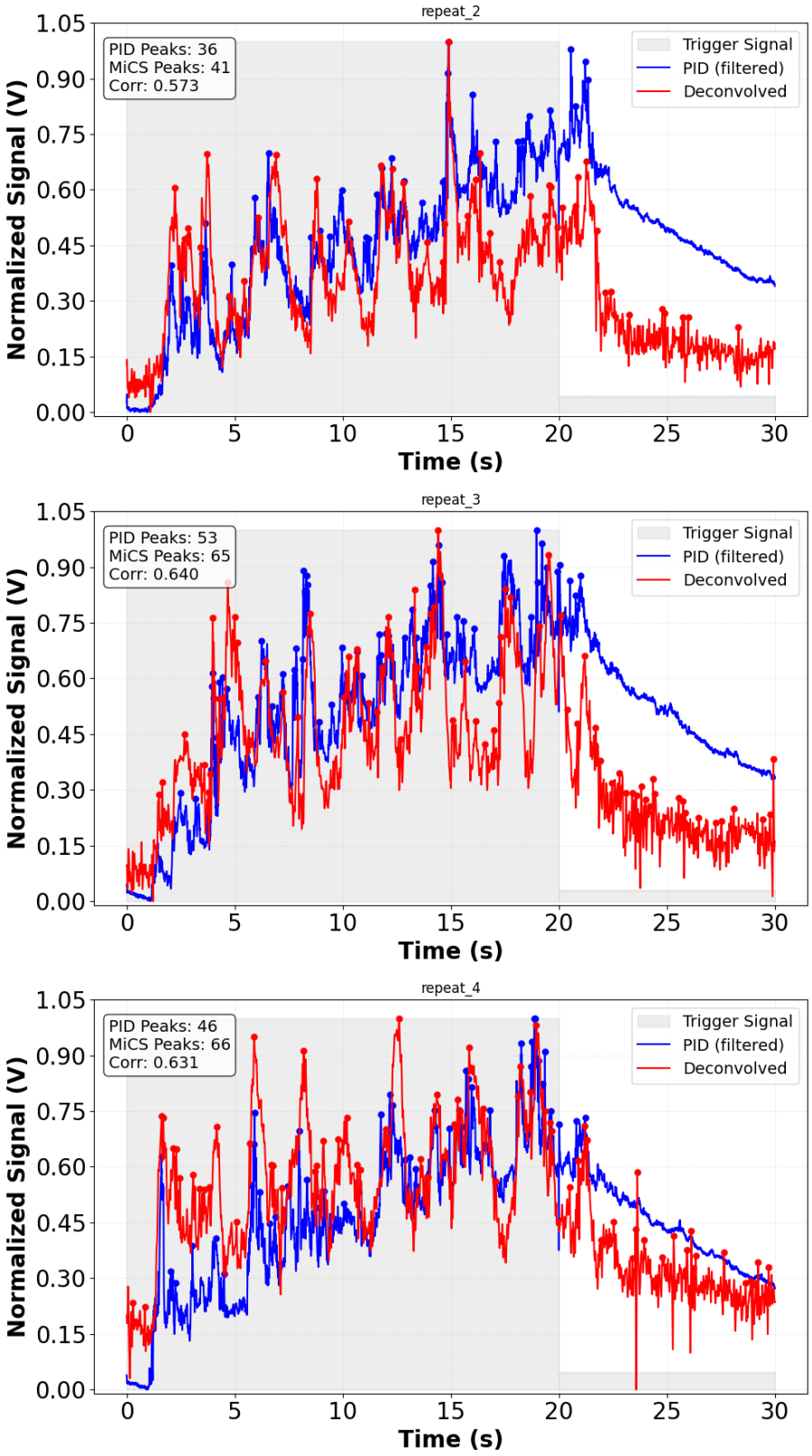

Figure 3.42: PID and MiCS deconvolved signals with Alpha Terpinene at location (1). PID Signal (blue), MiCS deconvolved signal (red) and Odour presentation (grey) lasting for 20 seconds

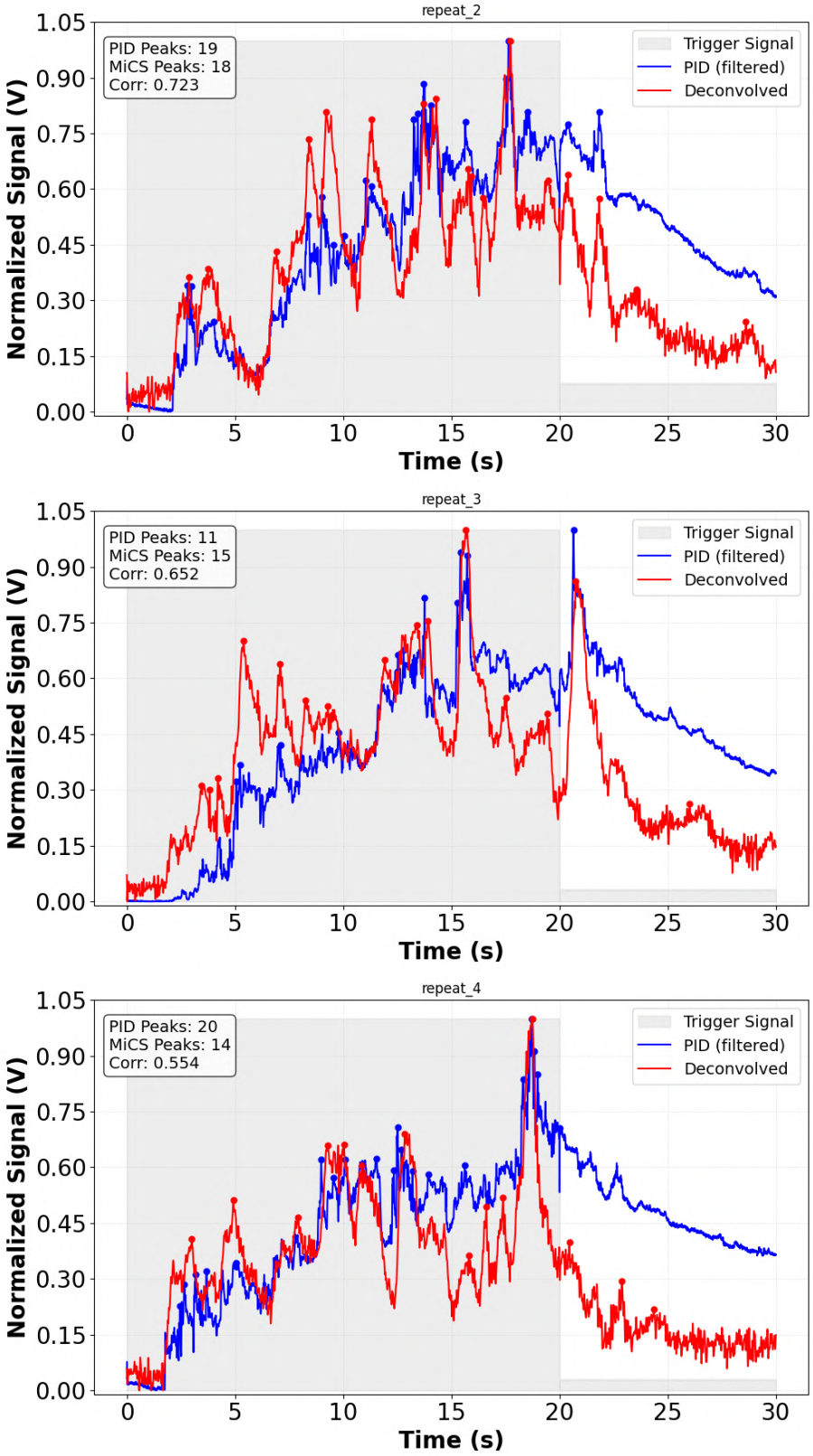

Figure 3.43: PID and MiCS deconvolved signals with Alpha Terpinene at location (2). PID Signal (blue), MiCS deconvolved signal (red) and Odour presentation (grey) lasting for 20 seconds

3.6.2 Ethyl Butyrate

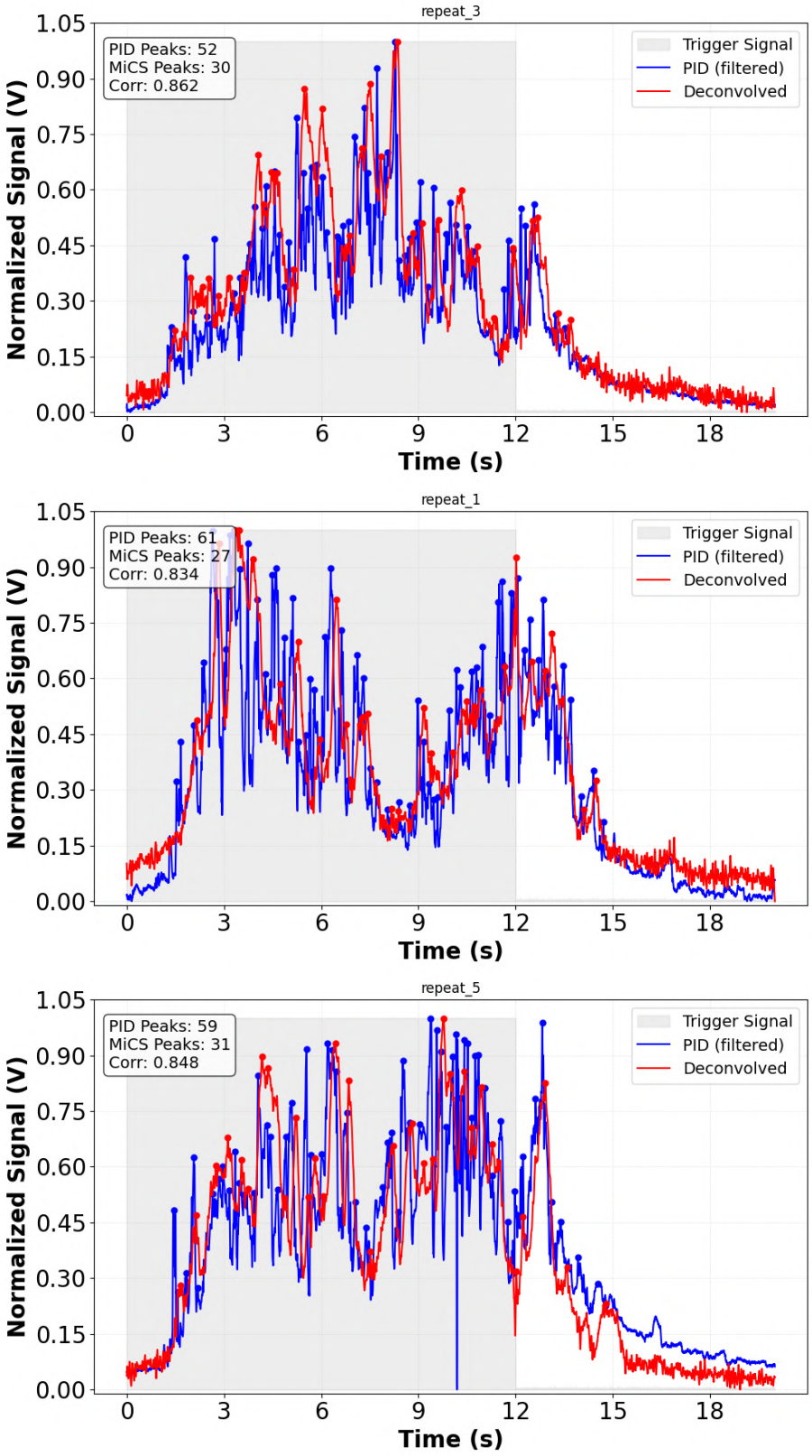

Figure 3.44: PID and MiCS deconvolved signals with Ethyl Butyrate at location (3). PID Signal (blue), MiCS deconvolved signal (red) and Odour presentation (grey) lasting for 12 seconds

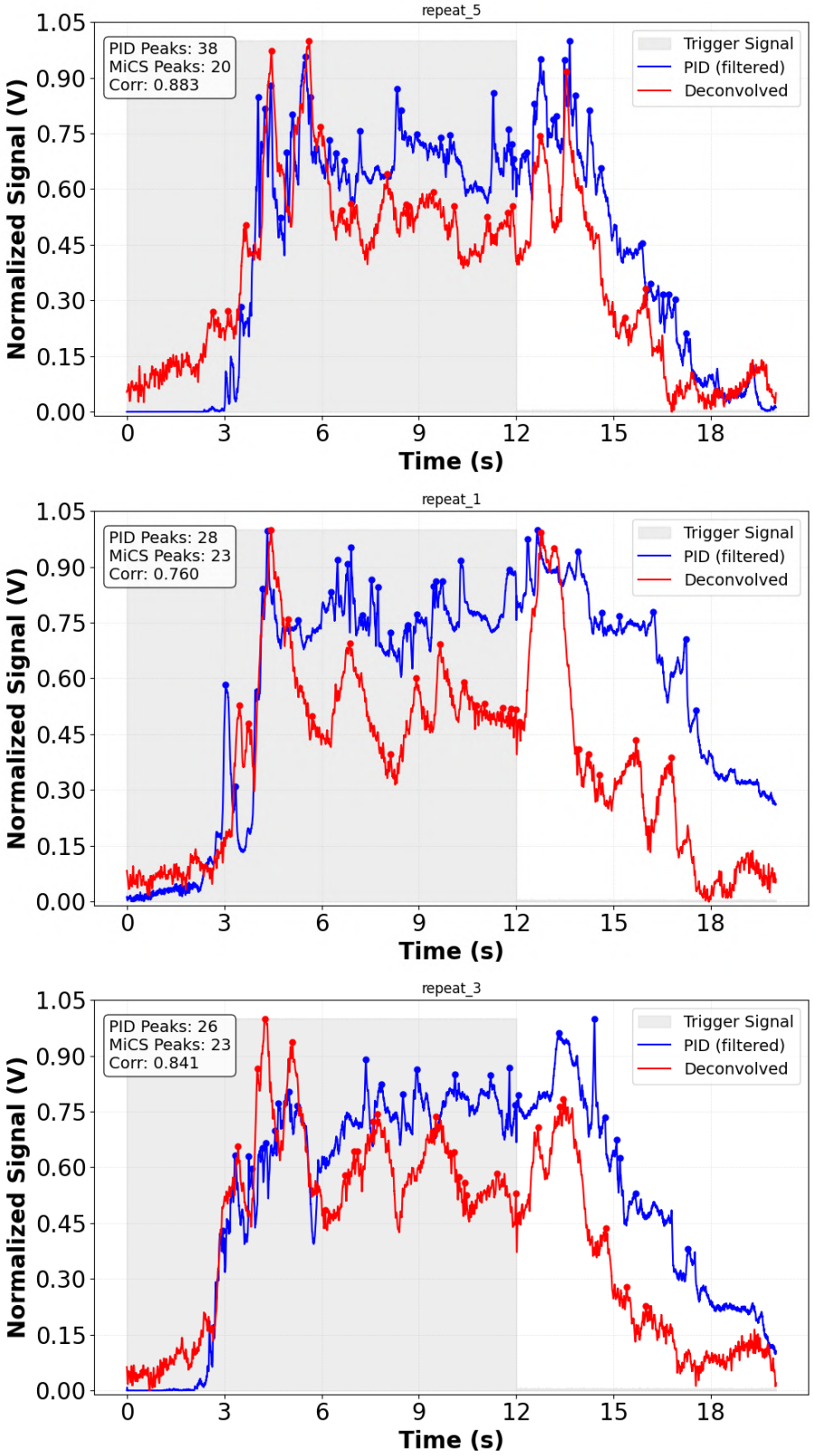

Figure 3.45: PID and MiCS deconvolved signals with Ethyl Butyrate at location (4). PID Signal (blue), MiCS deconvolved signal (red) and Odour presentation (grey) lasting for 12 seconds

The MiCS responses display a correlation higher than 0.8 (with one exception) with the PID responses for Ethyl Butyrate while showing a moderate correlation of 0.5 to 0.7 for Alpha Terpinene. The similarity in the number of peaks detected for the two signals suggests that the sensor is successful in replicating the major temporal patterns observed in the PID response to the same trigger, both at the middle and end of the arena. However, there was notable variability in the number of peaks detected by PID and MiCS at the middle of the arena. In contrast, the number of peaks detected by both sensors was more consistent at the end of the arena.

3.7 Incorporating the Sensor into the Arena

After testing the viability of the sensor for recording real-time olfactory information in the behavioural arena, the next step was to establish the integration of the sensor into the arena. This was achieved with a custom-made sensor holder, miniature cables and a 10-channel slip ring commutator.

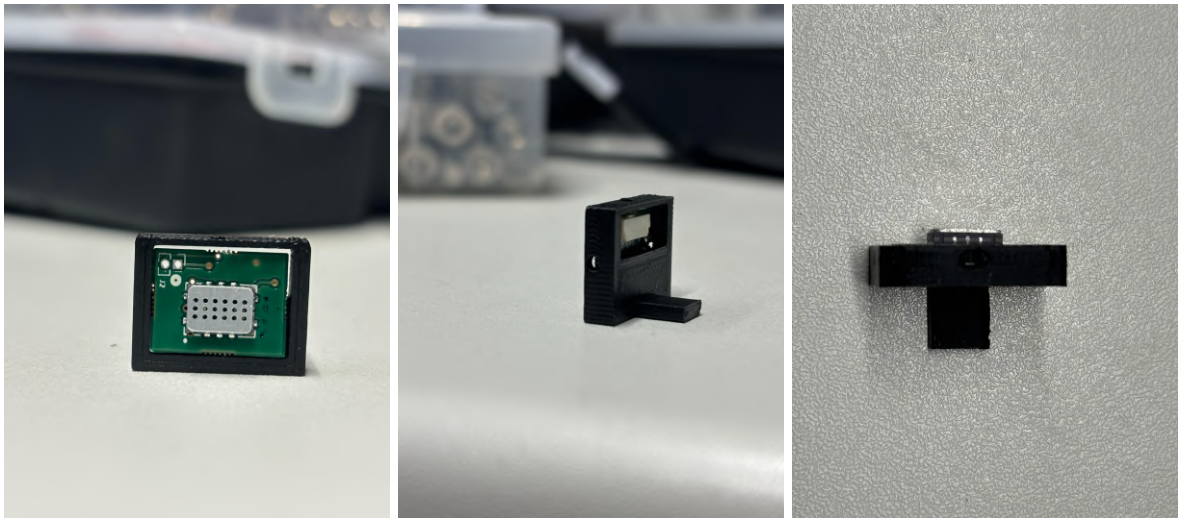

(a) (b) (c)

Figure 3.46: Miniature sensor and the custom-made sensor holder

The sensor holder (Figure 3.46) is necessary to implant and keep the sensor fixed while the animal navigates the arena.

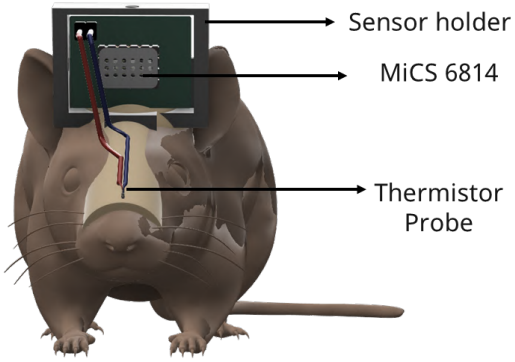

Figure 3.47: Design of a mouse with the sensor, sensor holder and thermistor probe implanted

The thermistor probe to study the respiration of the animal will be implanted over the olfactory epithelium after piercing the nasal bone (Figure 3.47).

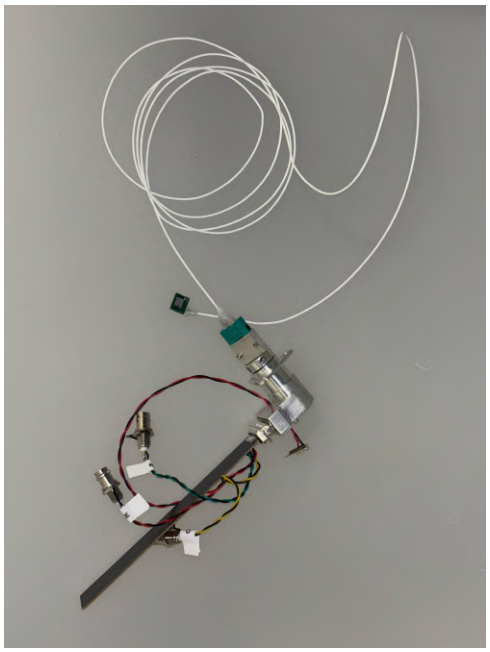

Figure 3.48: Commutator and the miniature cable with the connections established to the PCB

The miniature cable (STC-36T-8 from Micro Measurements) is ideal for integrating the miniature sensor into the behavioural arena while allowing sensor-implanted animals to move freely as it helps to minimise the physical burden and allows the animals to move freely without constraints. The 36 AWG silver-plated copper conductors ensure stable and reliable signal transmission throughout experimental trials.

The SL10C slip-ring commutator (Campden Instruments) maintains a continuous electrical connection between stationary and rotating components, allowing sensor-implanted animals to move without constraint during behavioural experiments. Designed with a 10-channel configuration and a low-noise transmission system, it prevents signal loss while eliminating cable twisting and tangling as the animal explores the arena.

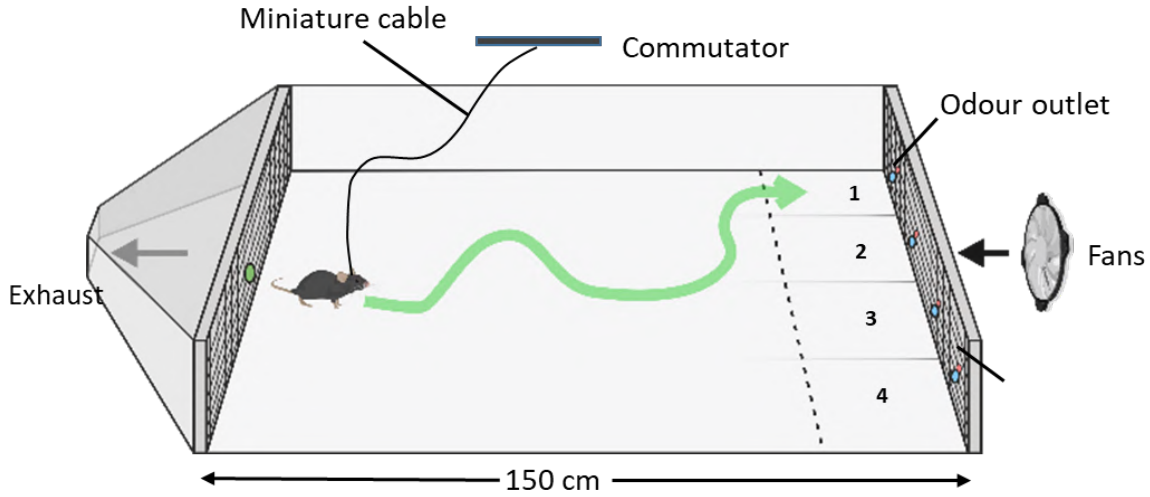

Figure 3.49: Schematic displaying the plan to integrate the sensor

The commutator will be mounted on a profile above the arena, as shown in Figure 3.49 to ensure that the length of the cable released is regulated to avoid entanglement.

Chapter 4

DISCUSSION

The aim of this project was to develop a miniature odour sensor that can be head-mounted on a freely behaving animal, performing an odour navigation task in a controlled behavioural arena (150cm x 108 cm) with turbulent airflow conditions to mimic natural environment, to record real-time olfactory information. The Photoionisation Detector (PID) is widely acknowledged as the gold standard for odour detection. Multiple metrics were employed to systematically compare the performance of the MiCS 6814 sensor against the PID across various odour stimuli involving Alpha Terpinene, Ethyl Butyrate, and Acetophenone. We found that the MiCS generally shows comparable sensitivity and bandwidth to the PID rendering it a viable option to record dynamic odour information in freely moving mice.

For simple square pulses, linear regression analysis revealed a high correlation between the normalised area under the curve (AUC) and full width half maxima (FWHM) of the MiCS deconvolved signal compared to the PID signal across all three tested odorants. Specifically, the correlation values for normalised AUC and FWHM between PID and MiCS deconvolved signals were 0.97 and 0.99 for Alpha Terpinene, 0.97 and 0.99 for Ethyl Butyrate, and 0.97 and 0.97 for Acetophenone, respectively. These strong correlations demonstrate the potential reliability of the MiCS for basic odour pulse detection. The direct correlation values between the two signals were considerably lower, ranging from 0.5 to 0.85 for Alpha Terpinene, 0.4 to 0.55 for Ethyl Butyrate, and 0.5 to 0.85 for Acetophenone . The lower correlation arises from the reduced filtering of the signal which was necessary to preserve the fluctuations observed in the signal. This resulted in increased noise affecting the correlation.

The response characteristics to coupled pulses revealed more complex and odorant-specific patterns. For Alpha Terpinene, we observed a correlation of 0.76 for normalised AUC with 10 ms pulses and a strong correlation of 0.98 for FWHM across all pulse width-ISI (Inter-Stimulus Interval) combinations. These findings suggest that

the MiCS can reliably detect and follow coupled pulses of Alpha Terpinene with performance comparable to that of the PID. In contrast, both Acetophenone and Ethyl Butyrate exhibited moderate to low correlations between PID and MiCS deconvolved signals for the metrics employed. The MiCS exhibited a reduced response to the second pulse of Ethyl Butyrate, which had a notable impact on the normalised AUC and FWHM measurements. This could be attributed to either adaptation of the sensing element or challenges in the signal deconvolution process.

The ability to differentiate between various concentrations of odorants represents a critical performance parameter for the sensor. The analysis revealed that for both sensors, the normalised AUC increased exponentially with increasing pulse duration, following expected sensor response dynamics. The concentration dependence was evident for both sensors in the cases of Alpha Terpinene and Acetophenone as we observed a proportional increase, with higher concentrations (10%) consistently producing elevated normalised AUC values compared to medium (5%) and low (1%) concentrations across all pulse durations. However, a significant limitation emerged with the MiCS's ability to differentiate concentrations of Ethyl Butyrate. While the PID successfully distinguished between different concentrations of this odorant, the MiCS yielded similar response values for 10% and 5% concentrations, while paradoxically showing a higher response for the 1% concentration. This anomaly likely arises from either saturation effects of the sensor or limitations in the deconvolution-based signal processing.

When examining the response to pulse trains at different frequencies (5 Hz, 10 Hz, 15 Hz, 20 Hz and 40 Hz), both the PID and MiCS demonstrated the ability to detect the same number of peaks as provided by the odour command pulse across all three odorants. This result confirms the temporal fidelity of the MiCS for detecting discrete odour events. Additionally, utilising tODD (temporal Odor Delivery Device) allowed us to present pulse trains with a high temporal bandwidth, enabling more precise control of odour presentation. A notable characteristic of the MiCS response was the progressive diminution of signal magnitude following the initial peak for all odours except Acetophenone. This reduction in amplitude for subsequent pulses became particularly pronounced at higher frequencies, suggesting potential limitations in the sensor's recovery time or possible adaptation mechanisms within the sensing element.

The temporal response properties, particularly the latency to the peak of the odour pulse, exhibited distinctive patterns across different odorants. For Alpha Terpinene, the PID signal displayed higher latency and more pronounced frequency dependent variations compared to the MiCS deconvolved signal, which maintained relatively consistent latency at frequencies from 5 to 20 Hz. Conversely, for Ethyl Bu-

tyrate, both sensors exhibited a decreasing latency trend as frequency increased, but the MiCS deconvolved signal consistently showed higher values than the PID signal. Interestingly, for Acetophenone, the MiCS deconvolved signal generally demonstrated lower latency than the PID across most frequencies, although it exhibited greater variability at lower frequencies, particularly at 5 Hz. These odorant-specific latency profiles emphasise the importance of carefully picking odours for behavioural experiments andtailored calibration approaches when precise temporal measurements are required.

In addition, we analysed the sensors' responses to pre-recorded odour plumes generated under turbulent conditions. We were able to present temporally complex odour plumes in a reproducible way using tODD, which is reflected in the low variability across PID repeats and MiCS deconvolved repeats. The MiCS successfully captured the major peaks detected by the PID, with a maximum difference of 4 peaks for Alpha Terpinene (with one exception) and a maximum difference of 3 peaks for Ethyl Butyrate. This level of concordance suggests that the MiCS, despite its limitations, can effectively track the dynamic structure of natural odour plumes with reasonable fidelity.

For plumes recorded directly in the behavioural arena at two distinct locations, the MiCS showed correlation values ranging around 0.8 for Ethyl Butyrate, while correlations for Alpha Terpinene at two other locations ranged between 0.5 and 0.7. The sensor detected a comparable number of peaks as the PID toward the end of the arena for both odours. However, a significant disparity in peak detection was observed in the middle section. This spatial dependency in detection performance could reflect the influence of arena-specific airflow patterns or concentration gradients.

The incorporation of the miniature sensor into the behavioural arena was accomplished through the implementation of a 10-channel slip ring commutator, multi-wire round cable, and a custom-designed sensor holder. This technical infrastructure provides a robust foundation for future experiments enabling the animal to navigate freely across the arena.

Even though the overall performance of the sensor is comparable to PID across stimuli of varying complexities, we revealed some limitations such as the inability to differentiate different concentrations of Ethyl Butyrate and resolving coupled pulses for Ethyl Butyrate and Acetophenone. In future work, the signal processing pipeline could be further improved by employing a dynamic kernel for deconvolution to enhance its viability in complex olfactory environments.

In natural environments, odour plumes consist of complex mixtures of chemical molecules at varying concentrations. The sensor's capacity to discriminate among these mixtures can be investigated by combining the outputs from multiple sensing elements within MiCS: RE, OX and NH3 sensing elements. The data presented so far is from RE sensing element. This capability can be systematically explored in the next phase of the project using tODD, allowing for controlled and reproducible presentation before extending the investigation to turbulent conditions within the arena.

To enable direct correlation between the respiration dynamics of a mouse and the structure of an odour plume as recorded by the miniature odour sensor, breathing rate, amplitude, and phase information are first extracted from the thermistor signal, while the odour sensor signals are processed to identify concentration fluctuations. Both datasets are temporally aligned using a common timestamp, allowing for precise synchronisation of breathing phases with local odour concentration fluctuations. Correlation metrics can then be applied to quantitatively assess the relationship between respiratory behavior and odour plume dynamics. To ensure calibration and validation of the methodology, controlled odour presentations with known plume structures to provide a reference for accurate dataset alignment and interpretation.Importantly, the temporal characteristics of the respiration signals recorded with the thermistor-including potential delays will be evaluated in a head-fixed animal, providing a reliable basis for subsequent analyses in freely moving animals. This integrated strategy facilitates a robust analysis of the interplay between mouse respiration and the spatiotemporal features of odour plumes.

Data from a sensor implanted, freely-moving mouse couldn't be presented because of the delay in the approval of the animal license by the local authority to implant the sensor and perform animal experiments.

Chapter 5

CONCLUSIONS

In this project, we developed a miniature, head-mounted odour sensor capable of recording real-time olfactory information in freely behaving animals. By overcoming the inherent limitations of MOx sensors through signal processing involving deconvolution with a rise-decay-sustain kernel, we have established a device that balances the practical requirements of miniaturisation and the necessity for accurate and temporally precise measurement of olfactory information in real time. Through systematic comparison with the gold standard Photo-Ionisation Detector (PID), we have established that the MiCS 6814 sensor, when coupled with appropriate deconvolution techniques, offers a viable alternative for capturing dynamic olfactory information during navigation tasks.

The sensor demonstrated strong performance with simple square pulses across all tested odorants (Alpha Terpinene, Ethyl Butyrate, and Acetophenone), with correlation values above 0.95 for normalized AUC and FWHM. More complex stimuli, such as coupled pulses and pulse trains, revealed odorant-specific response patterns, with particularly strong performance for Alpha Terpinene. While certain limitations were observed, particularly in concentration differentiation for Ethyl Butyrate and amplitude reduction in pulse train responses, the overall temporal fidelity of the sensor remained robust. Crucially, when tested with odour plumes under turbulent conditions, the MiCS sensor successfully captured the major peaks detected by the PID as well as a moderate to high correlation with the signals, demonstrating its ability to track the dynamic structure of highly fluctuating odour stimuli.

The successful integration of this sensor into our custom-designed open-field behavioural arena enables its use as a chronic lightweight implant for freely moving mice. This allows for its use for studying how rodents respond to olfactory stimuli during navigation tasks, allowing us to better correlate the behaviours observed with the specific odour cues the animal encounters.

Chapter 6

REFERENCES

1. Abraham, N. M., Spors, H., Carleton, A., Margrie, T. W., Kuner, T., & Schaefer, A. T. (2004). Maintaining accuracy at the expense of speed: stimulus similarity defines odor discrimination time in mice. neuron, 44(5), 865-876.

2. Ackels, T., Erskine, A., Dasgupta, D., Marin, A. C., Warner, T. P., Tootoonian, S., Fukunaga, I., Harris, J.J. & Schaefer, A. T. (2021). Fast odour dynamics are encoded in the olfactory system and guide behaviour. Nature, 593(7860), 558-563.

3. Baker, K. L., Dickinson, M., Findley, T. M., Gire, D. H., Louis, M., Suver, M. P., Verhagen, J.V., Nagel, K.I. & Smear, M. C. (2018). Algorithms for olfactory search across species. Journal of Neuroscience, 38(44), 9383-9389.

4. Celani, A., Villermaux, E., & Vergassola, M. (2014). Odor landscapes in turbulent environments. Physical Review X, 4(4), 041015.

5. Dennler, N., Drix, D., Warner, T. P., Rastogi, S., Casa, C. D., Ackels,T., Schaefer, A.T., van Schaik, A. & Schmuker, M. (2024). High-speed odor sensing using miniaturized electronic nose. Science Advances, 10(45), eadp1764.

6. Drix, D., & Schmuker, M. (2021). Resolving fast gas transients with metal oxide sensors. ACS sensors, 6(3), 688-692.

7. Findley, T. M., Wyrick, D. G., Cramer, J. L., Brown, M. A., Holcomb, B., Attey, R., ... & Smear, M. C. (2021). Sniff-synchronized, gradient-guided olfactory search by freely moving mice. Elife, 10, e58523.

8. Grimaud, J., Dorrell, W., Jayakumar, S., Pehlevan, C., & Murthy, V. (2024). Bilateral alignment of receptive fields in the olfactory cortex. Eneuro, 11(11).

9. Gumaste, A., Baker, K. L., Izydorczak, M., True, A. C., Vasan, G., Crimaldi, J. P., & Verhagen, J. (2024). Behavioral discrimination and olfactory bulb encoding of odor plume intermittency. Elife, 13,e85303.

10. Jacobs, L. F. (2012). From chemotaxis to the cognitive map: the function of olfaction. Proceedings of the National Academy of Sciences, 109(supplement_1), 10693-10700.

11. Lewis, S. M., Suarez, L. M., Rigolli, N., Franks, K. M., Steinmetz, N. A., & Gire, D. H. (2024). The spiking output of the mouse olfactory bulb encodes large-scale temporal features of natural odor environments. BioRxiv.

12. Marin, A. C., Schaefer, A. T., & Ackels, T. (2021). Spatial information from the odour environment in mammalian olfaction. Cell and Tissue Research, 383, 473-483.

13. Matheson, A. M., Lanz, A. J., Medina, A. M., Licata, A. M., Currier, T. A., Syed, M. H., & Nagel, K. I. (2022). A neural circuit for wind-guided olfactory navigation. Nature communications, 13(1), 4613.

14. Monroy, J. G., González-Jiménez, J., & Blanco, J. L. (2012). Overcoming the slow recovery of MOX gas sensors through a system modeling approach. Sensors, 12(10), 13664-13680.

15. Poo, C., Agarwal, G., Bonacchi, N., & Mainen, Z. F. (2022). Spatial maps in piriform cortex during olfactory navigation. Nature, 601(7894), 595-599.

16. Resulaj, A., & Rinberg, D. (2015). Novel behavioral paradigm reveals lower temporal limits on mouse olfactory decisions. Journal of Neuroscience, 35(33), 11667-11673.

17. Sunil, A., Pedroncini, O., Schaefer, A. T., & Ackels, T. (2024). How do mammals convert dynamic odor information into neural maps for landscape navigation?. Plos Biology, 22(11), e3002908.

18. Tariq, M. F., Lewis, S. M., Lowell, A., Moore, S., Miles, J. T., Perkel, D. J., & Gire, D. H. (2021). Using head-mounted ethanol sensors to monitor olfactory information and determine behavioral changes associated with ethanol-plume contact during mouse odor-guided navigation. eneuro, 8(1).

19. Wachowiak, M. (2011). All in a sniff: olfaction as a model for active sensing. Neuron, 71(6), 962-973.